# Nonlinear Optical Phenomena in Multimode Fibers

by

Shaival V. Buch

Submitted in Partial Fulfillment of the

Requirements for the Degree

Doctor of Philosophy

Supervised by Professor Govind P. Agrawal

The Institute of Optics

Arts, Science and Engineering

Edmund A. Hajim School of Engineering and Applied Sciences

University of Rochester

Rochester, New York

2018

# Table of Contents

# Biographical Sketch

The author was born in Gandhinagar in the state of Gujarat in India. After finishing high school in Vadodara, he enrolled in the Engineering Physics program at the Indian Institute of Technology Guwahati in Assam and obtained his Bachelor of Technology degree in 2012. In the fall of 2012, he joined The Institute of Optics, University of Rochester to pursue a Master of Science degree in Optics, which was awarded to him in 2013. In the fall of 2013, he enrolled in the PhD program at The Institute of Optics and joined Dr. Govind Agrawal's Nonlinear Photonics Group. He has worked on numerical modeling of nonlinear phenomena in multimode optical fibers and collaborated with Nokia Bell Labs to study light propagation through multimode lightwave systems. He was involved in a two-year experimental project on space optical communications using laser beam amplification as part of a collaboration between NASA and the University of Rochester. He also worked on free-space coherent optical communication systems as an intern at Mitsubishi Electric Research Labs.

**The following publications were a result of work conducted during doctoral study:**

**S. Buch** and G. P. Agrawal,"Soliton stability and trapping in multimode fibers," *Opt. Lett.*, vol. 40, pp. 225-228 (2015).

**S. Buch** and G. P. Agrawal, "Intermodal soliton interaction in nearly degenerate modes of a multimode fiber," *J. Opt. Soc. Am. B*, vol. 33, pp. 2217-2224 (2016).

P. Balla, **S. Buch** and G. P. Agrawal, "Effect of Raman scattering on soliton interactions in optical fibers," *J. Opt. Soc. Am. B*, vol. 34, 1247-1254 (2017).

**S. Buch**, S. Mumtaz, R.-J. Essiambre, A. M. Tulino and G. P. Agrawal, "Averaged nonlinear equations for multimode fibers valid in all regimes of random linear coupling," *manuscript under review.*

**Conference Presentations:**

**S. Buch**, Y. Xiao and G. P. Agrawal, "Soliton stability in multimode fiber," *Frontiers in Optics*, FW4D (2014)

**S. Buch** and G. P. Agrawal, "Soliton stability in multimode fiber," *Spatiotemporal Complexity in Nonlinear Optics* (2015).

**S. Buch** and G. P. Agrawal, "Soliton interaction in nearly degenerate modes of a multimode fiber," *Frontiers in Optics*, JTh2A.47 (2016).

**S. Buch** and G. P. Agrawal, "Intermodal suppression of spectral broadening in normal dispersion few-mode fibers," *Frontiers in Optics* JW4A.74 (2017).

**S. Buch**, S. Mumtaz, R.-J. Essiambre, A. M. Tulino and G. P. Agrawal, "Nonlinear propagation equations for arbitrary levels of random linear coupling between modes," *Optical Fiber Communications Conference and Exposition* (2018).

# Acknowledgments

I would like to acknowledge the numerous individuals who have played a role in making this thesis possible.

I am very thankful to my advisor Professor Govind Agrawal, for the support and guidance that he has provided for the duration of my PhD. He has been instrumental in every aspect of the research described in this thesis. He has contributed significantly to refining ideas and writing papers. His flexibility in allowing graduate students to pursue specific research opportunities and willingness to make himself available to his students for regular discussions has made this a very enriching experience. His humble and generous nature is an inspiration for any young scientist.

I am thankful to Dr. Rene-Jean Essiambre, for his guidance during the last year of my PhD and also for hosting me at Nokia Bell Labs. He has been a very patient and resourceful mentor. He provided me the opportunity to maximize my involvement in the scientific community at Bell Labs.

I would like to thank my committee members Professor Wayne Knox and Professor Qiang Lin, for providing useful suggestions during my thesis proposal.

I am thankful to Dr. William Donaldson for giving me the opportunity to perform experimental work in his lab at the Laboratory for Laser Energetics (LLE). He was very helpful and accommodating. I would also like to acknowledge Dr. Ildar Begishev for his help in keeping the laser up and running.

I would like to thank members from Professor Agrawal's Nonlinear Photonics Group, Dr. Yuzhe Xiao, Dr. Brent Plansinis, Aku Antikainen, Dr. Paco Arteaga-Sierra, Dr. Simranjit Singh, Prannay Balla and Amira Ahsan for several insightful and interesting conversations, during group meetings and in the graduate students office. I am especially thankful to Dr. Yuzhe Xiao for helping me get started on computational studies of nonlinear optics in multimode fibers and Dr. Brent Plansinis for helping me with my experimental setup at the LLE. I am also thankful to a former postdoctoral researcher from the group, Dr. Sami Mumtaz, as his research laid the ground for work on linear coupling described in this thesis. Outside the research group, I am grateful to Dr. Jordan Leidner and Dr. Haomin Yao from Professor John Marciante's group for many helpful discussions.

It is never easy to move to a new country, but the graduate student community at the University of Rochester and the academic and administrative staff at The Institute of Optics has made this experience worth all the effort. I am very grateful to professors at The Institute of Optics for some of the most enlightening and engrossing courses I have ever had the pleasure of taking.

Finally, I would like to thank my family and friends for their unconditional love and support. I have had the pleasure of meeting some wonderful people at Rochester, which has resulted in several lasting friendships and one cherished relationship to last a lifetime. Most importantly, I am grateful to my parents who have, directly and indirectly, made this entire journey possible.

# Abstract

Nonlinear optical effects are very well studied in optical fibers. However, most of these studies are restricted to fibers that support one spatial mode. Multimode fibers can provide several new nonlinear pathways due to intermodal effects, which makes light propagation through them difficult to understand. But several proposed applications have led to a resurgence in efforts to determine how nonlinearity manifests in multimode fibers. This thesis deals with many different studies undertaken to understand a subset of this large variety of nonlinear effects that occur inside a multimode fiber.

The first part of the thesis looks at two different manifestations of intermodal nonlinearity, spatiotemporal solitons and nonlinear spectral effects. The existence and interaction of solitons in multimode fibers is considered. Solitons, or a solitary wave packet that maintains its shape during propagation, is a commonly observed nonlinear artifact that has several applications in fiber optics. Intermodal interaction is added to the picture and the stability and formation of solitary wave packets in a multimode fiber are studied using numerical simulations. Simulations and theory are also used to understand how solitons propagating in different modes of a multimode fiber interact with each other owing to nonlinearity.

Nonlinear optics has been successfully exploited to generate sources with novel spectral profiles, including a broad supercontinuum, frequency-combs etc. A combination of several nonlinear effects in the medium is usually responsible for tailoring the source spectrum. Numerical results are presented that show a novel spectral suppression phenomenon in multimode fibers. Nonlinear spectral broadening is demonstrated through experimental results, using a special photonic crystal fiber.

The second part of this thesis explores the impact of random linear coupling between modes in a multimode or multicore fiber and how it affects nonlinear coupling. Random linear coupling can occur due to several imperfections in a real optical fiber and is important to consider when modeling systems that employ multimode fibers, like in the case of space division multiplexing communication systems. A comprehensive theoretical model is proposed that can be used to simulate the average nonlinear behavior with any amount of random linear coupling present in the system. Specific regimes of linear coupling are found to be more detrimental to optical communication systems. An experimental study to quantify linear coupling in a multicore fiber, and future work pertaining to it, are also described.

# Contributors and Funding Sources

Work reported in this thesis was conducted under the supervision of thesis advisor Professor Govind Agrawal from The Institute of Optics and committee members Professor Wayne Knox from The Institute of Optics and Professor Qiang Lin from the Department of Electrical and Computer Engineering.

Research reported in chapters 7-9 was co-supervised by Professor Govind Agrawal and Dr. René-Jean Essiambre from Nokia Bell Labs, Holmdel, NJ. Portions of this dissertation have been published elsewhere.

Chapter 5 is a result of work done in collaboration with Prannay Balla, formerly of Professor Govind Agrawal's Nonlinear Photonics Group. The experimental work described in chapter 6 was performed in Dr. William Donaldson's lab at the Laboratory for Laser Energetics, Rochester. Initial setup for this was done in collaboration with Dr. Brent Plansinis, formerly of Professor Govind Agrawal's Nonlinear Photonics Group. Chapters 7 and 8 are the result of continuation of work started by Dr. Sami Mumtaz, formerly of Professor Govind Agrawal's Nonlinear Photonics Group and visiting researcher at Nokia Bell Labs. The experimental work described in chapter 9 was performed in collaboration with Dr. Nicolas Fontaine and Dr. Haoshuo Chen at Nokia Bell Labs, Holmdel, NJ.

The material is based on work supported by the National Science Foundation - Grant Opportunities for Academic Liaison with Industry (GOALI) under award ECCS-1505636 and NASA Small Spacecraft Technology Program under award NNX13AQ83A.

# List of Tables

# List of Figures

# Chapter 1

# Introduction

## 1.1 Historical perspective

It is well known that any dielectric medium responds nonlinearly to an intense electromagnetic field. In particular, nonlinear optical effects have been studied extensively since 1962. In silica fibers, nonlinear effects can become very significant if a short, intense light pulse is propagated through it. While such nonlinear effects are usually considered detrimental to the performance of a fiber-based communication system, their understanding has also led to several applications where the nonlinear phenomena have been exploited for desired purposes.

Light coupled into an optical fiber propagates in the form of spatial modes supported by that fiber. Under certain conditions, which depend on the fiber design and the input wavelength, a fiber can be designed to support only a single spatial mode. Such single-mode optical fibers have been used extensively for observing nonlinear phenomena [1] as well as for designing optical communication systems [2]. Despite early studies on the nonlinearity of fibers that support more than one spatial mode i.e. multimode fibers (MMFs), they were historically regarded as low-quality waveguides because of a relatively large modal dispersion associated with them. However, MMFs have attracted attention recently because of their proposed use in telecommunications [3–7], imaging [8–11], fiber lasers [12, 13] etc. Such fibers provide an extra dimension over which communication channels can be multiplexed to meet the demand for ever-increasing capacity [14] and also have higher damage threshold, owing to the increased mode-field diameter, suitable for high-energy ultra short pulse applications.

Over the last ten years or so, a lot of experimental and theoretical work has been carried out toward the understanding of nonlinear effects in MMFs. Even though MMFs are used in data centers and local-area networks, telecommunication systems still use single-mode fibers to send data over long distances, both on land and under water. But the ever-increasing demand for network capacity has led to new avenues being explored at the research level. Having realized multiplexing in the temporal, spectral and polarization degrees of freedom for telecommunication systems using single-mode fibers, the attention has now shifted towards multiplexing data using spatial modes of a MMF or a multicore fiber, a technique referred to as space-division multiplexing (SDM), for the next generation of telecommunication systems [15–18]. Recently, MMFs have also been employed to scale mode-locked lasers to large mode-areas [19]. Multimode interference (MMI) effect has been exploited to design devices like mode-field adapters and low-loss couplers [20, 21]. For supercontinuum generation using ultra-short pulse regimes, MMFs offer an obvious solution to the fiber damage caused by such pulses in single-mode fibers [22] because of their larger core diameter. These and other proposed applications have led to a resurgence of interest and motivation to study and understand light propagation in MMFs that was previously lacking. A proper theoretical framework is needed to understand light propagation in such systems and to exploit the nonlinear effects for novel device designs and applications.

The complexity of analyzing MMFs increases with increasing number of modes. The Kerr nonlinearity of a fiber couples different spatial modes. Even for fibers supporting only 50-60 modes, millions of nonlinear coupling terms are present, leading to complex but very rich nonlinear dynamics [23]. Although nonlinear phenomena in MMFs have been studied since the early days of nonlinear optics [24–28], the efforts have been increased recently for a comprehensive analysis of light propagation in MMFs [23, 29–42, 42–47]. Such analysis is usually done under some simplifying assumptions that make a numerical or theoretical analysis feasible. But there is still a lot that we do not know or understand about nonlinear dynamics within a MMF.

The underlying motivation for the work described in this thesis is to better understand some of the fundamental physical effects that manifest inside a MMF. We use numerical modeling and some experimental results to study novel effects that occur due to intermodal nonlinear interaction. Additionally, the last three chapters of the thesis describe a study undertaken to understand and simulate the impact of random linear coupling in MMF, a topic that is very important for applications that employ MMFs.

## 1.2 Problems studied

An interesting manifestation of nonlinearity in a material is the formation of solitons. In the simplest terms, when the nonlinearity and dispersion in a material balance each other out, we observe the formation of a stable pulse (in space or time) that is invariant to weak perturbations. These pulses are known as solitons and they have been studied extensively in single-mode optical fibers, both theoretically and experimentally [1, 48–50]. However, solitons in MMFs are not well understood. Multiple spatial modes provide novel nonlinear pathways that can either help in the formation of solitons or perturb them. We explore the formation and interaction of solitons in the case of few-mode fibers, theoretically and numerically. More specifically, we consider how stable solitons are in a multimode environment and how their interaction is affected due to the presence of intermodal nonlinearities.

Nonlinearities have been exploited to generate new spectral components by using pulsed laser sources, which has been the basis for several important applications like optical parametric amplification, second-harmonic generation, supercontinuum generation etc. In fibers, third-order Kerr and Raman nonlinearities have been successfully used to generate spectral components of choice. These spectral components are generated because of the interplay of fiber dispersion and nonlinearity. Operating in the normal or anomalous dispersion region of a fiber can produce drastically different outcomes. The presence of additional nonlinear pathways in a MMF can provide more control, if understood properly, and extend our reach to exotic spectral regions not accessible in single-mode fibers. Here, we numerically consider the case of normal dispersion few-mode fibers and look at preliminary experimental results of spectral broadening in highly nonlinear photonic crystal fibers.

One of the major driving forces behind the renewed interest in MMFs is the proposed concept of space-division multiplexing (SDM) for the next generation of optical communication systems. In practice, aside from nonlinear coupling between modes, which is the major focus of this thesis, small perturbations in a real fiber can cause different modes to couple linearly with each other. This can occur due to several reasons like microbending, density fluctuations, shape irregularities etc. This effect is usually stochastic in nature and difficult to quantify. Additionally, it can also impact the nonlinear coupling between modes. We build a comprehensive theoretical model and consider some preliminary experimental data to characterize the average impact of random linear coupling on nonlinear interaction between modes, for any level of linear coupling. Averaging has been applied in the past to account for birefringence fluctuations in single-mode fibers or in specific coupling regimes in MMFs. Such averaged equations, known as Manakov equations, can be very useful for reducing the simulation time required to model real systems that employ MMFs, like SDM optical communication systems.

## 1.3 Thesis outline

Chapters 2–6 of this thesis include several numerical studies and some preliminary experimental results to understand the underlying physics of nonlinear effects that occur when short pulses are propagated inside a MMF. The impact of intermodal nonlinearities on spatiotemporal effects like multimode solitons and nonlinear spectral effects are studied.

In chapter 2, we develop the theory of nonlinear pulse propagation in MMFs. We review how Maxwell's equations can be reduced to a set of coupled nonlinear Schrödinger equations (NLSE) that can be used to model the propagation of optical field envelopes in a MMF. These equations include the effect of dispersion, third-order Kerr nonlinearity and higher-order nonlinear effects like stimulated Raman scattering and self-steepening. We then briefly review the two algorithms that we use to numerically solve the coupled NLSE.

In chapter 3, we use the coupled NLSE to study the formation and stability of solitons in MMFs. Using a six-mode fiber as an example, we simulate the evolution of solitons and try to understand how intermodal nonlinear interactions affect their stability and propagation behavior. We also consider the impact of differential group-delay (DGD) between modes and dispersion on soliton propagation in mutlimode fibers.

In chapter 4, we further investigate the interaction between two solitons in a MMF, specifically owing to the third-order Kerr nonlinearity. By numerically simulating two temporally separated solitons propagating in nearly-degenerate modes of a MMF, we try to understand how different pulse and fiber parameters change the interaction behavior and how it compares to the well-known case of soliton interaction in single-mode fibers.

In chapter 5, we extend the study of soliton interaction by considering the impact of Raman scattering in addition to Kerr nonlinearity. For this purpose, we simulate a shorter pulse, where the Raman effect becomes significant over the propagation distances that we consider. We observe this behavior for single-mode fibers, since the impact of Raman scattering on soliton interaction in single-mode fibers is also an interesting phenomenon that has not been studied extensively. Finally, we extend the case to MMFs.

In chapter 6, we consider two different nonlinear spectral effects in MMFs. First, we study numerically an interesting phenomenon of spectral suppression in normal dispersion few-mode fibers. Then, we look at some preliminary experimental results of nonlinear spectral broadening in a few-mode photonic crystal fiber.

Chapters 7–9 examine the case of random linear coupling that occurs in real fibers. More specifically, the impact of random linear coupling on nonlinear propagation is considered. This study is relevant for the optical communications industry in the context of space-division multiplexing.

In chapter 7, we develop a general theoretical framework to model nonlinear pulse propagation in MMFs while including random linear coupling between modes. We develop equations that can simulate the averaged behavior over several instantiations of random coupling. These equations are an extension of the averaged Manakov equations, derived for the case of birefringence fluctuations in single-mode fibers, to the multimode case.

In chapter 8, we use the equations developed in the previous chapter to study the impact of random linear coupling on multimode propagation. A parameter in our theory can be used to quantify the extent of linear coupling. The results discussed here can be applied to any regime of linear coupling. We also consider full numerical simulations of an optical communication system in different regimes of linear coupling.

Finally, in chapter 9, we briefly consider an experiment that was performed to characterize random linear coupling in coupled-core fibers and discuss the future work required for this project.

# Chapter 2

# Theory of multimode propagation

As we saw in the previous chapter, multimode fibers (MMFs) have been used ever since the invention of optical fibers in the 1950s. However, except for some early work during the 1970s [51], nonlinear effects in MMFs were not well studied up until recently. While a theory for nonlinear propagation of short pulses in single-mode fibers (SMFs) based on the nonlinear Schrödinger equation has been well established [1], simulating nonlinear propagation in multimode fibers was only studied under specific cases of a birefringent fiber or a fiber supporting two distinct modes up until a decade and a half ago [52–59]. With the increasing interest in studying MMFs, a robust theory of generalized multimode propagation was necessary. In Sect. 2.1, we look at the generalized multimode nonlinear Schrödinger equation (MM-NLSE) that has been derived for modeling nonlinear phenomena in multimode fibers. In Sect. 2.2, we simplify this equation by normalizing and removing certain terms corresponding to higher-order effects and re-write it in a form that will be used often in the chapters that follow. Finally in Sect. 2.3, we briefly describe two numerical techniques that have been used to solve the MM-NLSE for the results shown in chapters 3–6.

## 2.1 Generalized multimode nonlinear Schrödinger equation

We follow the procedure described by Poletti and Horak [29]. We start with the Maxwell's two curl equations

$$\nabla \times \mathbf{E}(\mathbf{r},t) = -\mu_0 \frac{\partial}{\partial t}\mathbf{H}(\mathbf{r},t), \tag{2.1a}$$

$$\nabla \times \mathbf{H}(\mathbf{r},t) = \epsilon_0 \frac{\partial}{\partial t}\mathbf{E}(\mathbf{r},t) + \frac{\partial}{\partial t}\mathbf{P}(\mathbf{r},t). \tag{2.1b}$$

$\mathbf{E}$ and $\mathbf{H}$ are the electric and magnetic field vectors, $\epsilon_0$ is the vacuum permittivity, $\mu_0$ is the vacuum permeability and $\mathbf{P}$ is the induced polarization which is given by

$$\mathbf{P}(\mathbf{r},t) = \mathbf{P}_{\mathrm{L}}(\mathbf{r},t) + \mathbf{P}_{\mathrm{NL}}(\mathbf{r},t), \tag{2.2}$$

where the linear ($\mathbf{P}_{\mathrm{L}}$) and nonlinear ($\mathbf{P}_{\mathrm{NL}}$) parts of the induced polarization are related to the electric field by the relations

$$\mathbf{P}_{\mathrm{L}}(\mathbf{r},t) = \epsilon_0 \chi^{(1)}\mathbf{E}(\mathbf{r},t), \tag{2.3a}$$

$$\mathbf{P}_{\mathrm{NL}}(\mathbf{r},t) = \epsilon_0 \chi^{(3)}\mathbf{E}(\mathbf{r},t) \int_{-\infty}^{\infty} R(t-t')|\mathbf{E}(\mathbf{r},t')|^2 dt'. \tag{2.3b}$$

$\chi^{(1)}$ and $\chi^{(3)}$ are the first and third-order susceptibility. $\chi^{(3)}$ governs the third-order nonlinear effects, which are the primary nonlinear effects that occur in a silica fiber as $\chi^{(2)}$ is absent due to symmetry properties. $R(t)$ is the third-order nonlinear response function that accounts for both the Kerr nonlinearities (instantaneous response) and the Raman nonlinearity resulting from delayed molecular response.

Taking the curl of Eq. (2.1a) and using Eq. (2.1b), we get the relation

$$\nabla^2\mathbf{E} - \frac{1}{c^2}\frac{\partial^2\mathbf{E}}{\partial t^2} = \mu_0\frac{\partial^2\mathbf{P}_\mathrm{L}}{\partial t^2} + \mu_0\frac{\partial^2\mathbf{P}_\mathrm{NL}}{\partial t^2}. \tag{2.4}$$

If we take a Fourier transform of this equation, we get

$$\nabla^2\tilde{\mathbf{E}} + \frac{n(x,y)^2\omega^2}{c^2}\tilde{\mathbf{E}} = -\frac{\omega^2}{\epsilon_0 c^2}\tilde{\mathbf{P}}_\mathrm{NL}, \tag{2.5}$$

where $\sim$ denotes a spectral domain quantity and $n(x,y) = [1+\chi^{(1)}]^{1/2}$ is the linear refractive index of the material. Its x and y dependence results from different refractive indices in the core and cladding of a MMF and leads to a set of modes with different transverse shapes $[F_p(x,y)]$ and propagation constant $\beta_p$ such that $p = 1, 2, \ldots N$, where $N$ is the number of modes. This is the form of the wave equation that we will solve. To solve the nonlinear problem, we can expand the electric field into a sum of all modal functions $F_p(x,y,\omega)$ with envelopes $\tilde{A}_p(z,\omega)$. The electric field can then be written as

$$\mathbf{E}(\mathbf{r},\omega) = C\sum_p F_p(x,y,\omega)e^{\imath\beta_p(\omega)z}\tilde{A}_p(z,\omega)\hat{\mathbf{e}} \tag{2.6}$$

where $\beta_p$ is the propagation constant of the $p^{th}$ mode and the normalization constant is given by $C = [(1/2)\epsilon_0 c n_\mathrm{eff}]^{-1/2}$, where $n_\mathrm{eff}$ corresponds to the effective index of the fundamental fiber mode. The modal functions satisfy the equation

$$\nabla_T^2 F_p + \frac{n(x,y)^2\omega^2}{c^2}F_p = \beta_p^2 F_p \tag{2.7}$$

and are normalized as follows

$$\iint F_p^* F_m dxdy = \left(\frac{n_\mathrm{m}}{n_\mathrm{eff}}\right)\delta_{pm}. \tag{2.8}$$

$\nabla_T^2$ is the transverse part of the $\nabla^2$ operator and $n_\mathrm{m}$ is the effective index of the m$^{th}$ mode. We have assumed propagation in the $z$ direction. The vectorial nature of the field is included through the unit vector $\hat{\mathbf{e}}$. We treat $F_p(x,y,\omega)$ as a scalar.

We assume that the electric field envelope $\tilde{A}_p$ varies slowly with $z$ and so we ignore its second derivative. Using this slowly varying approximation (SVA) and substituting Eq. (2.6) in Eq. (2.5), we get

$$C\sum_p 2\imath\beta_p F_p(x,y,\omega)\frac{\partial\tilde{A}_p}{\partial z}e^{\imath\beta_p z}\hat{\mathbf{e}} = -\frac{\omega^2}{\epsilon_0 c^2}\tilde{\mathbf{P}}_\mathrm{NL}. \tag{2.9}$$

If we left-multiply this equation with $F_p^*\hat{\mathbf{e}}$ and integrate over the transverse coordinates, we end up with the following equation for the spectral mode amplitudes

$$\frac{\partial\tilde{A}_p}{\partial z} = \frac{\imath\omega C}{4}\frac{n_\mathrm{eff}}{n_\mathrm{m}}e^{-\imath\beta_p z}\iint F_p^*\hat{\mathbf{e}}\cdot\tilde{\mathbf{P}}_\mathrm{NL}dxdy. \tag{2.10}$$

From Eq. (2.3b), we know that $\tilde{\mathbf{P}}_{\mathrm{NL}}(\omega)$ would be a convolution of three mode fields $(F_p\tilde{A}_p)$ and the time response function $R(\omega)$. We can then follow the treatment by Mamyshev and Chernikov [60] to write the pulse propagation equation in the time domain for silica fibers. We neglect the frequency dependence of the transverse mode functions $[F_p(x,y,\omega) \approx F_p(x,y,\omega_0)]$ and the normalization constants while performing the convolution integral. But the resulting spatial overlap integral is then assumed to be frequency dependent to the first order linear term around a central frequency $\omega_0$. This approximation has been shown to give improved results for nonlinear simulations [61]. We expand the propagation constant $\beta_p(\omega)$ in a Taylor series as follows

$$\beta_p(\omega) = \beta_{0p} + \beta_{1p}(\omega-\omega_0) + \frac{1}{2}\beta_{2p}(\omega-\omega_0)^2 + \cdots ; \qquad \beta_{kp} = (\frac{d^k\beta_p}{d\omega^k})|_{(\omega=\omega_0)}. \tag{2.11}$$

With these approximations and after some algebra, we get the following generalized MM-NLSE for mode $p$

$$\begin{aligned}
&\frac{\partial A_p(z,t)}{\partial z} - \imath(\beta_0^{(p)} - \beta_0)A_p(z,t) + (\beta_1^{(p)} - \beta_1)\frac{\partial A_p(z,t)}{\partial t} - \imath\sum_{n\geqslant 2}\frac{\beta_n^{(p)}}{n}\left(\imath\frac{\partial}{\partial t}\right)^n A_p(z,t) \\
&= \imath\frac{\gamma}{3}\sum_{lmn}\left(1+\tau_{lmnp}\frac{\partial}{\partial t}\right) f_{lmnp}\Bigg\{2A_l(z,t)\int dt' R(t')A_m(z,t-t')A_n^*(z,t-t') \\
&\qquad + A_l^*(z,t)\int dt' R(t')A_m(z,t-t')A_n(z,t-t')e^{2\imath\omega_0 t'}\Bigg\},
\end{aligned} \tag{2.12}$$

where $\gamma = n_2\omega_0/cA_{\text{eff}}$ is called the nonlinear parameter, with $n_2$ being the nonlinear refractive index and $A_{\text{eff}}$ the effective area of the fundamental mode. $\beta_0$ and $\beta_1$ correspond to the propagation constant and the inverse group velocity of the fundamental mode, which has been used here as the reference mode. We have made the assumption here that all the spatial mode functions $(F_p)$ are real. The spatial overlap factor $f_{lmnp}$, which governs nonlinear coupling between modes, is given by

$$f_{lmnp} = A_{\text{eff}}\iint F_l^* F_m F_n F_p^* dxdy \tag{2.13}$$

and the shock time constant [29] is given by

$$\tau_{lmnp} = \frac{1}{\omega_0} + \left\{\frac{\partial}{\partial\omega} ln[\frac{\gamma}{3}f_{lmnp}]\right\}. \tag{2.14}$$

The nonlinear time response function can be written as

$$R(t) = (1-f_R)\delta(t) + \frac{3}{2}f_R h(t), \tag{2.15}$$

where $f_R$ is the fractional contribution of the Raman response to the total nonlinearity and $h(t)$ is the delayed Raman response function. For silica fibers, we can use the Raman response given by [62].

The final integral in Eq. (2.12) has a rapidly oscillating term $e^{2\imath\omega_0 t'}$. If the response function $R(t')$ is a delta function, which we will see is the case when only Kerr nonlinearity is considered, this exponential term does not contribute to the integral. But if the response function has a delayed temporal response, like in the case of Raman nonlinearity, we assume that the presence of this rapidly oscillating term causes the contribution of the last integral in Eq. (2.12) to go to 0. Hence, we will remove that term from our integral and rewrite it as follows

$$\begin{aligned}\frac{\partial A_p(z,t)}{\partial z} &- \imath(\beta_0^{(p)}-\beta_0)A_p(z,t)+(\beta_1^{(p)}-\beta_1)\frac{\partial A_p(z,t)}{\partial t} - \imath\sum_{n\geqslant 2}\frac{\beta_n^{(p)}}{n}\left(\imath\frac{\partial}{\partial t}\right)^n A_p(z,t)\\ &= \imath\frac{\gamma}{3}\sum_{lmn}\left(1+\tau_{lmnp}\frac{\partial}{\partial t}\right) f_{lmnp}\Bigg\{2A_l(z,t)\int dt' R(t')A_m(z,t-t')A_n^*(z,t-t')\\ &\qquad + A_l^*(z,t)\int dt' R(t')A_m(z,t-t')A_n(z,t-t')\Bigg\}. \qquad (2.16)\end{aligned}$$

Under this approximation, the nonlinear time response function becomes

$$R(t) = (1-f_R)\delta(t) + f_R h(t). \qquad (2.17)$$

When we study cases without including the Raman response, we will set $f_R$ to 0.

## 2.2 Normalized MM-NLSE

Equation (2.15) is the generalized MM-NLSE which includes the effects of all orders of dispersion, third-order nonlinear effects, Raman scattering and the shock effect by including the frequency dependence of the nonlinear parameter up to first order. For the work shown in this thesis, we will not be including dispersion effects of order three and higher and the shock effects. These are reasonable approximations if we are simulating short distance propagation for pulses which are not being launched close to the zero-dispersion wavelength of the fiber and that have pulse widths of the order of ∼ps or larger, respectively. In that case, Eq. (2.15) reduces to

$$\begin{aligned}\frac{\partial A_p(z,t)}{\partial z} &- \imath(\beta_0^{(p)}-\beta_0)A_k(z,t)+(\beta_1^{(p)}-\beta_1)\frac{\partial A_p(z,t)}{\partial t} + \imath\frac{\beta_2^{(p)}}{2}\frac{\partial^2 A_p(z,t)}{\partial t^2}\\ &= \imath\frac{\gamma}{3}\sum_{lmn} f_{lmnp}\Bigg\{2A_l(z,t)\int dt' R(t')A_m(z,t-t')A_n^*(z,t-t')\\ &\qquad + A_l^*(z,t)\int dt' R(t')A_m(z,t-t')A_n(z,t-t')\Bigg\}. \qquad (2.18)\end{aligned}$$

A final major simplification that can be made is ignoring the Raman effect ($f_R = 0$), which is a weak effect for pulse widths of the order of picosecond or higher [1]. The MM-NLSE then reduces to

$$\begin{aligned}\frac{\partial A_p(z,t)}{\partial z} &- \imath(\beta_0^{(p)}-\beta_0)A_p(z,t)+(\beta_1^{(p)}-\beta_1)\frac{\partial A_p(z,t)}{\partial t} + \imath\frac{\beta_2^{(p)}}{2}\frac{\partial^2 A_p(z,t)}{\partial t^2}\\ &= \imath\frac{\gamma}{3}\sum_{lmn} f_{lmnp}\left[2A_l(z,t)A_m(z,t)A_n^*(z,t) + A_l^*(z,t)A_m(z,t)A_n(z,t)\right]. \qquad (2.19)\end{aligned}$$

If we consider a fiber that supports $M$ spatial modes, we also have to account for the fact that each spatial mode has two orthogonally polarized components. So the fiber under consideration supports a total of $N = 2M$ modes. To get a better physical sense of these orthogonally polarized modes, we can represent the field envelopes in a Jones-vector notation ($\mathbf{A}_p(z,t) = [A_{px}(z,t), A_{py}(z,t)]^T$). Eq. (2.18) can then be rewritten as

$$\frac{\partial \mathbf{A}_p}{\partial z} - \imath(\boldsymbol{\beta}_0^{(p)} - \beta_0)\mathbf{A}_p + (\boldsymbol{\beta}_1^{(p)} - \beta_1)\frac{\partial \mathbf{A}_p}{\partial t} + \imath\frac{\boldsymbol{\beta}_2^{(p)}}{2}\frac{\partial^2 \mathbf{A}_p}{\partial t^2} = \imath\frac{\gamma}{3}\sum_{lmn} f_{lmnp}\left[2\mathbf{A}_l^T\mathbf{A}_m\mathbf{A}_n^* + \mathbf{A}_l^H\mathbf{A}_m\mathbf{A}_n\right]. \quad (2.20)$$

$T$ and $H$ represent the transpose and Hermitian conjugate of a matrix. $\boldsymbol{\beta}_0^{(p)}$, $\boldsymbol{\beta}_1^{(p)}$ and $\boldsymbol{\beta}_2^{(p)}$ are 2×2 diagonal matrices with the propagation constant, inverse group velocity and group-velocity dispersion (GVD) parameter values respectively of the x and y components of the $p^{th}$ mode as its diagonal values. We have made the assumption here that both the orthogonally polarized modes have the same spatial profile. Note that we no longer explicitly denote the dependence of the field envelopes ($\mathbf{A}_p$) on $z$ and $t$ for the sake of simplicity.

In chapters 3 and 4, we will be using this model to study the existence and interaction of soliton pulses in a MMF. While we will look at what solitons are in greater detail in the next chapter, it is helpful to normalize this equation in terms of so-called "soliton units" at this point. This exercise will also help reduce the number of input parameters required for modeling nonlinear pulse propagation through a MMF. We can also do a mathematical transformation by including the propagator ($e^{\imath(\beta_0^{(p)}-\beta_0)z}$) in the definition of the field envelope ($A_p$), which will move the phase-mismatch effect from the linear term to an exponential in the nonlinear term. If we assume that the input pulse in the reference mode of the fiber (chosen as the fundamental mode here) has peak power $P_0$ and width $T_0$, then the set of coupled NLSE in Eq. (2.19) can be normalized and written as

$$\frac{\partial \mathbf{u}_p}{\partial \xi} + d_{1p}\frac{\partial \mathbf{u}_p}{\partial \tau} + \imath\frac{d_{2p}}{2}\frac{\partial^2 \mathbf{u}_p}{\partial \tau^2} = \imath\frac{N^2}{3}\sum_{lmn} f_{lmnp}\left[2\mathbf{u}_l^T\mathbf{u}_m\mathbf{u}_n^* + \mathbf{u}_l^H\mathbf{u}_m\mathbf{u}_n\right]e^{\imath\Delta\beta_{lmnp}\mathrm{L_D}\xi}. \quad (2.21)$$

In this equation, $\mathbf{u}_p = \mathbf{A}_p/\sqrt{P_0}$, $\tau = t/T_0$ and $\xi = z/\mathrm{L_D}$, where $\mathrm{L_D}$ corresponds to the dispersion length of the fundamental mode given by $\mathrm{L_D} = T_0^2/|\beta_2|$ ($\beta_2$ is the GVD parameter of the fundamental mode). The parameter $N$ corresponds to the soliton order, as we will see later. It is defined as $N^2 = \gamma P_0 T_0^2/|\beta_2|$. The phase-mismatch parameter appearing in the nonlinear term is defined as $\Delta\beta_{lmnp} = \beta_0^{(m)} + \beta_0^{(n)} - \beta_0^{(l)} - \beta_0^{(p)}$. The two normalized differential group delay (DGD) and group velocity dispersion (GVD) parameters ($d_{1p}$ and $d_{2p}$ respectively) are defined as

$$d_{1p} = (\beta_1^{(p)} - \beta_1)\frac{\mathrm{L_D}}{T_0}; \qquad d_{2p} = \frac{\beta_2^{(p)}}{|\beta_2|}. \quad (2.22)$$

We have derived several simplified versions of the generalized MM-NLSE [Eq. (2.15)] in this section, by making certain physical approximations and normalizing some parameters. In the following chapters, we will be using a version of the MM-NLSE that we have derived here to study different nonlinear effects in MMFs. For each case that we consider, we will simply refer to the relevant equation from this chapter that we used to simulate it.

Another important point to keep in mind for the remainder of this thesis is that we will work with the linearly-polarized (LP) modes terminology (instead of the real HE and EH modes) for step-index fibers, which is valid in the weakly-guiding approximation for fibers with a relatively small refractive index difference between the core and cladding.

## 2.3 Numerically solving the coupled NLSE

The NLSE, apart from certain specific cases, cannot be solved analytically. Here we will briefly describe the two numerical approaches that have been used to solve this equation under different conditions for the work presented in this thesis.

### 2.3.1 Split-step Fourier method

A common numerical approach that has been used to solve the NLSE over the years for the single-mode case is the split-step Fourier method (SSFM) [63, 64]. It is a pseudo-spectral approach that utilizes the finite-Fourier transform (FFT) algorithm. It has also been applied to the case of MMF, where we need to solve coupled partial differential equations. To see how the SSFM works, we can re-write Eq. (2.17) in the following form

$$\frac{\partial A_p(z,t)}{\partial z} - \hat{D}^{(p)}(z,t)A_p(z,t) = \hat{N}^{(p)}(z,t)A_p(z,t), \tag{2.23}$$

where all the dispersion terms ($\hat{D}^{(p)}$) and nonlinear terms ($\hat{N}^{(p)}$) have been separately grouped together. This equation can now be written as

$$\frac{\partial A_p}{\partial z} = (\hat{D}^{(p)} + \hat{N}^{(p)})A_p. \tag{2.24}$$

The solution to this equation can be given by

$$A_p(z+\Delta z,t) = exp[\Delta z(\hat{D}^{(p)} + \hat{N}^{(p)})]A_p(z,t), \tag{2.25}$$

where $\Delta z$ is the chosen step-size along the length of the fiber. In the SSFM, both the dispersion and nonlinearity exponentials that show up in this equation are solved separately. This is done by making an approximation that for small step sizes, the dispersion and nonlinearity can be assumed to act independently. Mathematically, it can be written as

$$A_p(z+\Delta z,t) \approx exp[\Delta z\hat{D}^{(p)}]exp[\Delta z\hat{N}^{(p)}]A_p(z,t), \tag{2.26}$$

Since the dispersion term only consists of linear terms with time-differential operators ($\partial/\partial t$), it is easier to solve it in the Fourier domain, where $\partial/\partial t$ can be replaced by $-\imath\omega$. $\hat{D}^{(p)}(-\imath\omega)$ then just becomes a number in the Fourier space.

By using this algorithm, the field amplitude ($A_p$) after every step ($\Delta z$) can be numerically calculated by separating the contributions from the dispersion and nonlinear terms. Further improvements in accuracy can be obtained by adopting a scheme where we first calculate the effect of dispersion for half-step propagation [$exp(\Delta z\hat{D^{(p)}}/2)$], then include the total effect of nonlinearity for the entire step [$exp(\Delta z\hat{N}^{(p)})$] and then add the effect of dispersion for the other half-step propagation [$exp(\Delta z\hat{D^{(p)}}/2)$]. Under this approximation, the nonlinearity is assumed to be discretely lumped at the middle of each propagation step. Mathematically, this can be written as

$$A_p(z+\Delta z,t) \approx e^{\frac{1}{2}\Delta z\hat{D}^{(p)}}e^{\Delta z\hat{N}^{(p)}}e^{\frac{1}{2}\Delta z\hat{D}^{(p)}}A_p(z,t). \tag{2.27}$$

There are further improvements that can be made to this scheme, like integrating the effect of nonlinearity over the entire step and including it at the middle of the propagation step, but we will not discuss them here.

This algorithm is accurate to third order in the step-size $\Delta z$. While we looked at the algorithm from the perspective of a particular ($p^{th}$) mode, we need to recall that MM-GNLSE is a set of coupled equations. So we employ this algorithm for each individual mode equation. Each mode is first propagated by one step-size ($\Delta z$). But the nonlinear term ($\hat{N}^{(p)}$) also depends on the mode-fields of all the other fiber modes. So we need to follow an iterative procedure where $A_p(z + \Delta z)$ is first estimated by calculating $\hat{N}^{(p)}(z + \Delta z)$ using the values of mode-fields at $z$. Then these updated values of $A_p(z+\Delta z)$ are used to calculate the new value of $\hat{N}^{(p)}(z + \Delta z)$.

While this algorithm has several built-in approximations, it nonetheless gives accurate numerical results for the cases considered in this thesis.

### 2.3.2 Fourth-order Runge-Kutta in the Interaction picture

Again, we start with Eq. (2.17). But this time, we take a Fourier transform of the entire equation. We can write this equation in the following form

$$\frac{\partial \tilde{A}_p}{\partial z} + \tilde{D}_p \tilde{A}_p = \tilde{N}_p, \tag{2.28}$$

where $\tilde{D}_p$ is an imaginary number that depends on the dispersion parameters for the $p^{th}$ mode and angular frequency ($\omega$). $\tilde{N}_p$ is the Fourier transform of the nonlinear term. We now make a transformation of variables given by

$$\tilde{A}_p' = \tilde{A}_p e^{\tilde{D}_p z}. \tag{2.29}$$

We make this transformation for each mode field. The NLSE in the spectral domain for the $p^{th}$ mode then becomes

$$\frac{\partial \tilde{A}_p'}{\partial z} = \tilde{N}_p' e^{\tilde{D}_p z}, \tag{2.30}$$

where $\tilde{N}_p'$ is the Fourier domain nonlinear term calculated using the transformed mode-fields ($A_p' = \mathcal{F}^{-1}[\tilde{A}_p']$). $\mathcal{F}$ represents the Fourier transform operation.

Equation (2.29) is now in the form of an ordinary differential equation (ODE). There are several numerical techniques to solve such ODEs. We will use the fourth-order Runge-Kutta method to solve this set of coupled ODEs and obtain the values of $\tilde{A}_p'(z, \omega)$ at each point along the propagation direction $z$. Finally, we can obtain the time-domain fields at each point along $z$ by doing the following transformation

$$A_p(z, t) = \mathcal{F}^{-1}[\tilde{A}_p'(z, \omega) e^{-\tilde{D}_p z}]. \tag{2.31}$$

This method is also known as the Interaction Picture method for solving the NLSE, a nomenclature which has its origins in quantum mechanics. This method was recently adopted to model supercontinuum generation in optical fibers [65]. Here, by making the variable transformations, we are including the time derivative within the transformed variable and solving in the frequency domain. This "picture" still lets us reveal all the physical properties of the system.

# Chapter 3

# Solitons in few-mode fibers

Solitons are one of the most well-known consequence of nonlinearity in a dielectric material, resulting from the interplay between nonlinear and dispersive effects. If the nonlinearity can exactly balance the dispersion effects inside a material, certain wave packets can be formed that can travel undistorted over long distances or evolve periodically. These solitary wave packets are known as solitons, a term that indicates its almost particle-like nature. They have been observed in many systems ranging from water canals to photonic waveguides [48–50].

In the context of fiber optics, solitons have been observed and studied extensively owing to fundamental interest and their applications in the field of optical communications. Solitons occur when the group-velocity dispersion (GVD) and self-phase modulation (SPM) inside a fiber exactly balance each other out. The presence of another pulse or higher-order nonlinear effects is then a perturbation to this soliton. In the case of single-mode fibers (SMFs), the inverse-scattering method to solve the NLSE has been successfully applied to predict the existence of solitons [66–68]. Without going into details of this method, what we need to know is that there exists a family of solutions that can propagate undistorted over long distances and this family of solutions has a secant-hyperbolic time dependence. Solitons and its applications in SMFs are well-documented [48–50, 67, 68]. Here, we will look at the existence of soliton-like wave packets in few-mode fibers (FMFs) and numerically study their stability in the presence of intermodal nonlinear coupling.

## 3.1 Temporal stability of solitons in few-mode fibers

The existence of optical solitons in multimode fibers hasn't been studied in detail. While there were few initial reports of solitons in multimode fibers [25, 26, 28, 69], which are solitary waves that span over more than one mode of a fiber, the recent surge in interest in multimode fibers has inspired a detailed analysis of the conditions for the existence of multimode solitons and their stability. We consider a case where fundamental solitons are launched individually in any mode of a multimode fiber. In this situation, we ask ourselves how stable the solitons are in the presence of intermodal nonlinearities which can be seeded by optical noise.

We consider a fiber which supports only the first two spatial modes in the linearly polarized (LP) modes approximation, namely $LP_{01}$ and $LP_{11}$. The $LP_{11}$ mode is two-fold degenerate and consists of two distinct degenerate modes $LP_{11a}$ and $LP_{11b}$. Accounting for the two orthogonally polarized components of each of these three modes, we end up with a total of six modes that this fiber can support. We model this case by using Eq. (2.20)

| Modes involved | Coupling terms | Value |
|---|---|---|
| $LP_{01}$ | $f_{1111}$ | 1 |
| $LP_{11a}$, $LP_{11b}$ | $f_{2222}$, $f_{3333}$ | 3/4 |
| $LP_{01}$-$LP_{11a}$, $LP_{01}$-$LP_{11b}$ | $f_{1212}$, $f_{2211}$, $f_{1122}$, $f_{2121}$, $f_{1313}$, $f_{1133}$, $f_{3311}$, $f_{3131}$ | 1/2 |
| $LP_{11a}$-$LP_{11b}$ | $f_{2332}$, $f_{3232}$, $f_{3322}$, $f_{2323}$, $f_{3223}$, $f_{2233}$ | 1/4 |

*Tab. 3.1:* Nonlinear coupling parameters ($f_{plmn}$) for the few-mode fiber under consideration.

and set $f_R = 0$ and $u_p(0, \tau) = u_0 sech(\tau)$, where $u_0$ is set to 0 for modes in which no pulse is launched. As was mentioned in chapter 2, the parameter $N$ in Eq. (2.20) corresponds to the soliton-order. In the case of SMFs, we expect a fundamental soliton ($N = 1$) to propagate undistorted and higher-order solitons ($N \geqslant 2$) to undergo periodic evolution, with the period given by $\xi = \pi/2$ [1]. To understand the effect of intermodal nonlinear coupling, we assume an ideal fiber and neglect any linear coupling and losses. For the initial analysis, we set the differential group-delay (DGD) between different modes to be 0 ($d_{1p} = 0$). This is done to ensure that the modes overlap and thereby stay coupled along the entire length of the fiber. In the next section, we will look at the impact of different values of DGD between the modes.

As we saw earlier, the overlap integral $f_{lmnp}$ governs the nonlinear coupling between modes. Since $l, m, n, p$ can go from 1-3 in this case, one needs to specify a total of 81 parameters to fully account for nonlinear coupling. However, a large number of them vanish because of orthogonality and phase-matching conditions, and many coincide in values because of the degeneracy of $LP_{11a}$ and $LP_{11b}$ modes. We are left with 17 non-zero terms. For numerical simulations, we use the values of fiber parameters given in [70]. Using the effective areas given there, we find $\gamma = 1.77$ W$^{-1}$/km and the values of the 17 non-zero nonlinear overlap parameters ($f_{lmpn}$) are given in Table 3.1. For our choice of $T_0 = 1$ ps ($T_{\mathrm{FWHM}} = 1.77ps$), $L_D = 41.15$ m and $d_{22} = 1.06$. The DGD parameter ($d_{1p}$) is set to 0 for the results shown in this section.

### 3.1.1 Single soliton propagation

We solve Eq. (2.20) using the split-step Fourier method described in Chapter 2. We first consider the case where a single fundamental soliton is launched in any given mode of the fiber. Our results show that the soliton remains unchanged and retains all of its energy even after propagating for hundreds of dispersion lengths, irrespective of the mode that it was launched into. To understand the stability of such solitons, we introduce perturbations in the form of white noise with a spectral density of $10^{-17}$ W/Hz to all the channels. This noise can seed intermodal and intramodal nonlinear effects. Remarkably, we observe that the solitons still propagate in a stable fashion. As an example, Fig. 3.1 shows a case where a fundamental soliton is propagated in the $LP_{01x}$ mode for a 100 dispersion lengths. We can see from the figure that a small amount of energy if transferred to the orthogonally polarized mode when it is seeded by white noise. But the magnitude of this energy transfer remains well below 0.1% of the input energy.

We also simulate a similar scenario with a higher-order soliton. An example of such a case is shown in Fig. 3.2, where a second-order soliton is launched in the $LP_{01x}$ mode of the fiber and the other modes are seeded with white noise. We notice that, similar to the case of single-mode fibers, the second-order soliton displays oscillatory behavior with a period

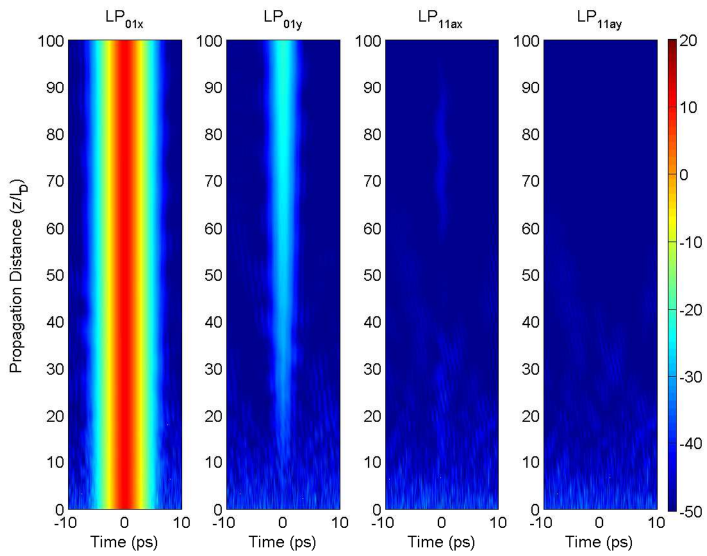


*Fig. 3.1:* Fundamental soliton launched in the $\mathrm{LP}_{01x}$ mode along with noise in all other modes (The $\mathrm{LP}_{11b}$ mode, which is not shown here, behaves similar to the $\mathrm{LP}_{11a}$). The color bar shows optical power on a dB scale

of $\xi = \pi/2$. But again, while there is some power transfer between the modes owing to noise-seeded intermodal nonlinearity, it is a negligible loss of energy and the fundamental mode retains almost all of the power launched into it. These results clearly indicate that an isolated solion of any order launched in any given mode of a multimode fiber propagates in a stable fashion.

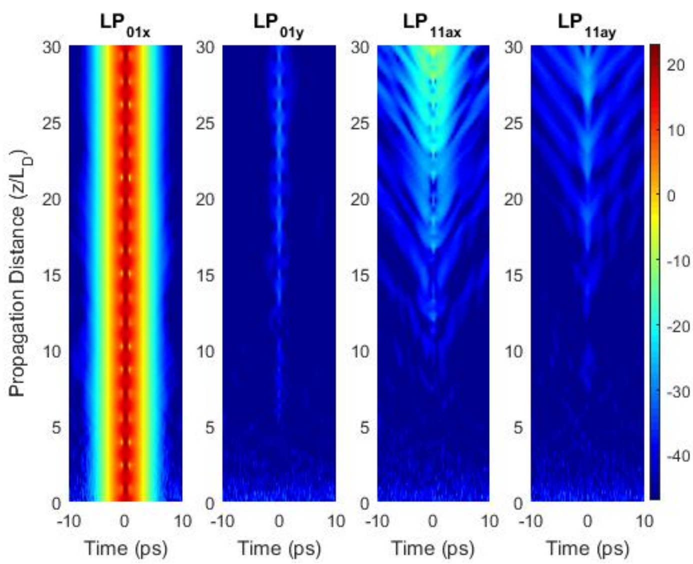


*Fig. 3.2:* Second-order soliton launched in the $\mathrm{LP}_{01x}$ mode along with noise in all other modes (The $\mathrm{LP}_{11b}$ mode, which is not shown here, behaves similar to the $\mathrm{LP}_{11a}$). The color bar shows optical power on a dB scale

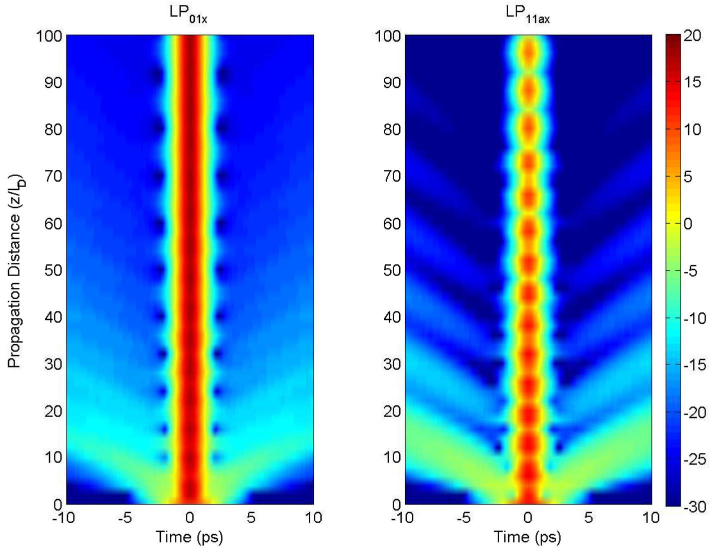


(a)

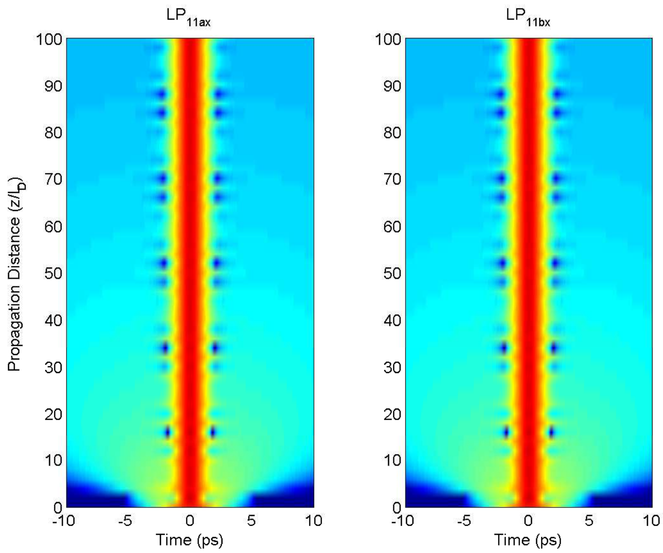


(b)

*Fig. 3.3:* Simultaneous propagation of fundamental solitons in two fiber modes: (a) $\mathrm{LP}_{01x}$ and $\mathrm{LP}_{11ax}$, (b) $\mathrm{LP}_{11ax}$ and $\mathrm{LP}_{11bx}$. The color bar shows optical power on a dB scale.

### 3.1.2 Multiple soliton propagation

We observe much more interesting behavior if more than one fundamental solitons are launched simultaneously into different fiber modes. We use the same numerical model and fiber parameters as used in the previous subsection. Fig.3.3 shows the evolution over 100 dispersion length for two such cases. In Fig. 3.3a, two co-polarized solitons are launched simultaneously in the non-degenerate $\mathrm{LP}_{01x}$ and $\mathrm{LP}_{11ax}$ modes of the fiber. Both solitons initially lose some energy in the form of dispersive waves and become narrower. To understand this behavior, we recall that strong intermodal interaction is possible because of the large spatial overlap between modes, despite traveling in different fiber modes. As a result, each soliton modulates the phase of the other soliton substantially through

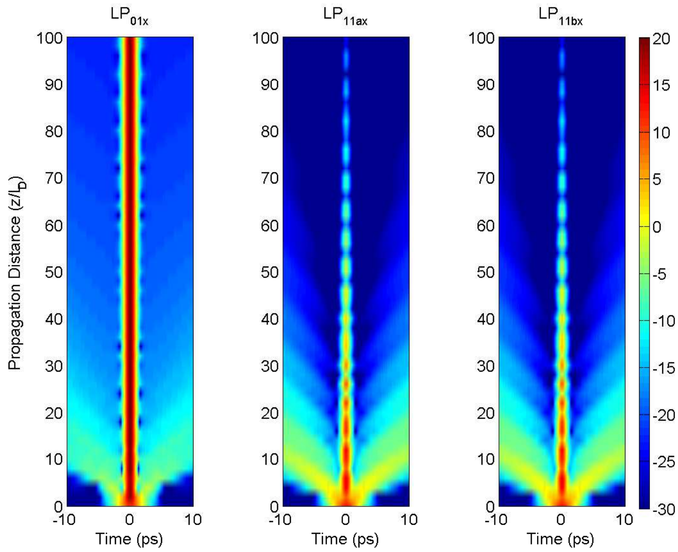


*Fig. 3.4:* Simultaneous propagation of $x$-polarized solitons in three fiber modes. The color bar shows optical power on a dB scale.

intermodal XPM. In effect, the total nonlinear phase shift seen by each soliton is larger than that of an isolated soliton. Since this simulation is similar to the case of a single soliton with N>1, each soliton undergoes an initial narrowing phase. This XPM-induced perturbation is responsible for the excess radiation being shed initially by each soliton as dispersive waves. However, most of the radiation is shed within the first few dispersion lengths and the energy lost by each soliton remains less than 1% of the input energy.

The most important feature of Fig. 3.3a is that the solitons undergo an oscillatory phase during which the pulse in $LP_{11ax}$ gradually transfers energy to the pulse in $LP_{01x}$. The $LP_{01}$ soliton, which gains energy, becomes increasingly narrower with a higher peak power, to ensure that the soliton order N remains close to 1. While the physical mechanism behind such power transfer is not clearly known, our results show that net energy transfer is always from a higher-order mode to the fundamental mode, which can be interpreted as a sort of self-focusing in multimode fibers. Some recent experimental reports have shown a similar self-focusing or "beam cleanup" in highly multimode fibers [43, 46]. Another possible explanation for such energy transfer is inspired from the thermodynamic effect of condensation of waves [71].

Fig. 3.3b shows the case of two fundamental solitons launched in the degenerate $LP_{11ax}$ and $LP_{11bx}$ modes. Similar to the case shown in Fig. 3.3a, both solitons initially shed some energy in the form of dispersive wave and reshape themselves by becoming narrower because of intermodal XPM. Moreover, they exhibit a periodic evolution pattern which does not stabilize even after propagating a 100 dispersion lengths. However, we do not notice any net energy transfer between the modes. Indeed, our results show that each soliton contains more than 99% of its initial energy, even after propagating for 200 dispersion lengths.

Finally, we also look at the case when three solitons are simultaneously launched in the $LP_{01x}$, $LP_{11ax}$ and $LP_{11bx}$ modes. Fig. 3.4 shows the evolution in that case. We observe behavior similar to Fig. 3.3a. All solitons initially lose some energy followed by a transfer of energy from solitons in both the higher-order modes to the fundamental mode. The main conclusion here is that solitons propagating in the higher-order mode are unstable when there is energy present in the fundamental mode. In contrast, the solition in the fundamental mode is not only stable, but becomes stronger and narrower as energy is transferred to it.

## 3.2 Temporal soliton trapping

In the previous section, we considered solitons propagating simultaneously in different modes of a few-mode fiber. However, we ignored the DGD between these modes. In practice, the presence of DGD will alter their behavior and can possibly lead to reduced nonlinear interaction between modes. Soliton robustness has been studied previously in the case of birefringent fibers having DGD between the two orthogonally polarized modes [72, 73]. In our case, it leads to a group-velocity mismatch between the $\mathrm{LP}_{01}$ and $\mathrm{LP}_{11}$ modes. We quantify this mismatch through the parameter $\delta\beta_1 = \beta_{12} - \beta_{11} = d_{12}T_0/\mathrm{L_D}$. The degenerate $\mathrm{LP}_{11a}$ and $\mathrm{LP}_{11b}$ modes have the same group-velocity.

Fig. 3.5 shows the numerical results for $\delta\beta_1 =$ (a) 10 ps/km and (b) 100 ps/km when fundamental solitons are launched simultaneously into the $\mathrm{LP}_{01}$ and $\mathrm{LP}_{11}$ modes. For the smaller value of $\delta\beta_1 = 10$ ps/km, the soliton in the fundamental mode slows down while the soliton in the higher-order mode speeds up, till they are both traveling at the same speed. This is the phenomenon of soliton trapping that has been observed in birefringent fibers [72], and it is accomplished through shifts in the spectrum of each soliton in opposite directions. Using simple arguments, we can estimate the spectral shift as $\Delta\omega = \Delta\beta_1/\beta_2 = \mathrm{L_D}\Delta\beta_1/T_0^2$. For the parameters used in Fig. 3.5(a), the estimated shift in the frequency is about 40 GHz. A comparison of Fig. 3.3(a) and Fig. 3.5(a) shows that apart from the trapping and a temporal tilt induced by spectral shifts, the two solitons evolve in a similar fashion. In particular, the $\mathrm{LP}_{11}$ soliton remains unstable and transfers its energy to the $\mathrm{LP}_{01}$ soliton as it propagates along the fiber.

As the group-velocity mismatch between the two modes increases, one would expect the soliton trapping to become less effective. For a sufficiently large value of $\delta\beta_1$, trapping should cease completely. The reason behind this thinking is that the two solitons overlap temporally over shorter and shorter distances as the DGD parameter increases, making intermodal XPM less and less effective. Numerical results confirm this behavior. Fig. 3.5(b) shows the case where $\delta\beta_1 = 100$ ps/km and we can see that soliton trapping has nearly ceased to occur in this scenario. In this particular case, the solitons have separated temporally before propagating even half a dispersion length. Remarkably, even within such a short distance, the spectrum of the solitons have shifted slightly, evident by the tilt in the temporal evolution of the fundamental mode. Also note that the soliton in the higher-order mode no longer transfers energy to the soliton in the fundamental mode. This is because they are no longer coupled through XPM since they separate temporally.

## 3.3 Spatiotemporal solitons

So far, we have looked at how stable solitons are when launched in any given mode of a multimode fiber. We looked at this with and without the presence of solitons in the other fiber modes. We could observe intermodal nonlinear effects in action, specifically intermodal XPM, which led the solitons to shed some energy and reshape themselves. In addition, we also found that light pulses present in different modes can be trapped with each other. These effects can lead us to ask the next logical question: Can we realize

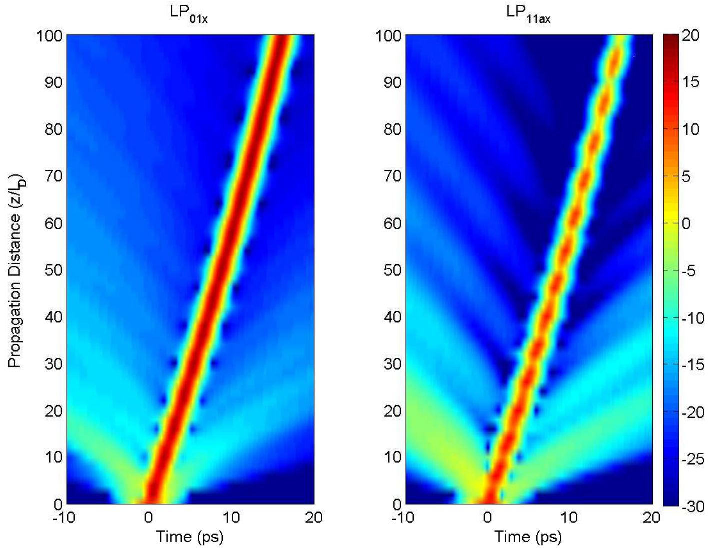


(a)

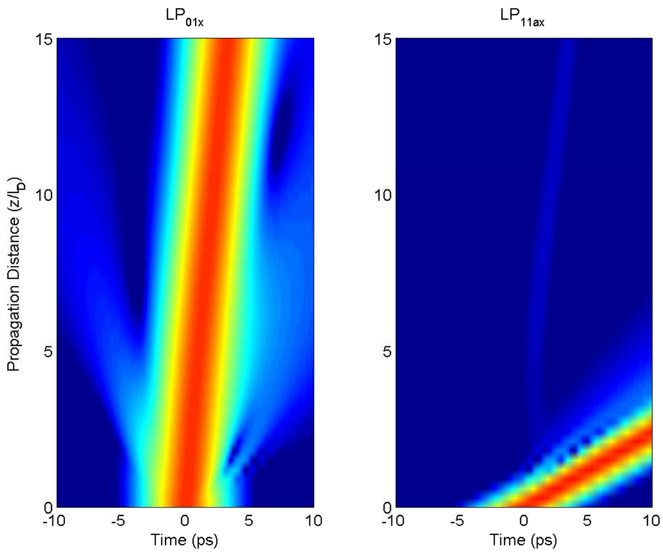


(b)

*Fig. 3.5:* Simultaneous propagation of fundamental solitons in $LP_{01x}$ and $LP_{11ax}$ modes with (a) $\delta\beta_1 = 10$ ps/km and (b)$\delta\beta_1 = 100$ ps/km. (Colorbar represents power in dB)

a temporal solitonic pulse that also spans over multiple spatial modes of a fiber, or a spatiotemporal soliton?

As the nonlinearity cancels out the effect of group-velocity dispersion for single-mode solitons, we would require the intermodal nonlinearity to cancel out modal dispersion to realize multimode solitons. Indeed, this line of thinking is not novel. There have been a few reports of spatiotemporal solitons existing in multimode nonlinear media in the past [74–77]. But this field of study has been taken up with new vigor lately, as multimode fibers become more relevant. Recent experimental studies have shown the first reports of observing spatiotemporal solitons in the lab [32, 35, 44]. These results, using a graded-index fiber supporting up to 10 modes, clearly show how such spatiotemporal solitons form. The energy that is initially coupled into each mode starts to separate in time owing to

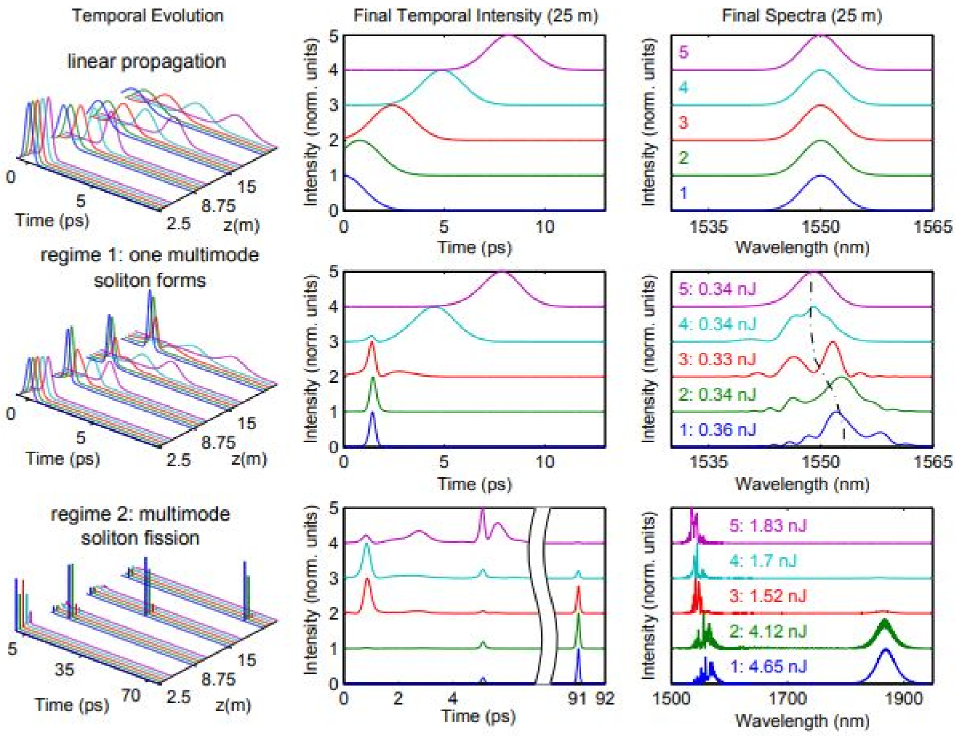


*Fig. 3.6:* (From [35]) Numerical simulation for 25 m propagation of a pulse equally distributed amongst the first 5 modes of a graded index fiber (zero angular momentum modes). The initial pulse has a duration of 500 fs and is centered around 1550 nm. *Left column*: normalized temporal evolution of each mode. *Middle column*: normalized temporal profiles at the end of 25 m (linear scale). *Right column*: normalized spectra at the end of 25 m. For the temporal evolution plots, the distributions are plotted for 2.5, 8.75, 15 and 21.25 m. The modes are color-coded as in adjacent plots, and offset along the distance axis slightly to increase visibility. *Top row*: linear propagation regime. *Middle row*: nonlinear propagation regime 1: each mode seeded with 0.34 nJ pulse energy. A dotted line shows the center wavelength in each mode. *Bottom row*: nonlinear propagation regime 2: each mode seeded with 2.74 nJ pulse energy.

intermodal DGD. But, intermodal nonlinearities can trap energy components in different modes, thereby temporally localizing that energy packet. As we have shown earlier, the pulses need to shift their spectrum to accommodate the change in group-velocity that accompanies trapping. If a group of such synchronized pulse components gets enough energy to form a soliton, it gets localized in the spatial dimension as well. This packet then propagates relatively unchanged, or displays periodic oscillatory behavior. Fig. 3.6, from [35], shows the formation of spatiotemporal solitons when light is launched into the first 5 azimuthally symmetric modes of a graded-index fiber. Such spatiotemporally localized packets of energy have also been called "light bullets" or multimode solitons. These multimode solitons can be comprised of different combinations of spatial modes.

While we mostly consider a two spatial mode fiber ($LP_{01}$ and $LP_{11}$) to study solitons, we observe the formation of multimode solitons even in this simple case. In fact, the case shown in Fig. 3.3(b), where two fundamental solitons are launched in each degenerate $LP_{11}$ mode, can be interpreted as a second-order soliton spanning both the modes. Modes that have a smaller difference in propagation constants are more likely to form multimode solitons.

## Conclusions

In this chapter, we have addressed the issue of the existence and stability of solitons in few-mode fibers using a three-mode fiber as an example. We found that when a single fundamental or higher-order soliton is launched into any given fiber mode, it can propagate stably over long fiber lengths, even though intermodal nonlinear effects are seeded through noise. If we launch two solitons simultaneously in the orthogonally polarized components of a single mode, the nonlinear birefringence induced through intramodal XPM makes the solitons evolve such that their widths oscillate periodically. We have not shown this case here as this has been dealt with in the past in detail [69, 72]. Finally, when two co-polarized solitons are launched into different fiber modes, their evolution depends on the amount of DGD between the modes. For small values of DGD, the solitons propagating in different modes are found to trap with each other such that they shift their spectra and travel at the same speed in spite of considerable DGD between them. For the fiber considered here, we could observe complete trapping for DGD values as high as 20 ps/km. A surprising feature that our simulations revealed is that under certain conditions, pulses propagating in higher-order modes may transfer their energy into the fundamental mode as they propagate along the fiber. Finally, we briefly discussed an extension of this concept of soliton propagation in multimode fibers, known as spatiotemporal or multimode solitons. Multimode solitons occur when the intramodal nonlinearity and intermodal nonlinearity counteract group-velocity dispersion and modal dispersion respectively.

# Chapter 4

# Impact of Kerr nonlinearity on intermodal soliton interaction

In the previous chapter, we discussed the existence of solitons and their stability in a multi-mode environment. In this chapter and the next, we will consider a scenario where two temporally separated solitons propagate simultaneously in an optical fiber and try to understand the nonlinear interaction between them.

Interaction between temporally separated solitons because of the nonlinear Kerr effect is well-documented in the case of single-mode fibers [78–88], however, soliton interaction in multimode fibers hasn't been thoroughly investigated. Here, we study in detail how temporally separated solitons, launched individually in degenerate or nearly-degenerate modes of a multimode fiber, interact with each other owing to the nonlinear Kerr effect.

The fiber that we use to study this behavior is identical to the one that was modeled in chapter 3. To recall, it is a two-mode fiber, which after including the degeneracy of the $LP_{11}$ modes and accounting for both polarizations, supports a total of six modes. But it is important to note that the governing equations remain the same even for a fiber that is highly multimodal. The results found here will remain the same for any higher or lower order pair of degenerate or nearly-degenerate modes that exist in a step-index or graded-index fiber, as long as those two modes are the only ones that are being excited. To look at the temporal evolution of the power in each mode, we use six coupled NLS equations [eq. (2.20)] and solve them numerically using the split-step Fourier method described in chapter 3. We do not include higher-order effects like Raman (included in chapter 5) and shock terms and only consider dispersion up to second-order.

In section 4.1, we first consider the impact of Kerr nonlinearity on interaction between temporally separated solitons propagating in degenerate modes of a multimode fiber. In section 4.2, we study the impact that input parameters like relative phase, relative amplitude and temporal separation have on this interaction behavior. We consider non-degeneracy between the modes and its effect on intermodal soliton interaction in section 4.3. Finally, we summarize the results.

## 4.1 Soliton interaction in first-order degenerate modes

We numerically study how soliton pulses launched simultaneously in degenerate modes of a fiber interact and how this interaction depends on their initial pulse parameters. The degenerate modes used for the following results are the $LP_{11a}$ and $LP_{11b}$ modes, although, as mentioned previously, these results would qualitatively be similar for any pair of degenerate modes in a multimode fiber.

We consider the simplest case of two fundamental solitons launched in the two degenerate modes individually, with a delay $T_s$ between them. The input, therefore, is of the form: $\mathrm{sech}[(\tau - q_0)]$ in the $LP_{11a}$ mode and $\mathrm{sech}[(\tau + q_0)] \exp(\imath\theta)$ in the $LP_{11b}$ mode. Here, $\theta$ corresponds to the relative phase between the modes at the time of launch; $\tau = t/T_0$ and $q_0 = T_s/2T_0$ are the normalized time parameters related to the input pulse width $T_0$ and the initial temporal pulse separation $T_s$.

Using mode 2 as the reference mode and assuming no power in mode 1, eq. (2.20) leads to the following set of coupled equations:

$$\frac{\partial \mathbf{u}_2}{\partial \xi} + i\frac{d_{22}}{2}\frac{\partial^2 \mathbf{u}_2}{\partial \tau^2} = i\mathrm{N}_2^2\left[f_{2222}|\mathbf{u}_2|^2\mathbf{u}_2 + (f_{3322} + f_{3232})|\mathbf{u}_3|^2\mathbf{u}_2 + f_{2332}\mathbf{u}_3^2\mathbf{u}_2^*\right], \qquad (4.1a)$$

$$\frac{\partial \mathbf{u}_3}{\partial \xi} + i\frac{d_{23}}{2}\frac{\partial^2 \mathbf{u}_3}{\partial \tau^2} = i\mathrm{N}_3^2\left[f_{3333}|\mathbf{u}_3|^2\mathbf{u}_3 + (f_{2233} + f_{2323})|\mathbf{u}_2|^2\mathbf{u}_3 + f_{3223}\mathbf{u}_2^2\mathbf{u}_3^*\right]. \qquad (4.1b)$$

The first-order time derivatives do not appear in these equations because the group-velocity is the same for all modes belonging to the $LP_{11}$ mode group. $N_2$ and $N_3$ correspond to the soliton order in the $LP_{11a}$ and $LP_{11b}$ modes respectively.

We numerically solve this set of coupled equations using the split-step Fourier method described in chapter 2. For the results shown in this chapter, we have used the fiber nonlinear coupling parameters from Table 3.1. For an input wavelength $\lambda_0 = 1540$ nm, the nonlinear parameter is chosen to be $\gamma = 1.77$ 1/W-km and the group-velocity dispersion parameters as $\beta_{22} = \beta_{23} =$ -24.3 ps$^2$/km. The Raman scattering term is ignored ($f_R = 0$) and its impact on soliton interaction will be studied in detail in the next chapter.

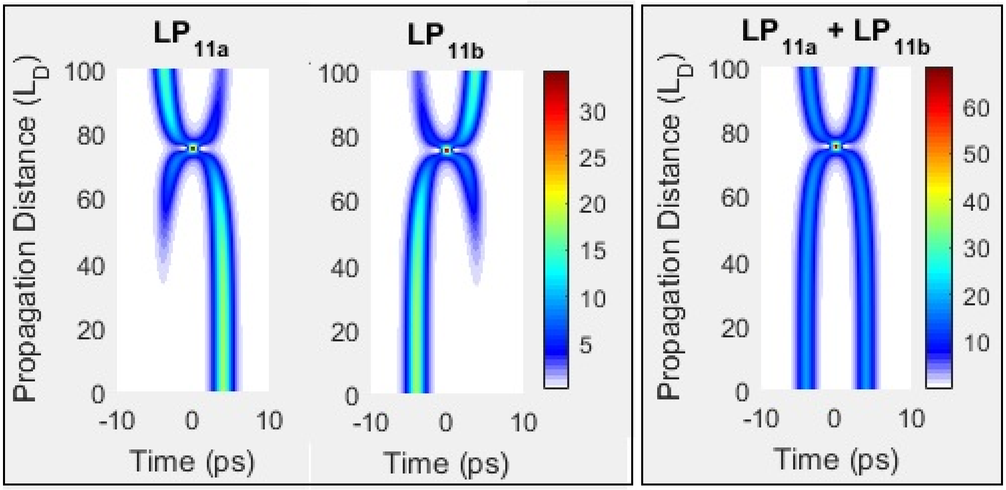


*Fig. 4.1:* Interaction of two temporally separated solitons launched in degenerate modes. (*Left*) Evolution of power in individual modes (*Right*) Sum of power in both modes. The color bar shows optical power on a linear scale.

First, we look at two in-phase fundamental solitons launched in the two first-order degenerate modes. For this case, we set $T_0 = 1$ ps, $q_0 = 4$ and $\theta = 0$, which represents two in-phase solitons separated by 8 ps initially. The dispersion length ($L_D$) is about 40 m in this case. The first two panels of Fig. 4.1 show the evolution of these solions in the few-mode fiber over 100 $L_D$, while the third panel shows the evolution of the total power in both modes.

To compare the intermodal interaction behavior to the intramodal interaction observed in single-mode fibers (SMF), Fig. 4.2 shows evolution of two temporally separated first-order solitons with $q_0 = 4$ in a SMF. Similar to what is observed in SMFs (Fig. 4.2), the two solitons initially attract each other, even though they belong to different modes. Indeed, the total power in both modes for the two-mode case (last panel in Fig. 4.1) evolves in a qualitatively identical manner to the evolution observed in SMF (Fig. 4.2).

In two-mode case, solitons attract through intermodal Kerr nonlineality. However, unlike the single-mode case, we find that solitons transfer some of its power to the other mode as the two solitons approach each other. Eventually, the two solitons overlap completely, forming an intense bimodal pulse at around 75 $L_D$. At this point, each pulse is significantly narrower than the input pulse and also has a wider spectrum. On further propagation, both pulses cross over into the other mode and start to separate from each other, almost returning to their initial temporal separation at a distance of 150 $L_D$. However, we stress that input conditions are never fully recovered because some energy remains in the original time slot.

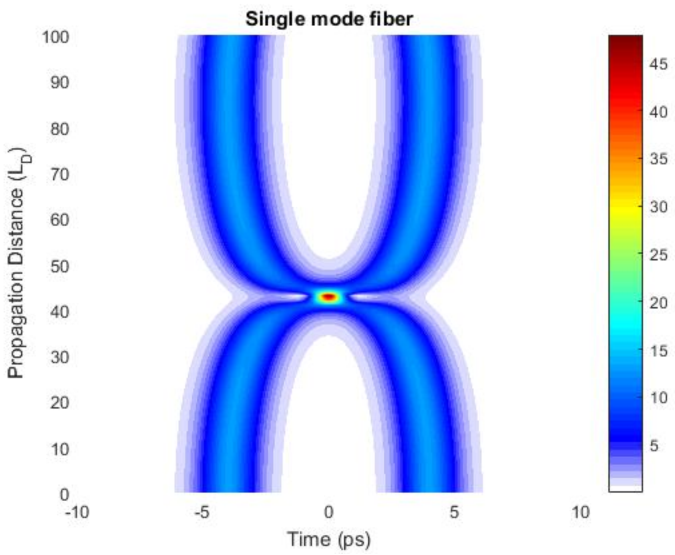


*Fig. 4.2:* Temporal evolution showing soliton interaction in a single-mode fiber. Input conditions are N = 1, $T_0$ = 1 ps, $q_0$ = 4 and $\theta$ = 0. The color bar shows power range on a linear scale.

Interaction behavior shown in Fig. 4.1 is similar to what is observed in SMFs, with some obvious differences. The main difference is that there is an intermodal exchange of power during the initial attraction phase. The underlying physical mechanism behind this energy transfer is intermodal four-wave mixing (FWM), governed by the last term in eqns. (4.1), which causes a part of the energy from one mode to be transferred to the other mode. If we plot this evolution on a logarithmic scale, we note that this power transfer begins right after the pulses are launched, but it becomes a noticeable fraction of the initial peak power only around 30 $L_D$.

Figure 4.3 shows the evolution of the power in mode 2 ($LP_{11a}$) in the range 60-85 $L_D$, which includes the part in the which the solitons "collide" and overlap temporally. Power variations in modes 3 ($LP_{11b}$) are just a mirror image of Fig. 4.3 around $\tau = 0$. The smaller peak on the left is due to the intermodal power transfer occurring from the neighboring mode. One can see that it grows in magnitude while the peak on the right weakens, because of a continuous transfer of power from that pulse to the other mode. The reason why this weak pulse also moves towards the center is that it is trapped by the soliton in mode 3, a phenomenon whose occurrence was explained in detail in chapter 2. Even after the point of collision, once the pulses cross over and start to temporally

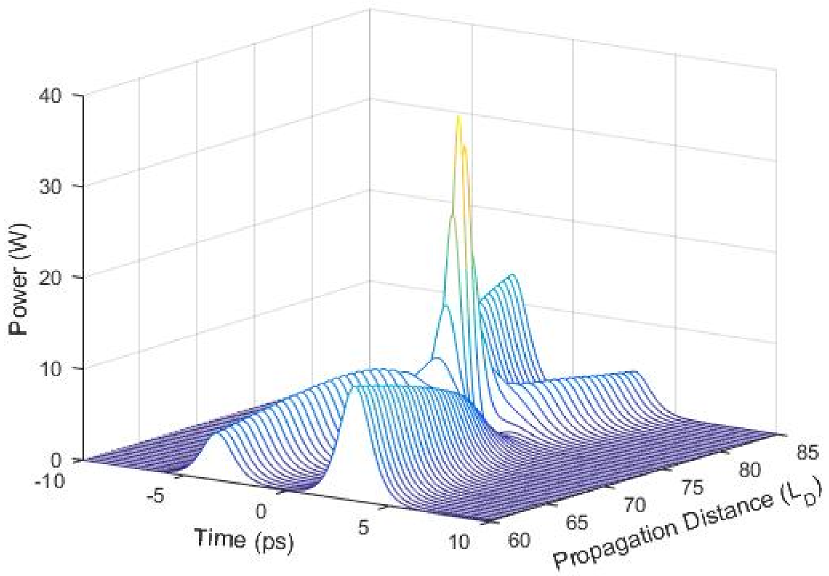


*Fig. 4.3:* Magnified view of the $LP_{11a}$ mode power between 60 to 85 $L_D$, a range that includes the point of collision. The peak initially on the left is due to intermodal power transfer from the $LP_{11b}$ mode.

separate from each other, a small portion of the energy in mode 2 stays trapped with the pulse propagating in mode 3 (and vice versa). However, if we look at the total power in both modes (last panel in Fig. 4.2), the behavior seems almost indistinguishable from the case of SMFs. This is surprising but also reassuring, since the energy of the two solitons must be conserved in the absence of losses. This similarity between the SMF case and the degenerate modes of an MMF has also been noted in the strong-coupling regime when linear coupling is included [30].

One way to understand the features seen in Figs. 4.2 and 4.3 is through the concept of a multimode soliton that was discussed in section 3.3. In this picture, even though a fraction of the soliton's energy is transferred to the other mode, both fractions remain a part of the same "bimodal" soliton. Since the modes are assumed to be perfectly degenerate, the exchange of power due to intermodal FWM is equal in both directions and hence the total energy in each mode is conserved. Interestingly, we do not observe any "ghost pulses" like the ones observed in intrachannel FWM [89, 90] studied in the context of telecommunication systems.

## 4.2 Impact of pulse parameters

We looked at interaction of temporally separated but identical in-phase solitons. Now we study what happens when the relative phase, amplitude or temporal separation between the two interacting solitons is varied.

### 4.2.1 Impact of relative phase

In the case of SMFs, soliton interaction is found to be quite sensitive to relative phase $\theta$. For this reason, we expect qualitative changes to occur with changes in $\theta$ even for the case of MMFs. Figure 4.4 shows the effect of changing $\theta$ while keeping the same value of $q_0 = 4$ for the initial temporal separation. For $\theta = \pi/8$ (*top row*) and $\pi/4$ (*middle row*), the solitons still experience intermodal attraction initially, but they separate from each other and never appear to collide. Indeed, the last panels where total power in the two modes is plotted exhibit features that are almost identical to the single-mode case. In fact, these are out-of-phase collisions [91], which occur when the two colliding solitons do not have identical phase. Temporally, solitons that collide out-of-phase never overlap completely at the point of collision. However, when we look at the mode powers in each mode individually, we find remarkably new features. Intermodal power transfer similar to that seen in Fig. 4.2 still occurs and it does depend to some extent on the exact value of $\theta$. Around 75 $\mathrm{L_D}$, the distance where solitons crossed over in the in-phase case, we observe that, despite the absence of complete temporal overlap of the two solitons, the entire mode power has shifted temporally to the other side. This feature is hard to understand. One possibility is that intermodal FWM becomes so strong that it transfers the entire power in mode 2 to mode 3 (and *vice versa*). A second possibility is to invoke the formation of multimode solitons and only consider the sum of powers in the two modes as a relevant quantity.

Another remarkable feature in Fig. 4.4 is the temporal asymmetry seen clearly in the last panel of the top row. We can see that the trace on the left is more intense than on the right after the two pulses have collided. Thus, even if we interpret the soliton interaction in terms of multimode solitons, intermodal FWM is not symmetric when $\theta \neq 0$. More power is transferred to the soliton on the left, making it more intense. This asymmetry is also present in individual mode powers. If we look carefully, the direction of power transfer is not uniform, which leads to one mode having more energy compared to the other mode. In other words, the energy within a mode is not conserved while the total energy in the fiber is conserved.

We have verified that this asymmetry is observed even in SMFs and is dependent on the sign of $\theta$. Indeed, when we change the sign such that $\theta = -\pi/8$, we find that the soliton on the right is more intense than the one on the left. This means that not only the magnitude of the phase but also its sign plays a role in deciding which mode is preferred by intermodal FWM.

The bottom row in Fig. 4.4 shows the case of $\pi/2$. For this specific value of $\theta$, both solitons appear to propagate without any interaction, as if the other soliton did not exist. This behavior is different from what is observed in SMFs. In that case, solitons experience repulsion and monotonically move away from each other for $\theta = \pi/2$. The physical reason for why the MMF case is different is not fully understood at this time. One factor that may contribute to this difference is the partial overlap spatial overlap between the modes compared to the 100% overlap in SMFs.

### 4.2.2 Impact of temporal pulse separation

We also look at the impact of varying the initial temporal separation $q_0$. The first plot in Fig. 4.5 shows how the spacing between the two solitons changes as they propagate down the fiber for three values of $\theta$ while choosing $q_0 = 4$. The spacing goes to 0 only for $\theta = 0$ at a certain distance where the two solitons overalp completely (or in-phase collision).

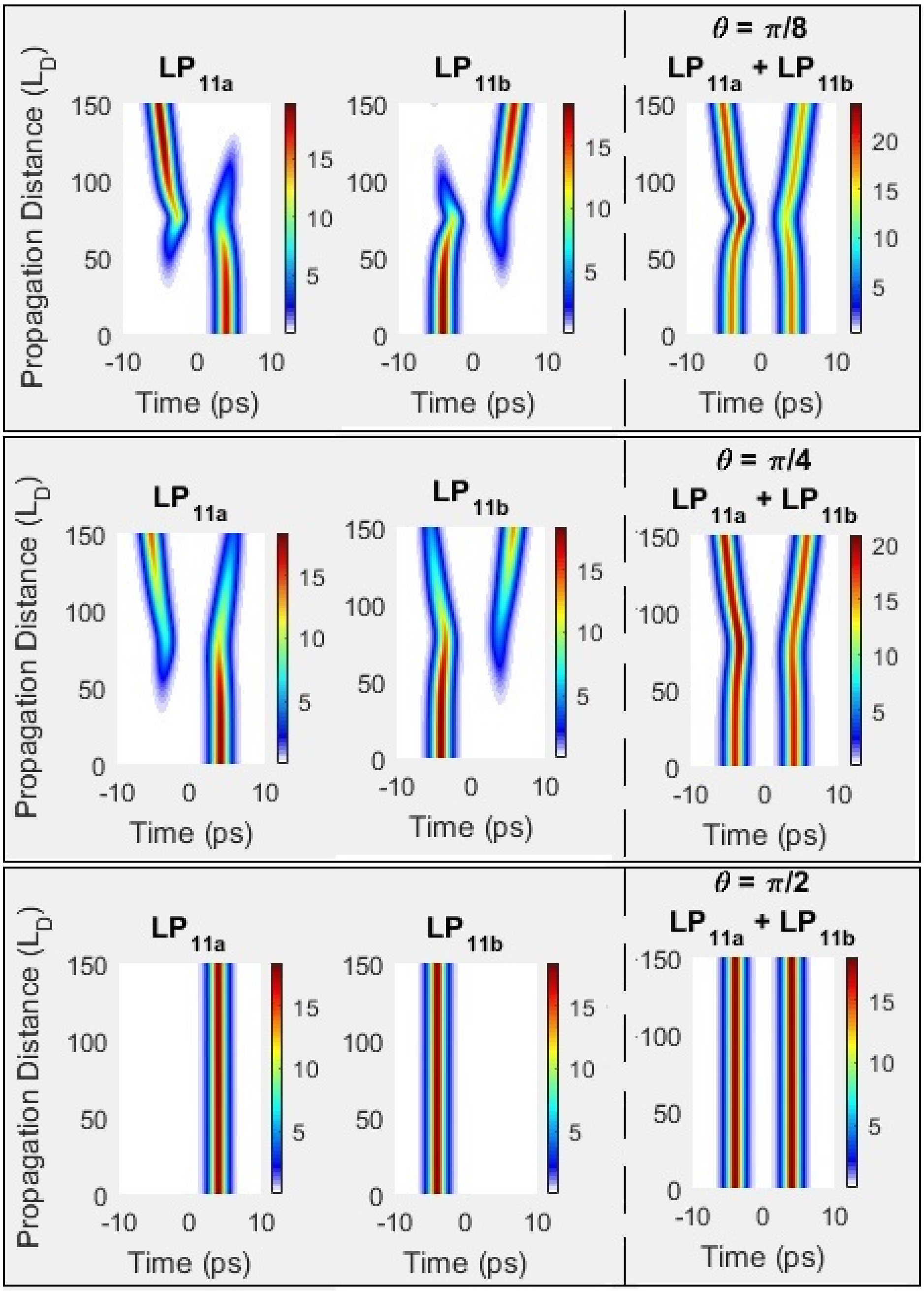


*Fig. 4.4:* Effects of initial phase difference on intermodal soliton interaction: (*top row*) $\theta = \pi/8$, (*middle row*) $\theta = \pi/4$, (*bottom row*) $\theta = \pi/2$. Color bar shows power on a linear scale.

In the case of $\theta = 0$, the qualitative behavior remains identical to that seen in Fig. 4.2 for other values of $q_0$ except that the two solitons collide after a shorter distance for smaller values of $q_0$. This dependence on $q_0$ is shown in the second plot in Fig. 4.5. Similar to the single-mode case, the collision distance depends exponentially on $q_0$, as verified by an exponential fit to the numerical data (dashed line). One may also ask whether the periodic interaction behavior observed in SMFs holds in the case of MMFs. To answer this question, we reduce the initial separation $2q_0$ between the two solitons so that they collide at a much shorter distance and propagate them long enough to record several collisions. Figure 4.6 shows the results of plotting the bimodal evolution for $q_0 = 2$ and 3. Clearly, intermodal

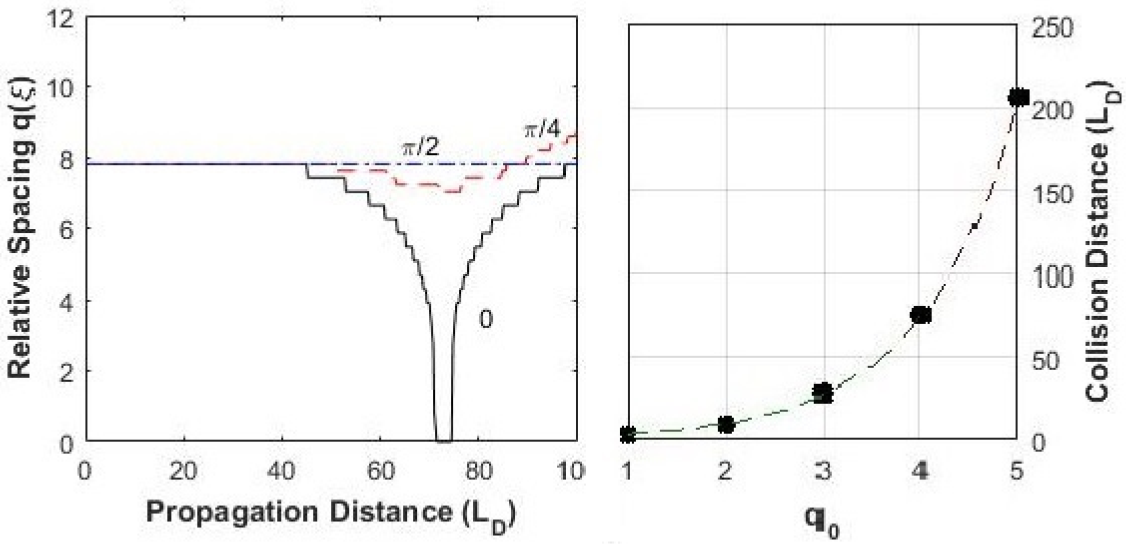


*Fig. 4.5:* (*Left*) Spacing between the two solitons as a function of propagation distance for three values of $\theta$. (*right*) Dependence of collision distance on the initial pulse separation for two in-phase solitons. The dashed line shows an exponential fit to the numerical data.

interaction of two in-phase solitons inside a MMF is far from being periodic. As seen in Fig. 4.6, successive collisions occur after increasingly shorter distances. This breakdown in periodicity is certainly a consequence of the intermodal FWM between modes. Because of this phenomenon, after the first collision, each mode has two pulses propagating through it, one of which is the soliton that is initially launched into that mode and the other forms due to the energy transfer from the other mode. As a result, each pulse experiences not only intermodal nonlinear coupling but also intramodal nonlinear coupling, and thus the initial conditions are not reproduced after the first collision, unlike in SMFs. It is thus not surprising that the interaction behavior is not periodic in MMFs.

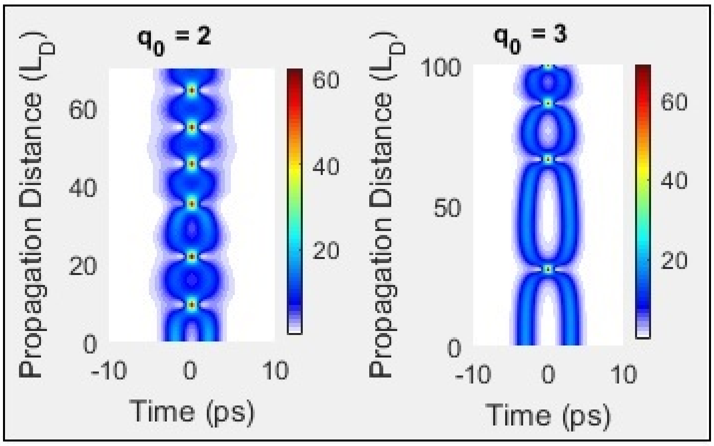


*Fig. 4.6:* Breakdown of periodicity in intermodal soliton interaction for in-phase solitons. Total power in the two degenerate modes is plotted as a function of distance for $q_0 = 2$ and 3. Color bar shows power on a linear scale.

### 4.2.3 Impact of relative amplitude

As with the SMF case [1], we also expect the interaction to depend on the relative amplitudes of the two solitons. We studied the amplitude dependence in the two-mode case by changing the peak powers that affect the soliton orders $N_2$ and $N_3$ associated with the two pulses. To emphasize the bimodal nature of the solitons, Fig. 4.7 shows how the total power in the two modes varies over $100L_D$ for the case of $N_2 = 1$ and $N_3 = 1.1$ after choosing $q_0 = 4$ and $\theta = 0$. Unlike the case of equal amplitude solitons, the two bimodal solitons never collide and exhibit oscillatory behavior with distance. These results indicate that the amplitudes and phase of the input pulses can thus be used to control the interaction process in MMFs.

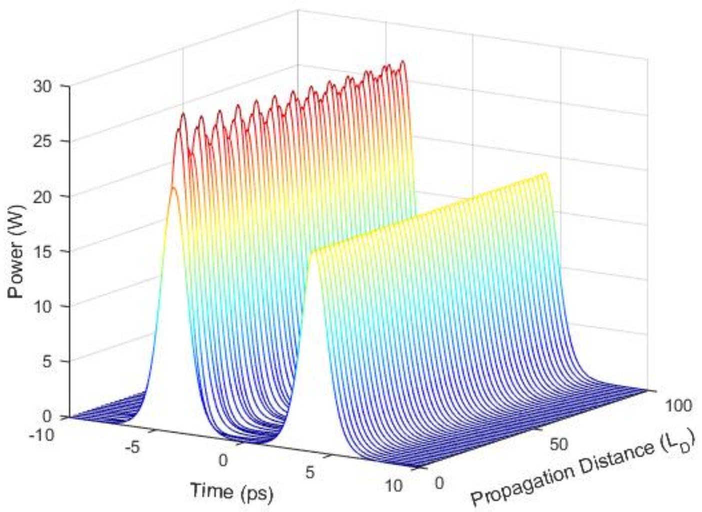


*Fig. 4.7:* Intermodal interaction of two in-phase solitons of the same width with different amplitudes ($N_2 = 1$, $N_3 = 1.1$). Total power in both modes is plotted as a function of distance.

## 4.3 Soliton interaction in nearly degenerate modes

In this section, we investigate how the interaction behavior changes when the two modes are not exactly degenerate ($\beta_2 \neq \beta_3$). One expects the behavior to be very similar to the case of degenerate modes for relatively small deviations in propagation constants. We also expect the collisions to be out-of-phase, since the modes have slightly different propagation constants. But the question is, how much deviation is tolerable? Since $\beta_2$ is not expected to change much for small deviations, we try to answer this question numerically through two parameters defined as $\Delta\beta_0 = \beta_{02} - \beta_{03}$ and $\Delta\beta_1 = \beta_{12} - \beta_{13}$, the latter representing the DGD between the two nearly-degenerate modes. Figure 4.8(a) shows the evolution of individual mode powers and the total bimodal power over 300 $L_D$, with conditions identical to Fig. 4.2 except that $\Delta\beta_0$ now has a finite value of 0.1 $m^{-1}$. The bimodal picture shows an initial attraction phase leading to a near collision (out-of-phase collision) between the two bimodal solitons around 75 $L_D$, after which they separate from each other. The individual mode powers, however, show even more drastic changes caused by the slightly different propagation constants. After the first collision, each mode repetitively transfers power to the other mode back and forth, but the two modes do not behave in a symmetric fashion.

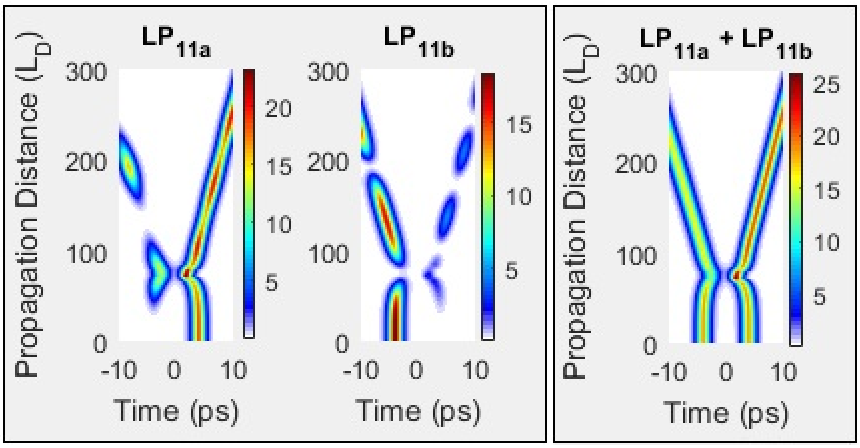


(a)

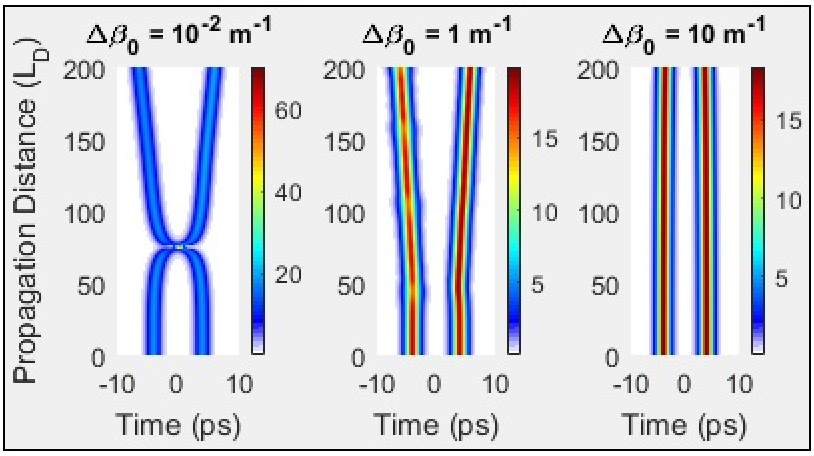


(b)

*Fig. 4.8:* Interaction of two in-phase solitons propagating in nearly degenerate modes with pulse parameters identical to those used in Fig. 4.2. (a) Evolution of individual mode powers and total bimodal power over 300 $L_D$ for $\Delta\beta_0 = 0.1$ m$^{-1}$. (b) Total power in both modes for three values of $\Delta\beta_0$

Indeed, as seen in Fig. 4.8(a), the $LP_{11a}$ mode becomes more intense compared to the other mode after the attraction phase. Similar to the case of initial phase difference $\theta$ studied in the previous section, the sign of $\Delta\beta_0$ determines which mode is preferred. When we reverse the sign of $\Delta\beta_0$, it is the $LP_{11b}$ mode that ends up becoming more intense after the collision.

To quantify the tolerable values of $\Delta\beta_0$, Fig. 4.8(b) shows the evolution of total bimodal power over 200 $L_D$ for three values of $\Delta\beta_0$ ranging from 0.01 to 10 m$^{-1}$ while keeping the other parameters same as in Fig. 4.2. For the smallest value of $\Delta\beta_0$, the behavior is initially similar to the case of degenerate modes shown in Fig. 4.2. But even for this case, the behavior changes after the collision since the bimodal solitons repel each other and do not collide again. Further increasing $\Delta\beta_0$ leads to weaker nonlinear coupling and even the initial collision ceases to occur. After $\Delta\beta_0$ exceeds 5 m$^{-1}$, the two bimodal solitons propagate independently as if they were isolated from each other. We thus conclude that the intermodal collision of two in-phase solitons requires the ratio $|\Delta\beta_0|/\beta_{02}$ to be below $10^{-7}$, making it unlikely that it can be observed in real fibers.

We also study the impact of intermodal DGD on soliton interaction. Figure 4.9 shows

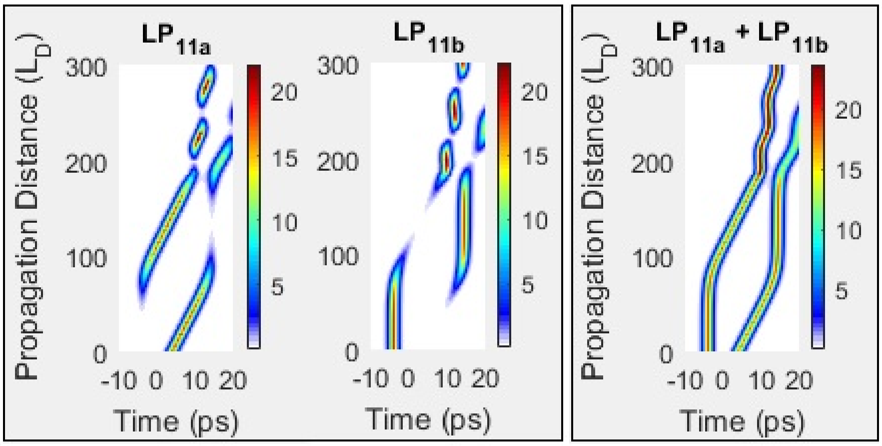


(a)

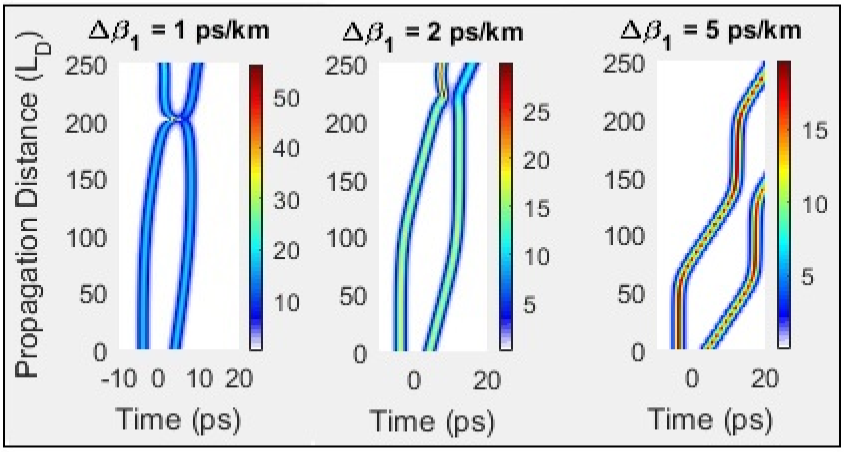


(b)

*Fig. 4.9:* Impact of DGD on the interaction of two in-phase solitons propagating in nearly degenerate modes with pulse parameters identical to those used in Fig. 4.2. (a) Evolution of individual mode powers and total bimodal power over 300 $L_D$ for $\Delta\beta_1 = 3$ ps/km. (b) Total power in both modes for three different DGD values.

soliton interaction for different values of $\Delta\beta_1$. For this figure, the modes are assumed to have the same propagation constant. While such a situation is not realistic, it has been simulated to isolate the impact of DGD on intermodal interaction of solitons. In Fig. 4.9(a), we show the behavior of solitons in individual modes as well as that of two bimodal solitons for $\Delta\beta_1 = 3$ ps/km. As seen there, the individual solitons change their group velocity, one of them speeding up while the other slows down, under the influence of nonlinear coupling. We also observe power being transferred repeatedly from one mode to another. The last panel shows how the bimodal solitons attract each other after they have adjusted their speeds and undergo an out-of-phase collision. After the collision, one of the solitons becomes more intense. Again, the preferential transfer of power is governed by the sign of $\Delta\beta_1$.

Figure 4.9(b) shows the bimodal picture by summing up the power in both modes for three different values of $\Delta\beta_1$ ranging from 1 to 5 ps/km. For a small value of DGD, the solitons exhibit a behavior quite similar to that seen in Fig. 4.2 (no DGD). More specifically, they adjust their speeds quickly to travel at the same speed and collide after some distance because of an attraction between the two bimodal solitons. The behavior here is very similar to the case of in-phase soliton collision, except that the collision occurs at a larger distance. As the magnitude of $\Delta\beta_1$ increases, nonlinear coupling gets weaker, and the collision distance keeps increasing. After a certain value, the nonlinear coupling weakens enough that the solitons no longer undergo collision. For DGD values beyond 10 ps/km, the two solitons do not interact with each other as the pulses cease to have any temporal overlap soon after they are launched.

## Conclusions

In this chapter, we numerically study how Kerr nonlinearity affects the interaction of two temporally separated solitons propagating simultaneously in degenerate or nearly-degenerate modes of a multimode fiber. Similar to the case of SMF, the solitons are found to attract and repel each other depending on the relative phase between the input pulses. However, each soliton is also found to transfer some of its power to the other mode through intermodal FWM. We show that despite this transfer of power, each soliton keeps propagating as a bimodal soliton and interacts with the other bimodal soliton as if they were propagating in a SMF. Indeed, for degenerate modes, the evolution of total power is qualitatively similar to the case of SMF.

We also looked at the impact of relative phase, temporal separation and relative amplitude on the interaction behavior. Asymmetry caused due to relative phase and amplitude drastically impacts soliton interaction. In all cases, bimodal solitons are still formed because of intermodal power transfer through FWM. But the evolution of these bimodal solitons does not coincide with the SMF case over long distances. We found that, unlike in SMFs, the two solitons do not collide periodically.

Finally, we studied how small changes in the propagation constant and group velocity between the modes affects interaction. We found that the difference in propagation constant $\Delta\beta_0$ between the two modes should be a small fraction of the average value ($<10^{-7}$ for the qualitative behavior to remain identical to the degenerate case). In the case of DGD, $\Delta\beta_1$ values of less than 1 ps/km do not affect interaction behavior qualitatively, but the solitons cease to interact for DGD values larger than 10 ps/km.

For realistic fibers, the propagation constants in adjacent modes are usually at least two orders of magnitude larger than the tolerable values of $\Delta\beta_0$ required to observe the interaction behavior shown here. However, degenerate mode-groups that exist under the weakly-guiding approximation or orthogonally polarized degenerate modes are good candidates to observe this phenomenon in the lab. We have verified that all features observed in this paper also hold for the case of two orthogonally polarized modes.

We have studied how nonlinear coupling affects soliton interaction. Another effect that can impede this behavior is linear coupling between modes that is often present in real fibers. However, our study is useful for a fundamental understanding of the formation, evolution and interaction of optical solitons in few-mode fibers.

# Chapter 5

# Impact of Raman scattering on soliton interaction

In chapter 4, we have studied how temporally separated solitons behave when they are simultaneously propagating in two nearly-degenerate modes of a multimode fiber. We focused mostly on the effect of nonlinear coupling due to Kerr nonlinearity. But, as we have discussed earlier in chapter 2, if the temporal pulses are short ($\langle$1ps), higher-order nonlinear effects like the Raman effect start to significantly impact pulse propagation.

In this chapter, we numerically investigate the impact of Raman scattering on the interaction of two temporally separated pulses with identical spectra. To clearly understand the impact of Raman scattering, we study this first in the context of a single-mode fiber (SMF), before finally simulating the case of a multimode fiber. We take into account all interpulse and intrapulse Raman scattering terms in the generalized nonlinear Schrödinger equation (NLSE) and study the interplay between the Kerr, interpulse Raman and intrapulse Raman effects. Considerable differences are observed from the well-known two-soliton interaction behavior caused by the Kerr nonlinearity in SMFs. We study in detail a mechanism for energy transfer from the leading pulse to the trailing pulse caused by the delayed nature of the Raman response. Long-range interactions, where the pulses do not temporally overlap, are shown to not cause any energy transfer but still impact each others' phase owing to the long tail of the Raman response term. We also study the dependence of this behavior on relative phase and amplitude of the two pulses.

In section 5.1, we briefly review how Raman scattering can affect pulse propagation and look at how to include it in the numerical model. In section 5.2, we study in detail two-soliton interaction for the case of in-phase solitons in SMFs and try to gain some analytical insight to understand the numerically observed behavior. In section 5.3, we study the impact of relative phase and amplitude on two-soliton interaction. In section 5.4, we extend our numerical simulation to the case of degenerate modes in a multimode fiber and look at the difference in behavior caused by the Raman term when compared to the Kerr-mediated interaction studied in chapter 4. Finally, we summarize our results.

## 5.1 Review of Raman scattering and its modeling

As we saw in the previous chapter, when two or more closely spaced solitons propagate together inside an optical fiber, they may attract or repel each other, depending on their relative phases. Higher-order dispersive or nonlinear effects like Raman scattering can perturb this behavior. Impact of Raman scattering on soliton interaction has been studied in different contexts in the past [91–104].

While the nonlinear response of a Kerr medium is instantaneous, the Raman response is known to be retarded. Moreover, stimulated Raman scattering can manifest in two different ways. In the case of a relatively wide pump pulse, it leads to the generation of a new pulse at a frequency that is red-shifted from the pump by about 13 THz in the case of silica fibers. However, for pulses shorter than a few picoseconds, the pulse spectrum itself shifts toward the red side in a continuous fashion through intrapulse Raman scattering. Such a Raman-induced frequency shift (RIFS) is also called the self-frequency shift since no other pulse is involved. However, when two or more closely spaced pulses are propagating through the fiber, because of the delayed nature of the Raman response, the leading pulse can affect the trailing pulses through the so-called interpulse Raman scattering. Indeed, such a Raman-induced interaction between two pulses was studied in 2015 inside a gas-filled fiber [97]. It is important to stress that interpulse Raman interaction can occur even when pulses are separated far enough that little temporal overlap occurs between them, as long as their temporal separation is smaller than the Raman response time. However, as we will show later in this chapter, such long-range interactions cannot lead to any energy transfer between the two pulses in silica fibers.

The effects of Raman scattering in optical fibers have been studied in several different contexts. Experimental and numerical studies have shown a clear occurrence of energy transfer between two solitons propagating in a fiber, owing to interpulse Raman effects [102, 103]. This has also been shown to significantly affect collision dynamics. Raman-induced energy transfer between two solitons of different wavelengths has been shown to play a key role in supercontinuum generation in optical fibers [98, 99]. Interpulse Raman scattering has also been studied in the context of wavelength-division multiplexed optical communication systems [93, 94]. More recently, this effect has been shown to underpin the generation of the so-called "rogue" solitons with extreme red-shifts [91, 100, 101]. Most of these studies involve two or more solitons at different wavelengths traveling at different speeds within the fiber, which induces a collision between the pulses.

We will focus on the case of two temporally separated solitons of the same wavelength propagating at the same speed inside a single-mode fiber. As we saw earlier, this case was studied during the 1980s without including the Raman effect [78–88], and two solitons were found to interact substantially only when they were close enough that their tails overlapped significantly. The question we ask is how the Raman effect influences the Kerr-induced nonlinear interaction between the two solitons. We expect interpulse Raman scattering to considerably modify the Kerr-induced interaction between the two solitons. We will consider the case of two pulses with little temporal overlap so that the nonlinear interaction depends solely on interpulse Raman scattering. For closely spaced pulses, the interplay among four-wave mixing (FWM), RIFS, and interpulse Raman scattering should modify the interaction behavior considerably from what has been known previously. Apart from the mutual attraction and repulsion of the two solitons, we also expect to observe energy transfer between them [102, 103], which can affect collision dynamics in the case of two identical solitons.

To model this system, we use eq. (2.17). But since we are only looking at a fiber that supports one mode, after following the normalization procedure shown in chapter 2, we end up with the following equation

$$i\frac{\partial u}{\partial \xi} + \frac{1}{2}\frac{\partial^2 u}{\partial \tau^2} = -N^2 \times \left( u(\xi,\tau) \int_0^\infty R(\tau')|u(\xi,\tau-\tau')|^2 d\tau' \right). \tag{5.1}$$

Recalling from chapter 2, the Raman effects are included through the nonlinear response function $R(t)$ defined as

$$R(t) = (1 - f_R)\delta(t) + f_R h_R(t), \tag{5.2}$$

where $f_R$ represents the fractional contribution of the delayed Raman response to the nonlinear polarization and $h_R$ is the Raman response function related to vibrations of silica molecules. We use its form given in Ref. [62]

$$h_R(t) = (1 - f_b)H_R(t) + f_b[(2\tau_b - t)/\tau_b^2]\exp(-t/\tau_b), \tag{5.3}$$

where $f_b = 0.21$, $\tau_b \approx 96fs$, and $H_R(t)$ has the form

$$H_R(t) = \frac{\tau_1^2 + \tau_2^2}{\tau_1\tau_2^2}\exp\Big(-\frac{t}{\tau_2}\Big)\sin\Big(\frac{t}{\tau_1}\Big), \tag{5.4}$$

with $\tau_1 = 12.2fs$, $\tau_2 = 32fs$ and $f_R = 0.245$.

We solve Eq. (5.1) in the frequency-domain, using the fourth-order Runge Kutta method in the Interaction Picture (RK4-IP) that was described in section 2.3.2, for different input conditions. To study soliton interaction, the input is in the form of two temporally separated pulses that can differ in phase and amplitude but have the same wavelength. More specifically, we use

$$u(0, \tau) = \text{sech}[\tau + q_0] + r\,\text{sech}[r(\tau - q_0)]e^{i\theta}. \tag{5.5}$$

$q_0 = \Delta t_0/2T_0$ depends on the initial temporal separation $\Delta t_0$ between the two pulses, $\theta$ is their relative phase difference, and $r$ is the ratio of their amplitudes at $\xi = 0$. We choose $f_R = 0.245$ when we want to include the Raman term and set $f_R$ to 0 when want to look at only the impact of Kerr nonlinearity. In all simulations we choose $N = 1$ so that each pulse would propagate as a fundamental soliton in the absence of the other. Since we want to study the impact of Raman scattering, we need to choose a shorter input pulse duration than the $T_0$ value of 1 ps that was used in chapter 4. Here we use $T_0 = 100$ fs, a value that corresponds to a full width at half maximum of 176 fs for sech-shape pulses.

## 5.2 Interaction of two in-phase solitons in SMFs

### 5.2.1 Numerical results

We begin by studying how the Raman effect qualitatively changes the nonlinear interaction of two identical in-phase solitons ($\theta = 0$ and $r = 1$) by turning the Raman term on and off through the parameter $f_R$. We choose $q_0 = 3.5$ or $\Delta t_0 = 7T_0$ so that pulse tails overlap to some extent. The top panel of Fig. 5.1 shows the evolution of two solitons over 100 $\mathrm{L_D}$ in the absence of the Raman effect. As seen there, solitons attract each other through the Kerr nonlinearity and collide periodically, the first collision occurring at a distance of about 26 $\mathrm{L_D}$, where the spectrum also broadens considerably. After each collision, the solitons cross over and start to move away from each other till the separation between them equals their initial separation. This process keeps repeating. Indeed, we can see the second collision occurring at a distance of 78 $\mathrm{L_D}$. This behavior is well known and has been studied in detail [78–88]. We have previously shown this behavior in Fig. 4.1.

The bottom panel of Fig. 5.1 shows how this classical interaction behavior changes when the Raman effects are included. As seen there, both solitons slow down as their spectra red-shift because of the RIFS through intrapulse Raman scattering. Temporal separation between the pulses decreases initially owing to the Kerr effect. The solitons come very close to each other near $\xi = 40$, after which they begin to separate. This

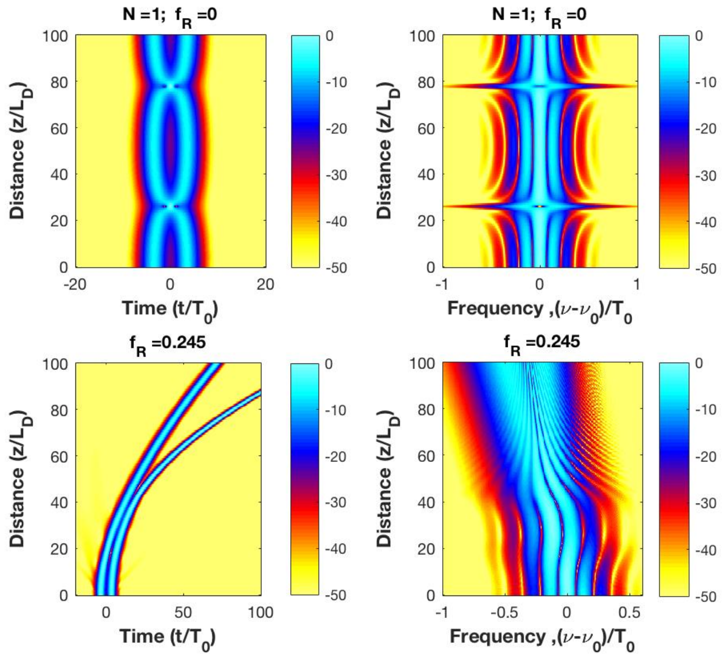


*Fig. 5.1:* Temporal and spectral evolution over 100 $L_D$ of two temporally separated pulses when the Raman term is excluded (*top row*) or included (*bottom row*). The input parameters used are $q_0 = 3.5$, $T_0 = 100$ fs, $\theta = 0$ and $r = 1$. The color bar shows power on a dB scale.

behavior is indicative of an out-of-phase collision [91] and occurs because the two solitons acquire different phase shifts as they propagate owing to the asymmetric nature of the interpulse Raman interaction. The solitons never fully overlap at the point of collision because of the destructive interference caused by the two out-of phase pulses. Moreover, the trailing pulse becomes narrower and its RIFS increases considerably since it scales with the local pulse width $T_s$ as $T_s^{-4}$ [1]. The origin of temporal narrowing is related to the Raman-induced transfer of energy from the leading pulse to the trailing pulse, which must reduce its width to maintain $N = 1$, as required for fundamental solitons. The net result of energy transfer is that the two pulses begin to separate from each other owing to the different RIFS experienced by each pulse. A large RIFS is also apparent from tilting of the spectrum in the last panel in Fig. 5.1. In Fig. 5.2, we quantify the extent of interplay between the Raman and Kerr effects by plotting the temporal separation of two pulses (top) and energy of each pulse (bottom) as a function of distance for the results shown in Fig. 5.1. In this figure, we clearly observe a net transfer of energy to the trailing pulse after $\xi = 25$, but before that distance it is the leading pulse that has more energy than the trailing pulse. To understand this strange behavior, we have to consider how the temporal separation of two pulses changes from its initial value of $2q_0 = 7$. As seen in Fig. 5.2, initially the two pulses move closer due to a Kerr-induced attractive force. At the same time, the spectra of both pulses red-shift owing to the RIFS. Initially the Kerr effect dominates, but the interpulse Raman effects take over beyond $\xi = 20$. In the region between $\xi = 25$ to $\xi = 40$, there is a net energy transfer from the leading pulse to the trailing one, which becomes narrower to remain a soliton and undergoes even more RIFS, resulting in an increasing temporal separation of the two pulses. In short, there is an initial phase of attraction between the pulses, followed by an out-of-phase collision, after

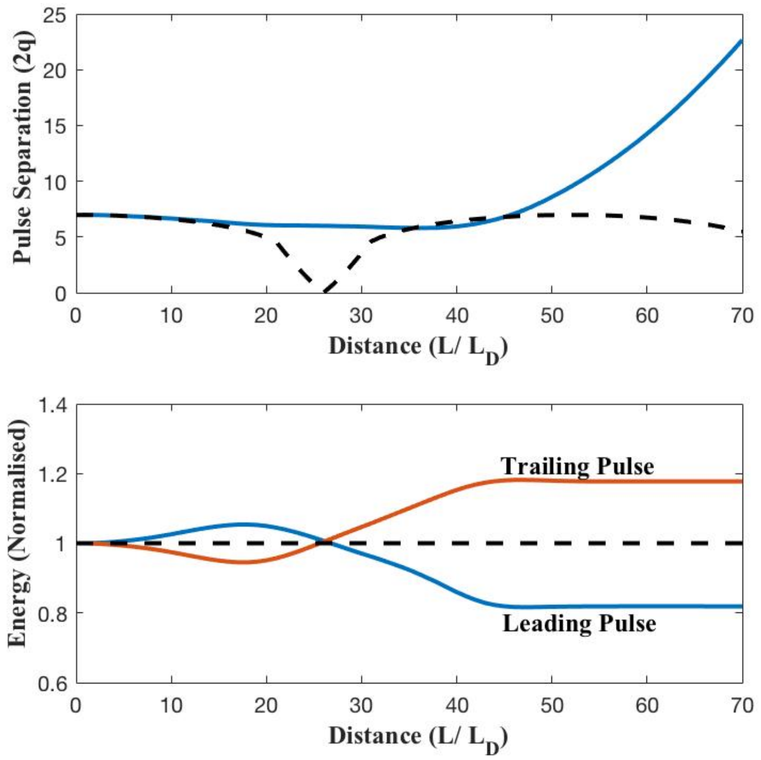


*Fig. 5.2:* Separation ($2q$) between two pulses (*top*) and energy in each pulse (*bottom*) as a function of distance $\xi$ for the case shown in the bottom row of fig. 5.1. The dotted lines show the corresponding plot when the Raman effect is not included ($f_R = 0$). No net energy transfer is observed in that case.

which the two pulses move away from each other owing to the energy transfer initiated by interpulse Raman scattering. Once they start moving apart, the Kerr effect weakens even more. The pulses eventually drift apart and stop interacting, with the trailing pulse becoming narrower and more intense than the leading pulse.

To understand why there is a net transfer of power from the leading to the trailing pulse, we need to consider the physics behind Raman scattering that leads to an asymmetry between the pulses. Even though both pulses induce molecular vibrations in the medium, the molecular vibrations induced by the leading pulse affect the trailing pulse much more than the other way around. Thus, because of the delayed nature of the Raman effect, some energy of the leading pulse used to excite molecular vibrations is transferred to the trailing pulse through Raman amplification. In a recent work, leading pulse affected the trailing pulse through Raman-induced soliton interaction inside a gas-filled fiber [97].

Since we expect that a similar mechanism is at play in silica fibers, we should be able to see some Raman-induced interaction between the two input pulses that are separated far enough that Kerr-induced attraction is negligible between them. Figure 5.3 shows the temporal and spectral evolutions when the two pulses are initially separated by $16T_0$ (1.6 ps for $T_0 = 0.1$ ps) so that there is negligible overlap between them. The solitons still influence each other, but this is limited to a Raman-induced perturbation that forces pulses to shed some energy early on, after which they reshape to form Raman solitons whose spectra red-shift continually. Both the intrapulse and interpulse Raman effects are at play here. The asymmetric nature of the interpulse Raman interaction leads to slightly different red-shifts

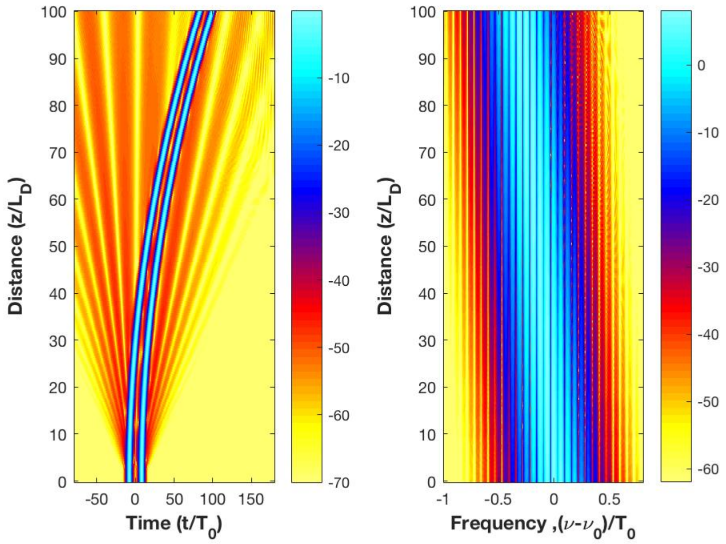


*Fig. 5.3:* Temporal (*left*) and spectral (*right*) evolution of two widely separated solitons with $q_0 = 8$. All other parameters remain the same as in fig. 5.1, bottom row. The color bar shows power on a dB scale.

for the two pulses (resulting from the intrapulse Raman effect). Since the radiation is emitted at different frequencies, its interference produces the temporal fringe-pattern seen in Fig. 5.3. The spectral fringes, on the other hand, result from beating of two temporally separated solitons, which maintain their temporal separation as they propagate along the fiber. Such long-range interactions can occur as long as temporal separation of the two pulses is within the Raman response time (∼1 ps for silica fibers). Somewhat surprisingly, we do not observe any energy transfer between the pulses for such interactions. As we will see later, interpulse Raman scattering responsible for energy transfer requires some temporal overlap between the pulses.

### 5.2.2 Some analytical insight

Two distinct nonlinear effects can lead to energy transfer among temporally separated optical pulses. One of them is interpulse FWM (related to the Kerr nonlinearity) that transfers energy from one pulse to its two neighboring pulses in a symmetric fashion. The other is interpulse Raman scattering, a nonlinear process that is inherently asymmetric because of its delayed nature. In this case, there is a net transfer of energy from the leading pulse to the trailing pulses through the onset of molecular vibrations. The combined effect of the two phenomena depends on the initial conditions. To understand how the competing Raman and Kerr nonlinearities affect soliton interaction, we need to isolate their contributions.

If we write the input field in the form $u(0,\tau) = u_1(0,\tau) + u_2(0,\tau)$, where $u_1$ and $u_2$ correspond to two temporally separated pulses, and substitute this form in Eq. (5.1), we get two coupled equations. The equation for $u_1$ can be written as

$$i\frac{\partial u_1}{\partial \xi} + \frac{1}{2}\frac{\partial^2 u_1}{\partial \tau^2} + (1-f_R)[|u_1|^2 + 2|u_2|^2]u_1 = -(1-f_R)u_1^2 u_2^*$$
$$- f_R u_1 \int_0^\infty (|u_1|^2 + |u_2|^2) h_R(\tau')d\tau' - f_R u_2 \int_0^\infty (u_1 u_2^* + u_1^* u_2) h_R(\tau')d\tau'. \quad (5.6)$$

The three terms on the right side respectively correspond to interpulse FWM, RIFS, and interpulse Raman scattering. There are also two nonlinear terms on the left side of eq. (5.6). Some of these five terms cause nonlinear phase shifts while the others initiate an energy transfer. To isolate the energy transfer terms, we look at the evolution of the pulse intensity $|u_1|^2$ and obtain

$$\frac{\partial |u_1|^2}{\partial \xi} = -2\mathrm{Im}\left[(1-f_R)u_2^2 u_1^{*2}\right] - 2\mathrm{Im}\left[f_R u_1^* u_2 \int_o^\infty (u_1 u_2^* + u_2 u_1^*) h_R(\tau')d\tau'\right]. \quad (5.7)$$

The first term on the right side is due to the Kerr effect and represents energy transfer initiated by interpulse FWM. The second term is due to the Raman effect and represents energy transfer initiated by interpulse Raman scattering. The evolution equation for $|u_2|^2$ can be found by interchanging $u_1$ and $u_2$ in eq. (5.7).

Equation (5.7) is quite useful for understanding the results shown in Figs. 5.1–5.3. The right side of eq. (5.7) is 0 initially since both $u_1$ and $u_2$ are real at $\xi = 0$ for two in-phase solitons. For the energy transfer to occur, there has to be a relative phase difference between the two pulses. In the case of two in-phase pulses launched at the same frequency, a change in the relative phase can be initiated by cross-phase modulation, Raman scattering, or both.

Once a finite relative phase is established between the two pulses, the interpulse Raman term in eq. (5.7) leads to an asymmetric transfer of energy between the two pulses. The asymmetry arises from the Raman response function $h_R(t)$, which has a long oscillatory tail and produces a net transfer of energy from the leading pulse to the trailing pulse as the two pulses propagate along the fiber. This energy transfer produces changes in the soliton widths, which in turn leads to different RIFS for each soliton. As a result, the solitons begin to move away from each other. So, while interpulse FWM and the Raman effect both can cause energy transfer between the solitons, it is the asymmetry of the Raman process that eventually leads to increasing separation of the two pulses. It is important to note that the RIFS term from eq. (5.6) does not show up in the equation for energy transfer [eq. (5.7)]. The right-hand side of eq. (10) would remain 0 if there were no temporal overlap between the pulses. Thus, temporal overlap between the pulses is a necessity for energy transfer to occur, which explains the absence of any energy transfer in Fig. 5.3. On the other hand, the RIFS term from eq. (5.6) would still survive, despite a lack of temporal overlap between the pulses, owing to the long tail of the delayed Raman response function ($h_R(t)$). This term affects soliton dynamics for pulses that are widely separated in time.

If we consider the spectral domain, the Raman gain is known to be zero for zero frequency shift. So when there is interpulse energy transfer because of the Raman effect, one would expect energy to flow from the blue edge of the leading soliton to the red edge of the trailing soliton. We have verified this numerically by plotting the output spectrum of each pulse for the case shown in Fig. 5.1. The spectrum of each pulse was asymmetric such that the blue and red sides were steeper for the leading and trailing pulses, respectively. Such spectrally asymmetric energy transfer can result in an additional cross-frequency shift for the two solitons [100].

## 5.3 Impact of relative phase and amplitude

### 5.3.1 Relative phase difference

The results discussed so far consider two in-phase fundamental solitons. As we saw in chapter 4, even in the absence of the Raman effect, an initial phase difference between the two solitons leads to out-of-phase collisions that can lead to a difference in interaction behavior. The inclusion of the Raman effect can cause the relative phase to change in such a way that the interaction force on average is canceled out [96]. In this section, we investigate numerically how the interaction of solitons, in the presence of Raman scattering, is affected by their initial relative phases.

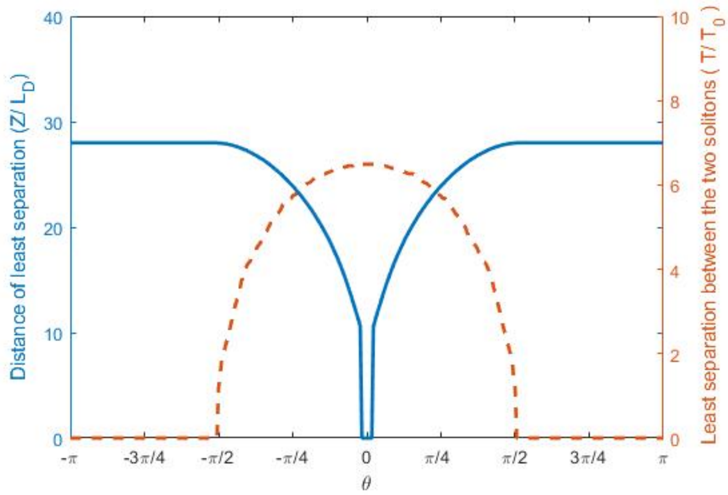


*Fig. 5.4:* Distance at which two pulses have smallest separation (solid) and the value of this separation (dashed) as a function of the relative phase $\theta$. The other parameters are $q_0 = 3.5$ and $r = 1$. Raman effect is not included here ($f_R = 0$).

To put the dependence of interaction on the initial relative phase into context, we briefly review the phase dependence of Kerr-induced interactions. As soon as a finite non-zero value of $\theta$ is introduced, the symmetry and periodicity seen in the top row of Fig. 5.1 is broken. For values of $\theta$ between 0 and $\pi/2$, the two pulses undergo an initial phase of attraction before they move away from each other. In the range $\theta = \pi/2$ to $\pi$, the pulses experience monotonic repulsion and begin to move away from each other right away. We can quantify this behavior by plotting the distance at which the pulses come closest to each other as a function of $\theta$. This is shown in Fig. 5.4 where we also show the smallest separation of pulses. When $\theta$ is between $\pi/2$ and $\pi$ (or between $-\pi$ and $-\pi/2$), the smallest separation occurs at $z = 0$.

Figure 5.5 shows the same two quantities as in Fig. 5.4, but with the Raman term included. A direct comparison of the two figures reveals the drastic changes induced by the Raman effect, the most noteworthy being that the behavior is not symmetric about $\theta = 0$. We still have a region of no attraction where pulses undergo monotonic repulsion, but this region does not begin exactly at $|\theta| = \pi/2$. In the region $\theta < |\pi/2|$, the pulses undergo an initial phase of attraction, before beginning to move away from each other. However, the minimum pulse separation and the distance at which that occurs do not follow any uniform pattern and even exhibit maxima and minima at specific values of $\theta$.

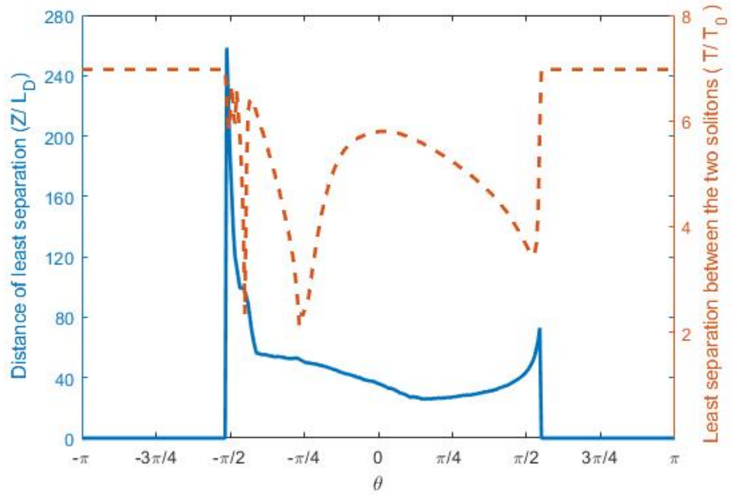


*Fig. 5.5:* Same as fig. 5.4, except that the Raman effect is included here.

In our opinion, this behavior is related to temporal oscillations in the Raman response function $h_R(t)$. Figure 5.6 shows examples of the temporal evolution of the two pulses for two specific values of $\theta = \pi/4$ and $\theta = 3\pi/4$. Notice the different widths of two solitons in the first case after a distance of 40 $L_D$ because of the transfer of energy from the leading soliton to the trailing one. Energy transfer is less significant in the second case where the two solitons begin to separate from each other right away.

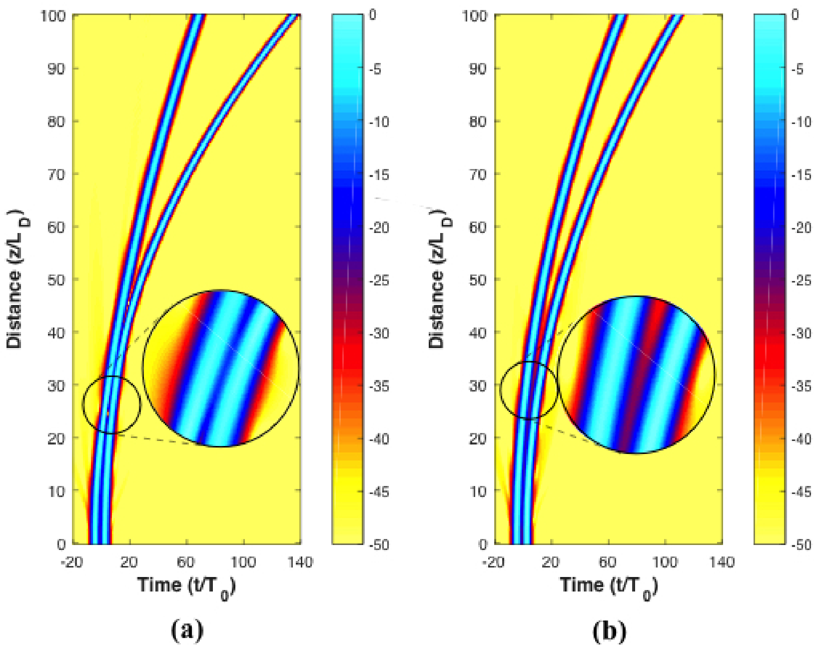


*Fig. 5.6:* Temporal evolution over 100 $L_D$ of two solitons with an initial relative phase of (a) $\theta = \pi/4$ and (b) $\theta = 3\pi/4$. In both cases $q_0 = 3.5$ and $r = 1$. The color bar shows power on a dB scale.

We can use eq. (5.6) to gain some physical insight into the numerical results shown in Figs. 5.4–5.6. If we assume that pulses are so wide that the dispersion terms can be neglected (the continuous-wave approximation) and use $u_j = \sqrt{P_j}e^{i\phi_j}$ where $P_j$ is related to the peak power ($j = 1, 2$), we obtain the following set of three coupled equations for $P_1$, $P_2$, and $\theta = \phi_2 - \phi_1$:

$$\frac{\partial P_1}{\partial \xi} = -2c_f P_1 P_2 \sin(2\theta) - 2f_R P_1 P_2 \sin(2\theta) \tag{5.8a}$$

$$\frac{\partial P_2}{\partial \xi} = 2c_f P_1 P_2 \sin(2\theta) + 2f_R P_1 P_2 \sin(2\theta) \tag{5.8b}$$

$$\frac{\partial \theta}{\partial \xi} = (P_2 - P_1)\left[c_s - c_x - c_f \cos(2\theta) - 2f_R \cos(\theta)\right] \tag{5.8c}$$

where $c_s = 1 - f_R$, $c_x = 2(1 - f_R)$, and $c_f = 1 - f_R$ represent the relative contributions of self-phase modulation, cross-phase modulation, and FWM terms respectively. These equations show how the peak powers and the relative phase evolve with $\xi$. If these quantities stop changing in the limit $\xi \to \infty$, a kind of steady state can be realized. It is easy to see that this can occur only if $P_1 = P_2 = P_0$ and $\theta = \theta_m = m\pi/2$ at $\xi = 0$, where $m$ is an integer. The case of two equal-amplitude, in-phase solitons discussed in section 5.2 corresponds to the choice $m = 0$.

We perform a standard linear stability analysis (LSA) to check the stability of the steady-state solutions. Assuming that small perturbations in phase grow with $\xi$ as $e^{g\xi}$, the growth rate is found to be

$$g = 2P_0\Big[(2 - f_R)(-1)^m(c_s - c_x - 2f_R \cos\theta_m) - c_f\Big]^{1/2} \tag{5.9}$$

It turns out that for phase values that are multiples of $\pi$ ($m$ is an even integer), $g$ is purely imaginary. In other words, the relative phase between the two pulses remains constant on propagation, if the initial value of $\theta$ is chosen to be $-\pi$, 0, or $\pi$. For other values of $\theta$, the relative phase oscillates about the closest multiple of $\pi$. The case of $\theta = \pm\pi/2$ is a special case, since $g$ is 0 at that point. So, if the initial value of $\theta$ is chosen to be $\pi/2$, it will stay the same during propagation of pulses along the fiber. However, even a slight perturbation would lead to $\theta$ oscillating about the next closest multiple of $\pi$. This is the reason that we observe a sudden change in behavior near $\theta = \pm\pi/2$ in Figs. 5.4 and 5.5. The term containing $f_R$ in eq. (12) is responsible for qualitative differences that appear when the Raman term is included.

We also look at how the interpulse energy transfer discussed in section 5.2 for $\theta = 0$ changes for nonzero values of $\theta$. Figure 5.7 shows the fraction of energy transferred to the trailing pulse as a function of $\theta$. An interesting feature seen here is that even when the Raman term is not included, we observe some energy transfer between the pulses, but which pulse transfers the energy depends on whether $\theta$ is positive or negative. This Kerr-induced energy transfer has not been noticed in earlier studies. The energy transfer indicates that two closely spaced solitons with a nonzero value of $\theta$ do not represent an exact two-soliton solution of the NLS equation. Indeed, the well-known two-soliton solution cannot be reduced to the form of our initial conditions at any distance over one period. The physical reason of energy transfer is related to interpulse FWM. Equation (5.7) in the limit of $f_R \to 0$ (no Raman) shows that the term on the right side is not zero when the two solitons have a relative phase difference. It takes a positive value for one soliton, and a negative value for the other, indicating a net energy transfer. We observed this Kerr-mediated energy transfer in the case of intermodal soliton interaction as well, that was discussed in detail in chapter 4.

The inclusion of the Raman term adds asymmetry to the energy transfer mechanism in the sense that the trailing pulse ends up getting more energy for almost any value of

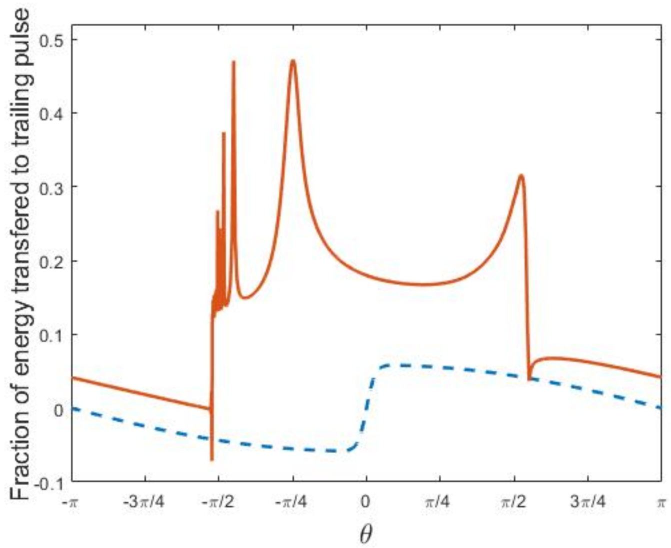


*Fig. 5.7:* Fraction of energy transferred to the trailing pulse as a function of relative phase $\theta$. The solid curve is for the case when the Raman term is included. The other parameters are $q_0 = 3.5$ and $r = 1$. A positive value indicates that the trailing pulse gains energy.

$\theta$ that we choose. The amount of energy transferred is also much larger compared to the Kerr case. The oscillatory nature of energy transfer is again related to the form of the Raman response function for silica glass.

### 5.3.2 Relative amplitude difference

Here, we consider the case of two in-phase solitons with different amplitudes by choosing $\theta = 0$ and $r \neq 1$ in eq. (5.1). If the Raman term is not included ($f_R = 0$), it is known that solitons become resistant to both attractive and repulsive forces when $r \neq 1$. This was discussed in chapter 4. In other words, spacing between the two solitons oscillates as they propagate along the fiber such that they maintain the initial temporal separation between them on average.

The inclusion of the Raman term once again introduces asymmetry to this scenario in the sense that dramatically different behavior occurs depending on whether $r > 1$ or $< 1$. Figure 5.8 shows the two cases by choosing $r = 0.9$ and $r = 1.1$ along with the spectrograms at a distance of 60 $\mathrm{L_D}$ (bottom row). A relative difference in the peak powers of two solitons causes them to have different widths, which causes them to red-shift through RIFS by different amounts, and thus travel at different speeds along the fiber. If the trailing pulse has a higher peak power ($r > 1$), it experiences a stronger red shift, and the temporal separation increases monotonically between the two pulses. In contrast, if the leading pulse has a higher peak power ($r < 1$), it catches up with the trailing pulse after propagating a certain distance. At this point the pulses appear to cross each other before separating. Closer inspection reveals that, in fact, the two pulses never completely overlap, indicating an out-of-phase collision. As soon as the leading pulse approaches the trailing pulse, they begin to exchange energy through interpulse Raman scattering. As a result, the trailing pulse becomes more energetic and begins to move away from the other one.

The temporal fringes seen in Fig. 5.8 correspond to the dispersive waves created when

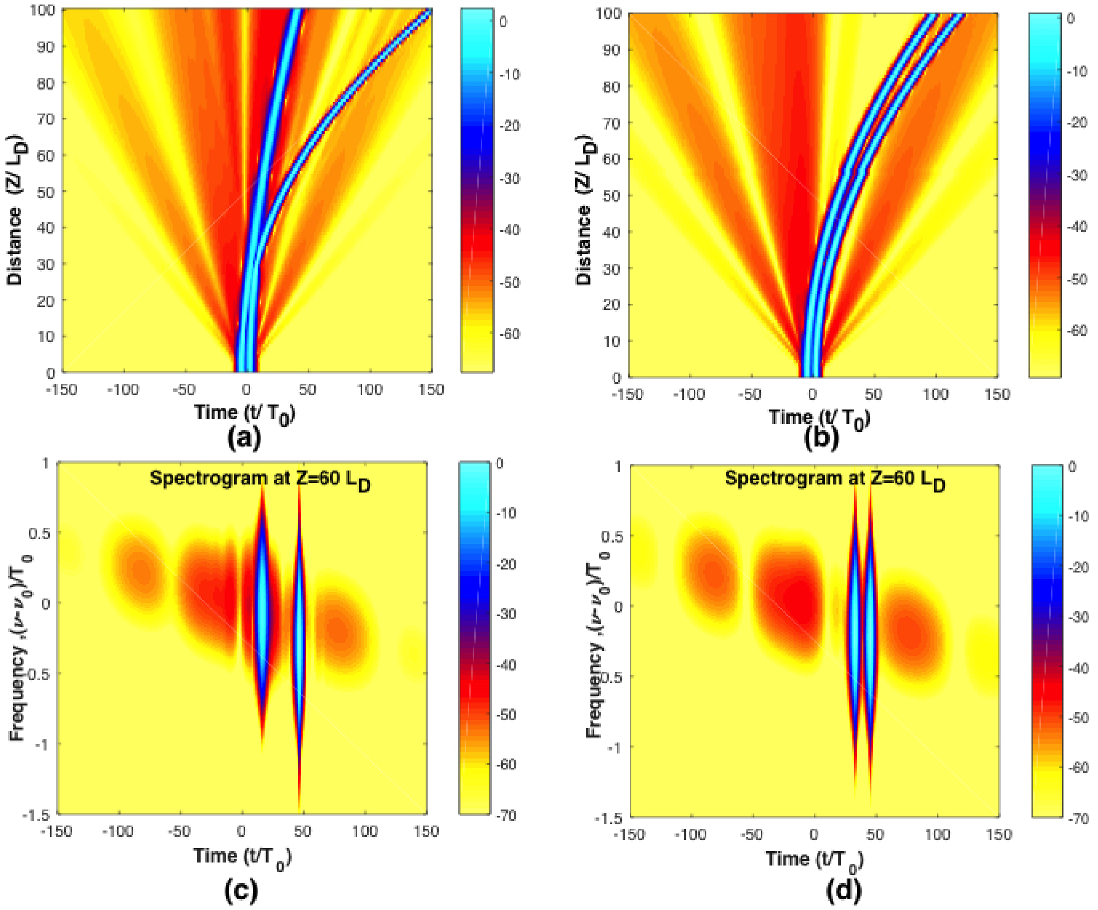


*Fig. 5.8:* (*Top row*) Temporal evolution over 100 $\mathrm{L_D}$ of two in-phase solitons with different amplitudes (*left*) $r = 0.9$ and (*right*) $r = 1.1$. In both cases, $q_0 = 3.5$ and $\theta = 0$. (*Bottom row*) Spectrograms at a distance of 60 $\mathrm{L_D}$ for the two cases in the top row that show different red shifts for individual solitons. Temporal fringes are caused by a small frequency difference between the two dispersive waves shed by a soliton.

solitons shed some energy as they are perturbed by the Raman effect. This dispersive radiation appears to form a fringe pattern whose origin can be understood as follows. As each pulse is perturbed by the other pulse, it sheds some energy in the form of a dispersive wave. But since the pulses have red-shifted by different amounts (owing to different initial peak powers), the excess energy shed from each pulse is at slightly different frequencies, leading to interference between the radiation emitted by each pulse and creating a fringe pattern seen in Fig. 5.8. This behavior has been observed in an experiment where soliton collisions were found to create dispersive waves [105].

## 5.4 Impact of Raman scattering on intermodal soliton interaction

Finally, we study interaction between solitons propagating in distinct, degenerate modes of a multimode fiber. This case has been studied in detail in chapter 4, but without including the effect of Raman scattering. The numerical simulations are performed using the same fiber parameters used to generate Fig. 4.2, but the input pulse is now shortened to $T_0 = 100$ fs, to ensure significant contribution from Raman scattering. We then solve eq. (2.17) with $f_R = 0.245$ and normalize the parameters $A(z,t)$, $z$ and $t$ to $u(\xi,\tau)$, $\xi$ and $\tau$ respectively, as described in chapter 2.

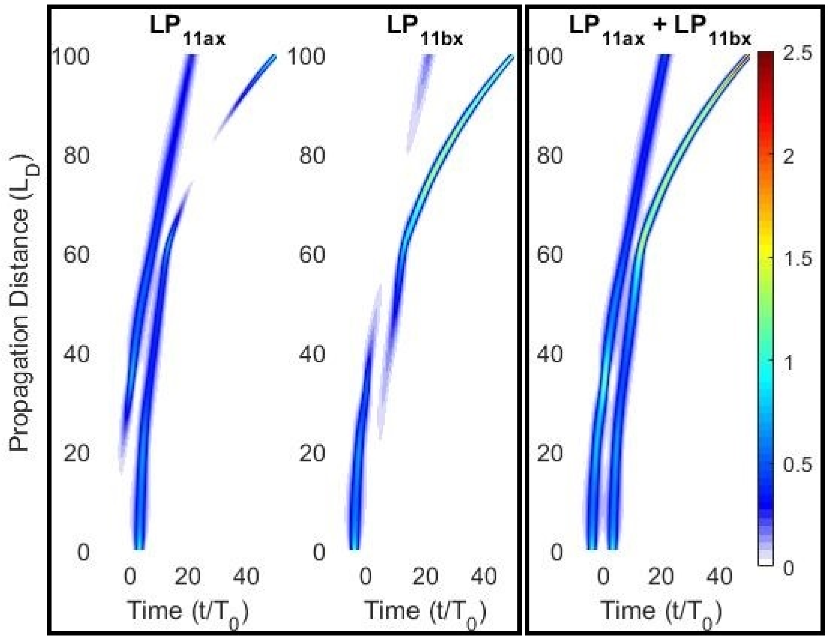


*Fig. 5.9:* Interaction of two temporally separated solitons launched in degenerate modes with Raman term included ($f_R = 0.245$). (*Left*) Evolution of power in individual modes (*Right*) Sum of power in both modes. The color bar shows optical power on a linear scale.

Figure 5.9 shows two-soliton intermodal interaction with Raman scattering included. We observe behavior that is quite different from the Kerr-mediated two-soliton intermodal interaction seen in chapter 4. Just as we saw in Fig 4.2, initially the two pulses appear to undergo a phase of attraction. Simultaneously, intermodal FWM also transfers some power between the modes. But as the pulses propagate along the fiber, the Raman effect starts to dominate and we begin to see a net transfer of power from the leading to the trailing pulse. The occurrence of this phenomenon was explained in detail in section 5.2.

Just as we had found that the evolution of total power in the two modes (Fig. 4.2) appeared to be qualitatively similar to the SMF case (Fig. 4.1), the same conclusion can be drawn when Raman scattering is included (compare qualitative behavior of bottom panel of Fig. 5.1 with the right-most panel in Fig. 5.9). But a mode-resolved picture shows us that most of the power is eventually transfered to the trailing pulse, which after the first out-of-phase collision, happens to be in the $\mathrm{LP}_{11b}$ mode for the case shown in Fig. 5.9. So while equal energy solitons were launched simultaneously in each fiber mode, we end up with most of the input energy in one mode after propagating 70 $\mathrm{L_D}$, owing to the asymmetry introduced by Raman scattering. The mode in which most of the energy eventually is confined depends on the input conditions.

## Conclusions

In this chapter, we have studied in considerable detail the effect of Raman scattering on the nonlinear interaction of two temporally separated pulses with identical spectra that propagate inside a single-mode fiber as fundamental solitons. We distinguish carefully between the intrapulse and interpulse Raman effects. The former produces spectral red shifts of each pulse, while the latter can lead to energy transfer between the two pulses in addition to spectral red shifts.

We first considered the special case of two identical in-phase solitons. The interplay between the Kerr effect and the delayed Raman response changes considerably the known behavior caused by the Kerr nonlinearity. Our results show that, even though the two solitons still experience some attraction initially, they undergo an out-of phase collision before beginning to separate from each other because of the Raman-induced spectral red shifts that change the relative speed of two pulses inside the dispersive nonlinear medium. Moreover, the delayed nature of the Raman response leads to considerable transfer of energy from the leading pulse to the trailing pulse through the interpulse Raman interaction between the two solitons. As a result of this energy transfer, the trailing soliton becomes narrower compared to the leading one and its spectrum is red shifted further because of intrapulse Raman scattering. The net result is that the two solitons that were identical in all respects initially develop different spectra, widths, and peak powers as they propagate inside an optical fiber.

We also investigated how different amplitudes or phases of the two solitons affect the interaction scenario in the presence of the Raman effect. In the case of different input phases, the soliton interaction depends considerably on the precise value of the initial phase difference between the two input pulses. We studied the minimum spacing between the solitons and the distance at which that occurs as a function of the relative phase shift and compared the interaction behavior with and without including the Raman effects. The fraction of energy transferred from the leading pulse to the trailing pulse also depends considerably on the precise value of the relative phase shift and this fraction can exceed 40% for some specific values of this parameter. A new feature that remained unnoticed in the past studies is that energy transfer between the two solitons can occur even when solitons interact only through the Kerr nonlinearity, if their relative phase is finite initially. However, the fraction of energy transferred is typically below 10%. Moreover, the net energy transfer is from the trailing pulse to the leading pulse for negative values of this relative phase, a situation that never occurs when the Raman effects are included.

In the case of different-amplitude solitons, we found considerably different behavior depending on whether the leading pulse or the trailing pulse has a higher amplitude initially owing to the asymmetry caused by the Raman effect. When optical pulses propagate as solitons, the soliton with a higher amplitude is also narrower. As a result, its red-shift through intrapulse Raman scattering is enhanced and it moves slower compared to the soliton with a smaller amplitude. The extent of energy transfer also depends on whether the leading soliton has a higher or smaller amplitude compared to the trailing one.

It should be evident from our results that both the intrapulse and interpulse Raman effects play a critical role in the nonlinear interaction of two temporally separated solitons. For pulses shorter than a few picoseconds, these effects cannot be ignored and should be considered in any study where two or more temporally separated short optical pulses are transmitted through a nonlinear dispersive medium.

Finally, we briefly overview the impact that Raman scattering can have on intermodal soliton interaction, by comparing it to the results from chapter 4. What we find is that Raman interaction eventually leads to a net transfer of energy from the leading to the trailing pulse, and most of this energy ends up in one of the modes. In fact, similar to what was observed in chapter 4, the evolution of total energy in the fiber shows similar qualitative behavior to the SMF case.

# Chapter 6

# Spectral compression and broadening in MMFs

In chapters 2–5, we studied in detail several soliton effects inside an optical fiber. In this chapter, we focus on how the spectrum of an optical pulse is modified when that pulse is launched into a few-mode fiber. The interplay between nonlinearity and dispersion has been used to realize several interesting spectral effects like creation of new frequencies and parametric amplification through four-wave mixing (FWM) [1], supercontinuum generation (SCG) [106] and frequency comb [107] sources etc. Several of these sources have played a major role in the advancement of fields like optical communications, spectroscopy and biomedical optics.

The spectral evolution of an optical pulse in a fiber changes considerably depending on whether the pulse is launched in the normal or anomalous dispersion regime. To generate supercontinuum, optimal spectral broadening is usually realized by using a short, high energy pump pulse in the anomalous dispersion region of a photonic crystal fiber (PCF). Pumping in the normal dispersion region has also been proposed to generate a supercontinuum with higher coherence [108–112]. In the last decade, there have been reports on SCG in multimode fibers as well [22, 113, 114]. While intermodal nonlinear coupling in MMFs increases the complexity of the system, it also provides novel nonlinear pathways for generation of new frequencies. One such effect that has recently been investigated in graded-index MMFs is the creation of discreetly spaced sidebands due to geometric parametric instability [42, 115]. The underlying motivation in most of these studies is to optimize the fiber and pump parameters to facilitate multiple nonlinear effects whose cumulative effect would lead to generation of a broad or selective spectral output.

In the study of nonlinear fiber optics, several nonlinear effects are commonly associated with the creation of new spectral components. But there exist certain applications where spectral compression is desired. There have been studies showing nonlinear spectral compression in optical fibers, notably using the effect of self-phase modulation (SPM) on negatively chirped pulses [116, 117]. Recently, Turitsyn *et al* demonstrated a unique nonlinear mechanism in normal disperion fibers, which they call inverse four-wave mixing, that leads to creation of frequency components near the central part of the spectrum at the expense of the frequency components in the wings of the spectrum [118]. Such a self-action effect in a single-mode fiber (SMF) usually requires precise input and phase-matching conditions. In a MMF, intermodal four-wave mixing (FWM) can provide many more pathways for phase-matching. Selectively exciting spectral components in one mode can lead to creation or suppression of select spectral components in another mode. Understanding this mechanism may be useful for observing new effects by suitably designing a fiber's dispersion profile and it's nonlinearity.

In this chapter, we numerically analyze spectral compression occurring in the normal dispersion region of a few-mode fiber. While this effect does not lead to the suppression of the SPM induced broadening, it does lead to spectral cleanup of the wings due to intermodal FWM. We discuss this phenomenon in section 6.1. In section 6.2, we present the experimental results of spectral broadening that occurs when a short, intense pulse is launched in the anomalous dispersion region of a few-mode PCF. Finally, the effects studied in this chapter are summarized.

## 6.1 Suppression of spectral broadening in normal dispersion few-mode fibers

To understand the intermodal nonlinear mechanisms involved in a multimode fiber, we consider a fiber that supports just the first two spatial modes in the weakly-guiding approximation. To numerically simulate such a fiber, we use the simple case of a standard telecom fiber (Corning SMF-28) and assume the pump to be a secant-hyperbolic pulse with $T_0 = 100$ fs (full-width at half maxima of 176 fs) centered at 1054 nm. A core diameter of 8.2 $\mu m$ and numerical aperture (NA) of 0.14 is used to calculate the fiber parameters. At this wavelength, the fiber has a V-number of 3.4 and can support the first two spatial modes ($\mathrm{LP}_{01}$ and $\mathrm{LP}_{11}$). Similar to the few-mode fiber considered in the previous chapters, if we include the degeneracy of the $\mathrm{LP}_{11}$ mode and account for the two orthogonally polarized components of each mode, we end up with a total of six modes that this fiber can support at this wavelength. However, we will be pumping only in the x-polarized components of the $\mathrm{LP}_{01}$ and the $\mathrm{LP}_{11a}$ modes and hence only two modes are shown in the figures that follow.

We solve eq. (2.20) using the fourth-order Runge-Kutta method in the interaction picture that was explained in section 2.3.2. Despite the higher losses in SMF-28 at an input wavelength of 1054 nm, we can safely ignore it for the short propagation distances that we simulate here. For the sake of simplicity, we still persist with the "soliton-units", despite pumping in the normal dispersion region where solitons are not expected.

Figure 6.1 shows the two normalized dispersion parameters corresponding to the inverse group-velocity ($d_{1p}$) and group-velocity dispersion ($d_{2p}$), for the $p^{th}$ mode. As we can see from the figure, a light pulse at 1054 nm would experience normal dispersion in both the modes supported by the fiber. It is important to note that for frequencies redsfihted by more than 80 THz (which corresponds to wavelengths greater than 1460 nm), the higher-order mode ($\mathrm{LP}_{11}$) is no longer supported by the fiber.

As noted earlier, there are many nonlinear effects which can contribute to spectral broadening of an optical pulse propagating through a nonlinear medium. In the normal dispersion region of a fiber, if we do not include the Raman effect, the major contribution to spectral broadening is due to SPM. In the case of higher pump powers, wave-breaking leads to the creation of additional spectral sidebands. In the study of SCG in normal dispersion fibers, FWM sidebands which are seeded by the SPM broadened wings of the spectrum have also been observed [109], which contribute to further broadening of the spectra.

In Figure 6.2(a), we show the case when a secant-hyperbolic pump pulse centered at 1054 nm with $T_0 = 100$ fs and $N = 8$ is launched into the fundamental ($\mathrm{LP}_{01}$) mode of the fiber. As we can see, after propagating for $0.4\mathrm{L_D}$, which corresponds to 24 cm of fiber, the spectrum has broadened considerably compared to the input pulse. The low-power spectral components beginning to come up beyond 50 THz on both the red and blue sides are the FWM sidebands. We verified that the new spectral components that are created

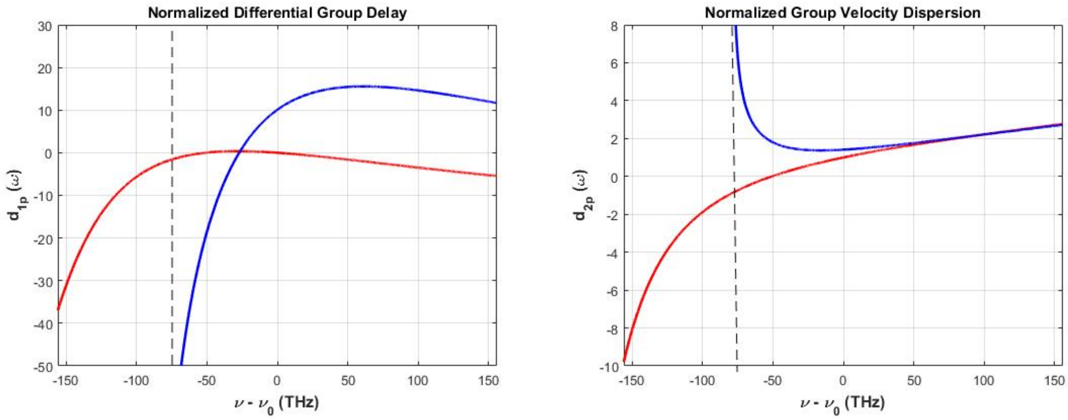


*(a)* *(b)*

*Fig. 6.1:* (a) Normalized differential group delay parameter ($d_{1p}$) and (b) Normalized group velocity dispersion ($d_{2p}$) as a function of frequency. The red curve corresponds to the $\mathrm{LP}_{01}$ mode and the blue curve corresponds to the $LP_{11}$ mode. The dotted line indicates higher-order mode cutoff, which means that the $\mathrm{LP}_{11}$ mode does not exist in the region to the left of the dotted line.

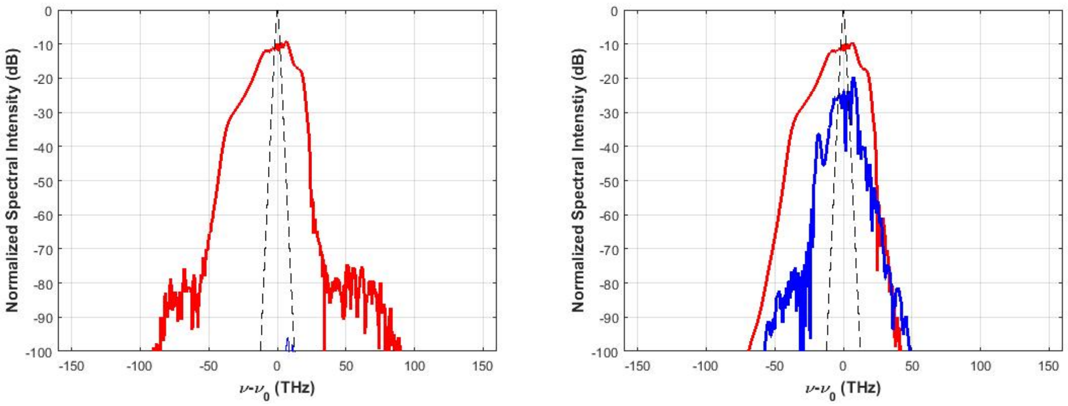


*(a)* *(b)*

*Fig. 6.2:* Spectal intensity after propagating for $0.4\mathrm{L_D}$ along the fiber with the following input conditions (a) Input pulse with N=8 and $\mathrm{T}_0$ = 100 fs launched in the $\mathrm{LP}_{01}$ mode and (b) Same pulse in $\mathrm{LP}_{01}$ and a pulse with the same width but 40% of the peak power in the $\mathrm{LP}_{11}$ mode. The red curve corresponds to the $\mathrm{LP}_{01}$ mode and the blue curve corresponds to the $\mathrm{LP}_{11}$ mode. The dashed curve shows the input pulse launched in the fundamental mode.

are not because of GPI, which requires beating between modes, by simulating single-mode propagation.

But we notice interesting behavior when we start launching some light into the higher-order mode along with the same input pulse in the fundamental mode as in Fig. 6.1(a). In the case that we show here [Fig. 6.2(b)], the input pulse launched in the higher-order mode is also a secant-hyperbolic pulse centered at 1054 nm with $T_0 = 100$ fs, but with a peak-power value that is 40% of what is coupled into the fundamental mode. What we can see clearly from the figure is that the presence of energy in the $\mathrm{LP}_{11}$ mode has suppressed the spectral wings that were observed in Fig. 6.1(a). This effect is further highlighted in Fig. 6.3 which shows the spectrogram of the fundamental mode after propagating a distance of $0.4\mathrm{L_D}$ for the two cases shown in Fig. 6.2.

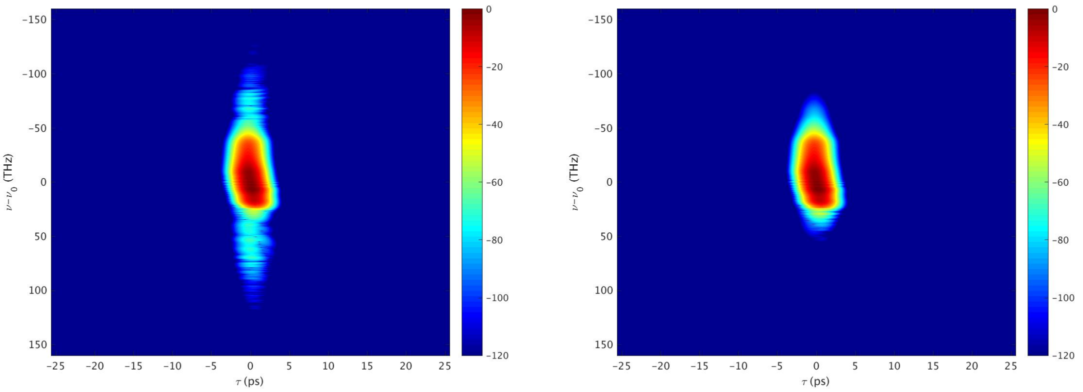


*(a)* *(b)*

*Fig. 6.3:* Spectrograms of the fundamental mode after $0.4\mathrm{L_D}$ with the same initial conditions as in Fig. 6.2(a) and (b) respectively. The colorbar shows intensity on a dB scale.

There are several important points to note here. First, as we noted earlier, the higher-order mode is not supported for frequencies that are more than 80 THz below the central frequency. This means that, in order to observe this effect for the fiber under consideration, we need to work with parameters which do not lead to significant broadening beyond 80 THz on the red side. Second, we observe this effect only in the normal-dispersion region of the fiber. As we can see from Fig. 6.1(b), the fundamental mode has a zero-dispersion wavelength (ZDW) around 1290 nm, which corresponds to a shift of -51 THz from the central frequency. So the component of the fundamental mode that is broadened beyond the ZDW will see anomalous dispersion. This also affects the suppression. We performed an unphysical simulation where we chose a fixed value of dispersion parameters across the entire spectral window to be a constant equal to their value at the central frequency ($d_{1p}(\omega) = d_{1p}(\omega_0)$, $d_{2p}(\omega) = d_{2p}(\omega_0)$). This forces both the modes to have normal dispersion across the entire spectral window. We can clearly observe the side-bands beginning to form and then getting suppressed because of the intermodal processes seeded by the higher-order mode. Another important question that arises pertains to the amount of energy required in the higher-order mode to suppress the spectrum in the fundamental mode. Indeed, we performed many simulations and observed suppression till we reduced the peak power coupled into the higher-order mode to 20 dB below the peak power in the fundamental mode. We discuss the physics behind this phenomena in the following subsection.

### 6.1.1 Discussion

If we expand all the nonlinear coupling terms in eq. (2.20) and write the equations for the $\mathrm{LP_{01}}$ and $\mathrm{LP_{11}}$ modes separately, we get the following equations:

$$\frac{\partial u_1}{\partial \xi} + d_{11}\frac{\partial u_1}{\partial \tau} + i\frac{d_{21}}{2}\frac{\partial^2 u_1}{\partial \tau^2} = iN^2 \times \left[f_{1111}|u_1|^2 u_1 + (f_{2211} + f_{2121})|u_2|^2 u_2 + f_{1221}u_2^2 u_1^*\right], \tag{6.1a}$$

$$\frac{\partial u_2}{\partial \xi} + d_{12}\frac{\partial u_2}{\partial \tau} + i\frac{d_{22}}{2}\frac{\partial^2 u_2}{\partial \tau^2} = iN^2 \times \left[f_{2222}|u_2|^2 u_2 + (f_{1122} + f_{1212})|u_1|^2 u_2 + f_{2112} u_1^2 u_2^*\right] , \tag{6.1b}$$

Since we have neglected the Raman and shock effects, the nonlinear terms on the right-hand side of these equations can be grouped into three main physical effects: SPM, cross-phase modulation (XPM) and intermodal FWM. To understand the origin of this spectral suppression phenomenon, we simulate artificial cases where the terms corresponding to either the XPM, IM-FWM or both have been turned off. We do that by setting the corresponding coupling coefficients to zero. Figure 6.4 shows the three simulated cases. As one would expect, the XPM term leads to further broadening of a weak pulse in the higher-order mode than it would normally broaden in the absence of the strong pulse in the fundamental mode. This effect is apparent when we compare Fig. 6.4(a) with Fig. 6.4(c). But, as this comparison shows, XPM induced nonlinear coupling does not lead to any spectral compression. Instead, when we compare Fig. 6.4(b) with Fig. 6.4(c), it becomes clear that the IM-FWM term is the one responsible for spectral compression. This means that IM-FWM is able to transfer power from the wings of the total spectrum towards the central part.

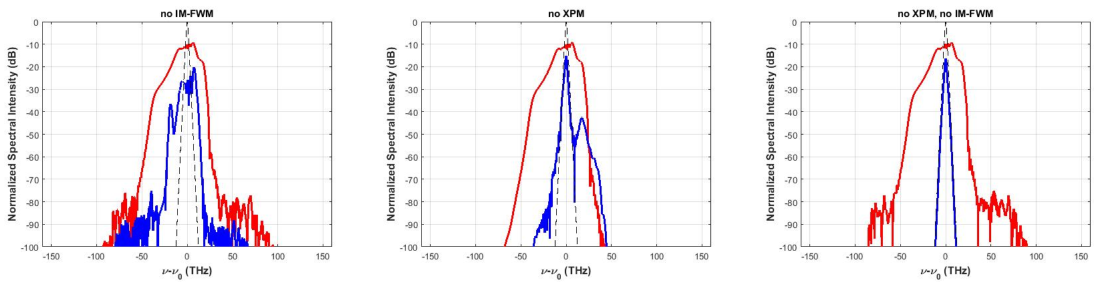


(a) (b) (c)

*Fig. 6.4:* Spectral intensity after propagating for $0.4\mathrm{L_D}$ along the fiber for the same initial conditions as in fig.6.2(b), but with (a) XPM term removed, (b) IM-FWM term removed and (c) both XPM and IM-FWM terms removed from the numerical model. The red and blue curve correspond to the $\mathrm{LP_{01}}$ and $\mathrm{LP_{11}}$ modes respectively and the dotted curve shows the input in the fundamental mode.

When we look at the total spectrum, this effect bears some resemblance to the inverse FWM effect that has been observed in normal dispersion SMFs, which causes spectral narrowing because of the components towards the edge of the spectrum transferring power to the central part of the spectrum [118]. We do not observe that effect for single mode propagation in our case, because of the low power levels and dispersion profile that we use. But the inclusion of another mode opens up new nonlinear pathways that lead to this effect. Figure 6.5 shows a simple example of such a pathway. We use a continuous-wave (cw) input to demonstrate the type of processes that can take place in this bimodal system. In Fig. 6.5(a), two quasi-monochromatic pump beams separated by 80 THz are launched into the fundamental mode of the fiber. They interact with each other to generate Stokes and anti-Stokes bands, but notice that no power is transfered in the spectral region between the two pumps. In Fig. 6.5(b), we simultaneously launch a pump in the higher-order mode which is off-centered by 10 THz on the red side, along with the two pumps from Fig. 6.5(a). As the figure shows, the IM-FWM processes can lead to transfer of power into the spectral region between the two pumps in the fundamental mode, which means that the addition of the pump in another mode can lead to gain in the region between the two pumps in the fundamental mode. One of the possible transition responsible for this: $\omega_{p1}^{01} + \omega_{p2}^{11} = \omega_{s}^{01} + \omega_{i}^{11}$, is shown in Fig. 6.5(b). Here $p1$, $p2$, $s$ and $i$ subscripts correspond to pump1, pump2, signal and idler respectively. It should be noted that this is just a qualitative argument and does not account for many other nonlinear effects that would simultaneously occur in the case of a pulsed input. The generated signal peaks can be further amplified compared to the idlers by the presence of energy in the central region in the pulsed case. Also, the assumption of temporal overlap that is implied in the cw case would not always hold true as different spectral components of a pulsed input might not overlap in time and thereby not interact.

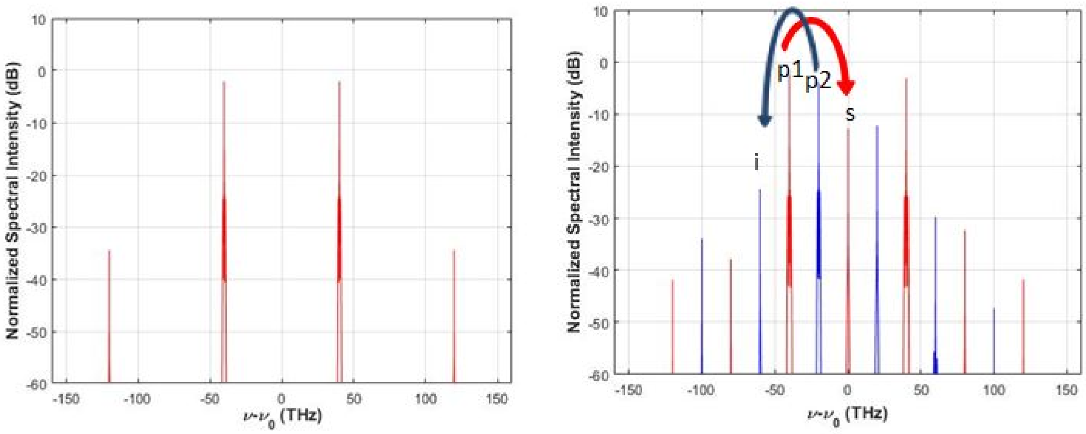


(a) (b)

*Fig. 6.5:* Two quasi-monochromatic CW pumps separated by 80 THz launched in the fundamental mode of the fiber with (a) No input in the higher-order mode and (b) a quasi-monochromatic CW pump at -10 THz simultaneously launched in the higher-order mode. The arrows shows one of the IM-FWM transitions that can lead to transfer of power towards the central part of the spectrum in the fundamental mode. The red and blue curve correspond to the $LP_{01}$ and $LP_{11}$ modes respectively.

## 6.2 Experimental results of nonlinear spectral broadening

As we saw in the introduction to this chapter, extreme spectral broadening, commonly referred to as supercontinuum generation (SCG), is usually achieved by pumping a highly nonlinear fiber in the anomalous dispersion regime. Here, we will take a look at some preliminary experimental results of spectral broadening.

The fiber that we use is a photonic crystal fiber (PCF) (NL-1050-ZERO-2 from NKT Photonics) with a nonlinear coefficient $\gamma$ of $\sim$37 (W-km)$^{-1}$ at a wavelength of 1064 nm. This fiber has a core diameter of 2.3 $\pm$ 0.3 $\mu$m and a numerical aperture of $\sim$0.37. The dispersion profile and attenuation for this fiber are shown below in Fig. 6.6. As we can see, the fiber has two zero-dispersion wavelengths that are located around 1025 nm and 1075 nm. We use 7.3 m of this fiber, although it should be noted that spectral broadening is expected to occur within a very short distance of pulse propagation.

We launch input pulses in this fiber using a mode-locked ytterbium laser that is pumped at 980 nm. This laser emits 150 fs wide pulses with average power of 100 mW and repetition rate of 38 MHz. The wavelength is centered at 1054 nm. At this wavelength,

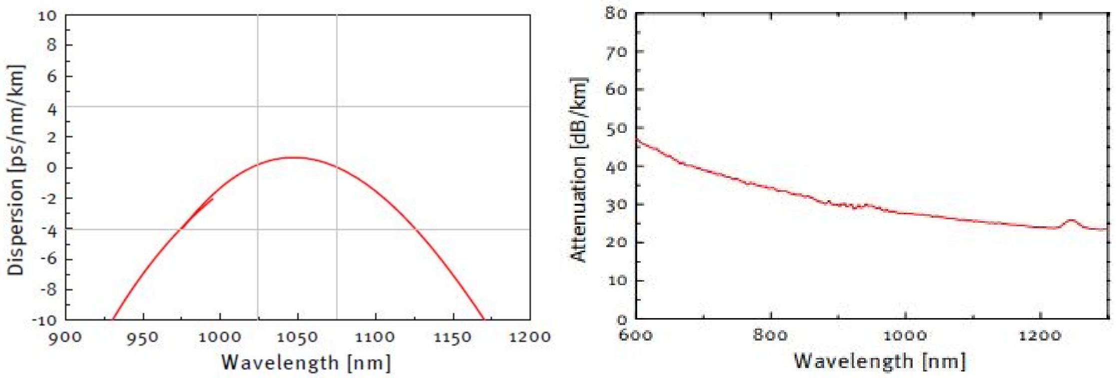


*(a)* *(b)*

*Fig. 6.6:* (a) Dispersion and (b) attenuation profile for the photonic crystal fiber used in the experiment. The plots are taken from the catalog from NKT Photonics (NL-1050-ZERO-2).

the fiber has a normalized frequency parameter of V = 2.53, so it supports the first two mode-groups ($LP_{01}$ and $LP_{11}$). Hence, intermodal nonlinear effects can also aid in the process of spectral broadening. As we can see from Fig. 6.6, the input wavelength lies in the anomalous dispersion region between the two zero-dispersion wavelengths.

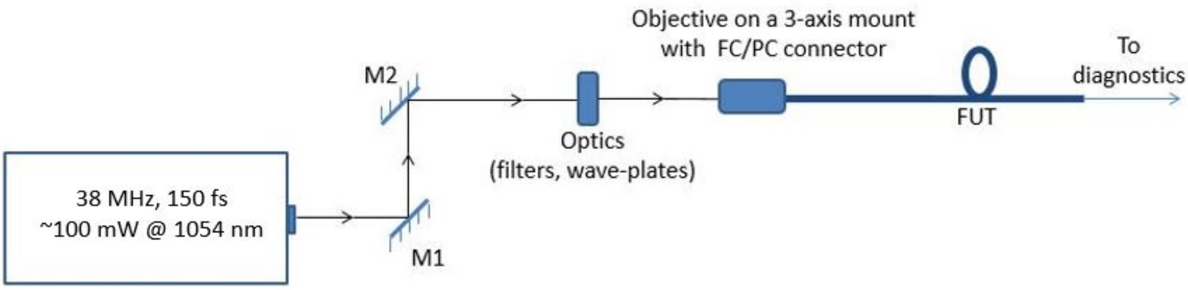


*Fig. 6.7:* Schematic of the experimental setup for studying spectral broadening in a photonic crystal fiber. Pulses generated from the mode-locked laser are coupled into the fiber under test (FUT) using the two mirrors $M_1$ and $M_2$ and a microscope objective.

A schematic of the experimental setup is shown in Fig. 6.7. As seen in the figure, we use two mirrors (M1 and M2) to send the input pulse on to a microscope objective. This objective is mounted on a 3-axis stage and used to couple the laser beam in to the PCF. The objective used here has a numerical aperture of 0.3. We can qualitatively vary how much light couples into which mode by controlling the angle of launch using mirrors M1 and M2. We can measure the power, spectrum and spatial profile of the light that comes out of this fiber using a power meter, optical spectrum analyzer (Yokogawa AQ6370D) and a laser beam profiler (Newport LBP2-HR-VIS) respectively.

Figure 6.8 shows the spectral and spatial output for three different instances of coupling light into the fiber. While this data needs to be further analyzed, there are several interesting things that we can immediately notice. We are able to get a broad, flat-top supercontinuum owing to the interplay of nonlinearity and dispersion. As one would expect, we observe more spectral broadening as the amount of power coupled into the fiber increases. However, it is interesting to note that there is no marked difference in spectral broadening behavior even when the spectrum crosses over into the normal dispersion region ($<$1025 nm and $>$1075 nm). We notice more energy on the red side of the input

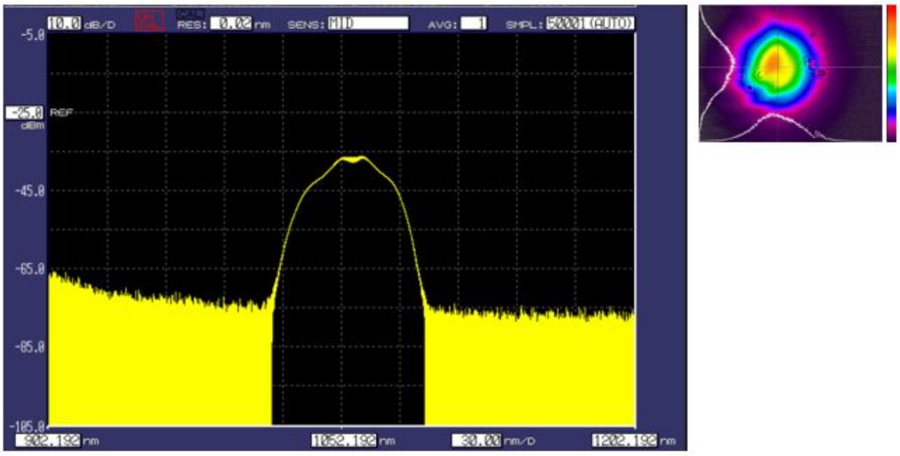


(a)

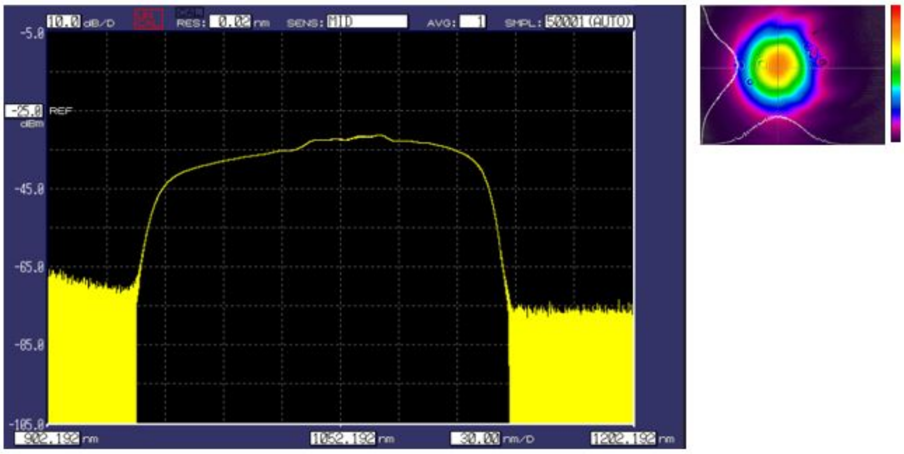


(b)

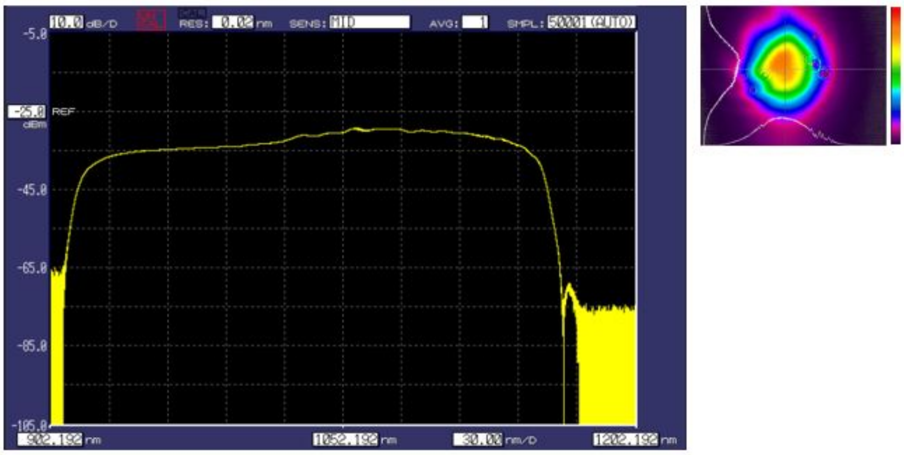


(c)

*Fig. 6.8:* Spectral and spatial output (top right) for different conditions of coupling into a photonic crystal fiber that supports the first two spatial mode groups. The average power at the fiber output for each case is (a) 0.43 mW (b) 4.16 mW (c) 10.16 mW. The fiber used here is 7.3 m long. The input is a laser pulse centered at 1054 nm and 150 fs long with an average power of 100 mW and repetition rate of 38 MHz.

wavelength (1054 nm), potentially owing to Raman effect.

Figure 6.8 also shows the spatial profile at the output of the fiber. As we can see from the figure, the output spatial profile is not always gaussian-like, and this asymmetry confirms that energy can be present in both modes that are supported by the fiber. Hence, intermodal nonlinearity can play a role in spectral broadening. Here, we do not have precise control over which mode of the fiber we are coupling light into, since that would require manipulating the phase of the input pulse using a spatial light modulator (SLM) or a phase plate. But varying the angle at which the laser is launched into the fiber, we can observe that we are indeed changing how much power gets coupled into each mode. It should be mentioned here that the spatial content at the output is likely to be different from that at the input, since nonlinearity can lead to power transfer between the modes. Finally, as we increase the power that gets coupled into the fiber, we start to notice a weak pulse-like artifact near the red-edge of the supercontinuum. We have observed that this spectral pulse red-shifts and becomes more energetic as the power coupled into the fiber is increased. This is an interesting phenomenon and requires further investigation.

## Conclusion

In this chapter, we looked at some interesting spectral effects that occur due to nonlinearity in few-mode optical fibers. We first studied a phenomenon that led to suppression of spectral broadening, an effect similar to inverse FWM [118], in normal dispersion few-mode fibers. We found that the presence of energy in a higher-order mode could lead to suppression of spectral broadening in the fundamental mode. Further simulations revealed that this effect was due to intermodal FWM.

We also looked at some experimental results of supercontinuum generation in a PCF that supports the first two mode-groups. Using a 150 fs, 100 mW average power pulse and varying its coupling efficiency and angle of launch into a PCF, we were able to observe a flat-top supercontinuum. Additionally, we also noticed other artifacts like more energy on the red side of the spectrum and a weak pulse-like spectral artifact on the red edge of the spectrum. The experimental data appears to show rich intermodal and intramodal nonlinear behavior and requires careful consideration in the future.

# Chapter 7

# Nonlinear propagation equations with random linear mode coupling

The modes of an ideal fiber can be coupled through nonlinear effects, as we have seen in the previous chapters, but they do not exhibit any linear coupling. However, in practice, there always exists some linear coupling between different spatial modes of the fiber. Such linear coupling is random and generally distributed over the entire length of the fiber. Random linear coupling can occur owing to material issues and waveguide imperfections. This poses a major challenge in understanding light propagation in a space-division multiplexing (SDM) system. From a system point-of-view, random mode coupling may require complex equalization at the receiver. However, it has also been shown that, under certain conditions, linear mode coupling may actually reduce the impact of nonlinear effects and therefore improve system performance [30, 31, 33, 119, 120].

Theoretically, including the impact of random linear mode coupling (RLMC) on pulses propagating inside multimode fibers is not trivial since RLMC can occur due to a variety of sources including microbending, density fluctuations, and random variations in the shape and size of the fiber core. Different models have been proposed to account for specific impairments [121–128]. Modeling nonlinear transmission with the RLMC effects usually is numerically time consuming, since it requires a large number of realizations of stochastic random coupling. In practice, it is important to find averaged equations that can model the effects of RLMC in an efficient manner. Such averaging can reduce computational time by orders of magnitude. The averaged equations are referred to as Manakov equations, after a similar treatment used to average random birefringence fluctuations in single-mode fibers [129, 130].

In the case of MMFs, Manakov equations have been derived in two limiting cases: (i) when all modes in the fiber are strongly coupled and (ii) when only groups of degenerate modes are coupled but there is no inter-group coupling. But certain MMFs can exhibit RLMC levels that fall between these two extreme regimes. Moreover, there is no definite criteria to quantify the regime of RLMC that we are operating in.

In this chapter, we build a theoretical framework that will be used to derive general averaged Manakov equations applicable to all regimes of RLMC. In section 7.1, we derive the coupled nonlinear Schrödinger (NLS) equations including the RLMC term and introduce the concept of a transfer matrix that we will use to characterize the impact of RLMC. In section 7.2, we look at several numerical considerations associated with computing the transfer matrix. Finally, in section 7.3, we derive the general averaged Mankov equations that can be used for all regimes of RLMC.

## 7.1 Model for RLMC

We considered a detailed derivation of the coupled NLS equations in section 2.1. However, that derivation did not include random linear mode coupling (RLMC). Here, we discuss how to include RLMC in the derivation of the coupled NLS.

We start with the nonlinear Helmholtz equations [1]

$$\nabla^2 \tilde{\mathbf{E}} + \epsilon(x, y, z) k_0^2 \tilde{\mathbf{E}} = -\omega^2 \mu_0 \tilde{\mathbf{P}}^{\mathrm{NL}} \tag{7.1}$$

where $\tilde{\mathbf{E}}(x, y, z, \omega)$ is the Fourier transform of the electric field, $\tilde{\mathbf{P}}^{\mathrm{NL}}$ is the third-order nonlinear polarization, $\epsilon(x, y, z)$ is the dielectric constant and $\mu_0$ is the permeability of free-space. We include RLMC through random fluctuations in the refractive index of the material. To account for random refractive index fluctuations, we assume [131]

$$\epsilon(x, y, z) = n^2(x, y) + \Delta\epsilon(x, y, z), \tag{7.2}$$

where $\Delta\epsilon(x, y, z)$ is a random variable in three dimensions. We also assume that $|\Delta\epsilon| \ll n_0^2$ at every spatial point so that index fluctuations can be treated in a perturbative manner.

To solve eq. (7.1), we expand $\tilde{\mathbf{E}}(x, y, z, \omega)$ in terms of the fiber modes supported by a multimode fiber in the absence of index fluctuations, similar to the treatment used in section 2.1. However, we now write it in a vector form. The resulting coupled equations can be written as:

$$\tilde{\mathbf{E}}(x, y, z, \omega) = \mathbf{F}(x, y) \circ \tilde{\mathbf{A}}(z, \omega) \circ e^{\imath \boldsymbol{\beta}(\omega) z} \circ \frac{1}{\mathbf{N}}, \tag{7.3}$$

where $\tilde{\mathbf{E}}$, $\mathbf{F}$, $\tilde{\mathbf{A}}$ and $\boldsymbol{\beta}$ are column vectors of length N=2M for a fiber which supports M spatial modes and $\circ$ denotes a Hadamard (entrywise) product. The N modes are arranged as follows: $\tilde{\mathbf{E}} = [\tilde{E}_1, \tilde{E}_2, \tilde{E}_3, \ldots \tilde{E}_k \ldots \tilde{E}_{N-1}, \tilde{E}_N]^{\mathrm{T}} = [\tilde{E}_{1x}, \tilde{E}_{1y}, \tilde{E}_{2x}, \tilde{E}_{2y} \ldots \tilde{E}_{Mx}, \tilde{E}_{My}]^{\mathrm{T}}$, where T denotes the transpose operation. The other vectors are arranged in a similar order. $\tilde{A}_k(z, \omega)$ is the spectrum of the slowly varying envelope of the $k^{th}$ mode of the fiber, $\beta_k(\omega)$ is the propagation constant of the $k^{th}$ mode and $F_k(x, y)$ is the transverse field distribution of the $k^{th}$ mode, which is obtained by solving the linear Helmholtz equation

$$\nabla^2 F_k(x, y) + [n^2(x, y)\omega^2/c^2 - \beta_k^2] F_k(x, y) = 0. \tag{7.4}$$

The normalization constant $\mathrm{N}_k$ is chosen such that $|A_k(z, t)|^2$ represents optical power in watts. The subscript $k$ can take any value from 1 to N. The normalization and orthogonality relations for $F_k(x, y)$ are given by

$$\iint |F_p(x, y)|^2 dx\, dy = 1, \qquad \iint F_p^*(x, y) F_m(x, y) dx\, dy = \delta_{pm}. \tag{7.5}$$

respectively.

Now, we can follow a standard procedure outlined in section 2.2 to obtain the time-domain nonlinear propagation equation that is satisfied by $A_k(z, t)$. But in this case, owing to intermodal nonlinear coupling and RLMC introduced by $\Delta\epsilon(x, y, z)$, it is useful to represent this entire set of N time-domain coupled nonlinear equations in a matrix form. For this purpose, we use the column vector $\mathbf{A}(z, t)$, which is the inverse Fourier transform of $\tilde{\mathbf{A}}(z, \omega)$, containing the temporal pulse envelope of all modes. We also denote by $\mathbf{B}_0$, $\mathbf{B}_1$, $\mathbf{B}_2$ the N $\times$ N diagonal matrices containing respectively the propagation constant ($\beta_0$), inverse group velocity ($\beta_1$) and dispersion parameter ($\beta_2$) of various modes along their diagonal. The master nonlinear propagation equation, governing the evolution of all modes, can then be written in the form [33, 132]

$$\begin{aligned}\frac{\partial \mathbf{A}}{\partial z} &+ \delta\mathbf{B}_1\frac{\partial \mathbf{A}}{\partial t} + \frac{\imath\mathbf{B}_2}{2}\frac{\partial^2 \mathbf{A}}{\partial t^2} = \imath\delta\mathbf{B}_0\mathbf{A} + \imath\mathbf{Q}(z)\mathbf{A} \\ &+\frac{\imath\gamma}{3}\iint \Big[2(\mathbf{A}^{\mathrm{H}}\mathbf{G}^{(1)}\mathbf{A})\mathbf{G}^{(1)}\mathbf{A} + (\mathbf{A}^{\mathrm{T}}\mathbf{G}^{(2)}\mathbf{A})\mathbf{G}^{(2)*}\mathbf{A}^*\Big]\,dx\,dy, \qquad (7.6)\end{aligned}$$

where $\delta\mathbf{B}_0 = \mathbf{B}_0 - \beta_{0r}$ and $\delta\mathbf{B}_1 = \mathbf{B}_1 - 1/v_{g_r}$ are defined by using propagation constant $\beta_{0r}$ and group velocity $1/v_{gr}$ as reference values (taken to be those of the fundamental mode here). The nonlinear parameter, $\gamma$, is also defined using the effective index $n_{\mathrm{eff}}$ and the effective area $A^{\mathrm{eff}}$ of the fundamental mode. The superscript $^{\mathrm{H}}$ in eq. (7.6) denotes Hermitian conjugate. Separating two distinct polarization states associated with each spatial mode (N = 2M) allows us to include random birefringence of the fiber in eq. (7.6) through the matrices $\delta\mathbf{B}_0$ and $\delta\mathbf{B}_1$.

In eq. (7.6), the effects of random linear mode coupling are included through the coupling matrix $\mathbf{Q}(z)$. The elements of this matrix and the two matrices $\mathbf{G}^{(1)}(x,y)$ and $\mathbf{G}^{(2)}(x,y)$ are given by

$$Q_{ij}(z) = \frac{k_0}{2n_i^{\mathrm{eff}}}\iint \Delta\epsilon(x,y,z)F_i(x,y)F_j^*(x,y)\,dx\,dy, \qquad (7.7)$$

$$G_{ij}^{(1)}(x,y) = F_i^*(x,y)F_j(x,y), \qquad G_{ij}^{(2)}(x,y) = F_i(x,y)F_j(x,y) \qquad (7.8)$$

where $n_i^{\mathrm{eff}}$ is the effective index for the $i^{th}$ mode. Clearly, all three matrices depend on the spatial profiles of various fiber modes.

Equation (7.6) involves stochastic matrices. Determining the solution generally requires solving eq. (7.6) a large number of times with different instantiations of the random matrices involved. To derive the average behavior of eq. (7.6), we use an approach similar to the one used to treat birefringence fluctuations to obtain the deterministic Manakov equations [130]. In practice, for distinct fiber modes, the two terms containing $\delta\mathbf{B}_0$ and $\mathbf{Q}(z)$ in eq. (7.6) vary on a length scale that is much shorter than the dispersion and nonlinear lengths that control other terms. We thus introduce the concept of a transfer matrix $\mathbf{T}(z)$ that tracks linear variations induced by these two terms and make a change of variable, $\mathbf{A} = \mathbf{T}\bar{\mathbf{A}}$, where the transfer matrix $\mathbf{T}(z)$ satisfies

$$\frac{\partial \mathbf{T}}{\partial z} = \imath\delta\mathbf{B}_0\mathbf{T} + \imath\mathbf{Q}\mathbf{T}; \qquad \mathbf{T}(0) = \mathbf{I}_{\mathrm{N}}, \qquad (7.9)$$

where $\mathbf{I}_{\mathrm{N}}$ is a N $\times$ N identity matrix. In terms of the new vector $\bar{\mathbf{A}}$, the nonlinear propagation equation becomes

$$\frac{\partial \bar{\mathbf{A}}}{\partial z} + \Big(\mathbf{T}^{\mathrm{H}}\mathbf{B}_1\mathbf{T} - \frac{1}{v_{g_r}}\Big)\frac{\partial \bar{\mathbf{A}}}{\partial t} + \frac{\imath}{2}\mathbf{T}^{\mathrm{H}}\mathbf{B}_2\mathbf{T}\frac{\partial^2 \mathbf{A}}{\partial t^2} = \boldsymbol{\mathcal{N}} \qquad (7.10)$$

where the nonlinear term $\boldsymbol{\mathcal{N}}(z,t) = [\mathcal{N}_1(z,t)\ldots\mathcal{N}_N(z,t)]^{\mathrm{T}}$ is given by

$$\boldsymbol{\mathcal{N}} = \frac{\imath\gamma}{3}\iint \Big[2(\bar{\mathbf{A}}^{\mathrm{H}}\mathbf{T}^{\mathrm{H}}\mathbf{G}^{(1)}\mathbf{T}\bar{\mathbf{A}})\mathbf{T}^{\mathrm{H}}\mathbf{G}^{(1)}\mathbf{T}\bar{\mathbf{A}} + (\bar{\mathbf{A}}^{\mathrm{T}}\mathbf{T}^{\mathrm{T}}\mathbf{G}^{(2)}\mathbf{T}\bar{\mathbf{A}})\mathbf{T}^{\mathrm{H}}\mathbf{G}^{(2)*}\mathbf{T}^*\bar{\mathbf{A}}^*\Big]\,dx\,dy. \qquad (7.11)$$

This equation shows how the nonlinear effects are modified by RLMC through the transfer matrix $\mathbf{T}(z)$. To understand this more clearly, we consider the nonlinear term $\hat{\mathcal{N}}_k(z,t)$ for a specific ($k$th) mode of the fiber. This quantity contains a large number of terms ($\sim$ N$^7$ for a N-mode fiber), most of which fluctuate rapidly. However, as we have seen in earlier chapters, some of them contribute little on average. To simplify this equation, we can remove the terms which have negligible contributions to the $k^{th}$ mode of the fiber on average by using the orthogonality relation between spatial modes [eq. (7.5)] and the fact that FWM-like terms are not phase-matched when modes with large differences in their modal propagation constants are involved. The terms we are left with are the ones that guide the nonlinear evolution of the $k^{th}$ mode in the presence of linear coupling. Denoting this set of terms by $\hat{\mathcal{N}_k}$, we obtain (see Appendix A)

$$\hat{\mathcal{N}_k} = \imath\gamma \sum_{l=1}^{\mathrm{N}} \sum_{m=1}^{\mathrm{N}} \sum_{n=1}^{\mathrm{N}} \frac{2(|t_{ml}|^2|t_{nk}|^2 + t_{ml}t_{nk}t_{mk}^*t_{nl}^*)}{(1+d_{kl})(1+d_{mn})} f_{mmnn}|\bar{A}_l|^2\bar{A}_k, \tag{7.12}$$

where $d_{ij}$ is equal to 1 if $i$ and $j$ belong to a coupled mode-group and 0 otherwise. $t_{ij}$ denotes an element of the matrix $\mathbf{T}(z)$. The nonlinear coupling parameter, which we have encountered earlier in chapter 2, is given by

$$f_{plmn} = A^{\mathrm{eff}} \iint F_p^* F_l F_m^* F_n \, dx\, dy. \tag{7.13}$$

Equation (7.12) includes both the SPM and XPM-type effects. The terms with $l = k$ represent the SPM-type of nonlinearity in the form

$$\hat{\mathcal{N}}_k^{SPM} = \imath\gamma|\bar{A}_k|^2\bar{A}_k \sum_{m=1}^{\mathrm{N}} \sum_{n=1}^{\mathrm{N}} \frac{2|t_{mk}|^2|t_{nk}|^2}{(1+d_{mn})} f_{mmnn}. \tag{7.14}$$

Among these N$^2$ terms, only one term with $m = n = k$ represents the classic SPM that involves just the $k$th mode. It is easy to see that this term reduces to $\imath\gamma|t_{kk}|^4|\bar{A}_k|^2\bar{A}_k$, where $|t_{kk}|^4$ represents the fraction of the mode power that is not transferred to other modes. The other (N$^2 - 1$) terms correspond to SPM resulting from parts of the field that are transferred from the $k$th mode to other modes through RLMC. We can refer to them as intermodal SPM, since their contribution depends on the extent of overlap among various spatial modes. It should be stressed that eq. (7.12) also includes a large number of terms that result from intermodal XPM, a phenomenon that plays an important role in multimode fibers [70].

As mentioned earlier, it is often reasonable to assume that random variations of the transfer matrix $\mathbf{T}(z)$ occur on a length scale that is much shorter compared to the nonlinear and dispersion length scales. In such a situation, one can average the nonlinear terms in eq. (7.12) over refractive-index fluctuations that lead to mode coupling. As we can see from that equation, the coefficients for these terms will depend on the averaged values of the fourth-order moments of the elements of the random matrix $\mathbf{T}(z)$. In the following section, we discuss how to calculate the transfer matrix.

## 7.2 Transfer matrix for a multimode fiber

As noted in the previous section, we would need to evaluate the fourth-order moments of the transfer matrix and average them over random index fluctuations to come up with the averaged nonlinear propagation equations. In this section, we discuss the physical considerations that we need to take into account and the method used for numerically calculating the transfer matrix.

### 7.2.1 Physical considerations

All matrix elements $t_{ij}$ of the transfer matrix depend on the random variable $\Delta\epsilon(x, y, z)$ appearing in eq. (7.2). Fluctuations of $\Delta\epsilon$ can come from several physical mechanisms such as microbending, twisting, random changes in the shape and size of the fiber core and material density fluctuations. In practice, the refractive index can be assumed to remain nearly constant over a short distance, that we will assume to be the decorrelation length $l_d$ (~10 m) associated with the fluctuations in $\Delta\epsilon(x, y, z)$.

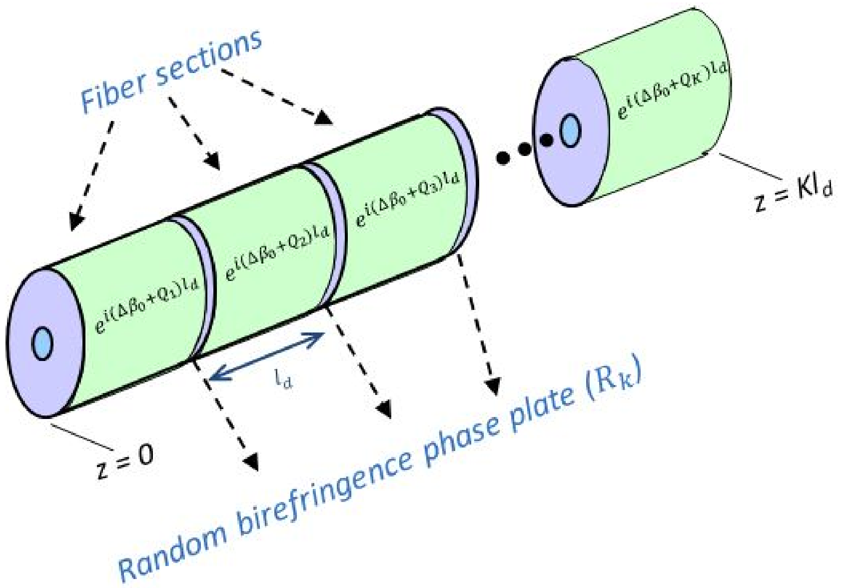


*Fig. 7.1:* Model used to compute the random linear transfer matrix $\mathbf{T}$. A fiber of length L is divided into K sections of length $l_d$, and each section is followed by a random birefringence plate.

To numerically model the transfer matrix, we divide the fiber into multiple sections of length $l_d$, as shown in Fig. 7.1. Over each section, $\Delta\epsilon$ varies randomly in the transverse plane but remains constant along the section length. We assume that $\Delta\epsilon$ is normally distributed with zero mean and a pre-specified standard deviation $\sigma_\epsilon$. It is unlikely that $\Delta\epsilon$ can fluctuate in the transverse plane on a scale shorter than 1 $\mu$m. In fact, we have numerically verified that components of $\Delta\epsilon$ with spatial frequencies higher than $1/2r$ do not contribute to linear coupling which is governed by $q_{ij}$. So, we filter all spatial frequencies above $1/2r$, where $r$ is the core radius. Figure 7.2 represents an example of $\Delta\epsilon(x, y)$ for $\sigma_\epsilon = 10^{-3}$.

The local transfer matrix of a single section can be found by solving eq. (7.9) analytically, provided the coupling matrix does not change with $z$ over the section length. The transfer matrix for a fiber of any length can then be obtained by concatenating multiple such matrices $\mathbf{T}(l_d)$, each one obtained with a statistically independent realization of perturbation $\Delta\epsilon(x, y)$.

Before proceeding to calculate the total transfer matrix $\mathbf{T}(z)$, we need to discuss the issue of polarization-division multiplexing (PDM), a technique that is used routinely for modern systems employing coherent digital receivers. Using PDM, one can transmit two orthogonally-polarized channels with identical spatial distributions in each spatial mode of the fiber. It is important to note that the coupling coefficient $q_{mp}$ in (7.7) vanishes if the two modes are orthogonal at every point in the transverse plane, i.e., if $F_m^*(x, y) \cdot F_p(x, y) = 0$. This condition is satisfied for any pair of orthogonally polarized fields. However, in

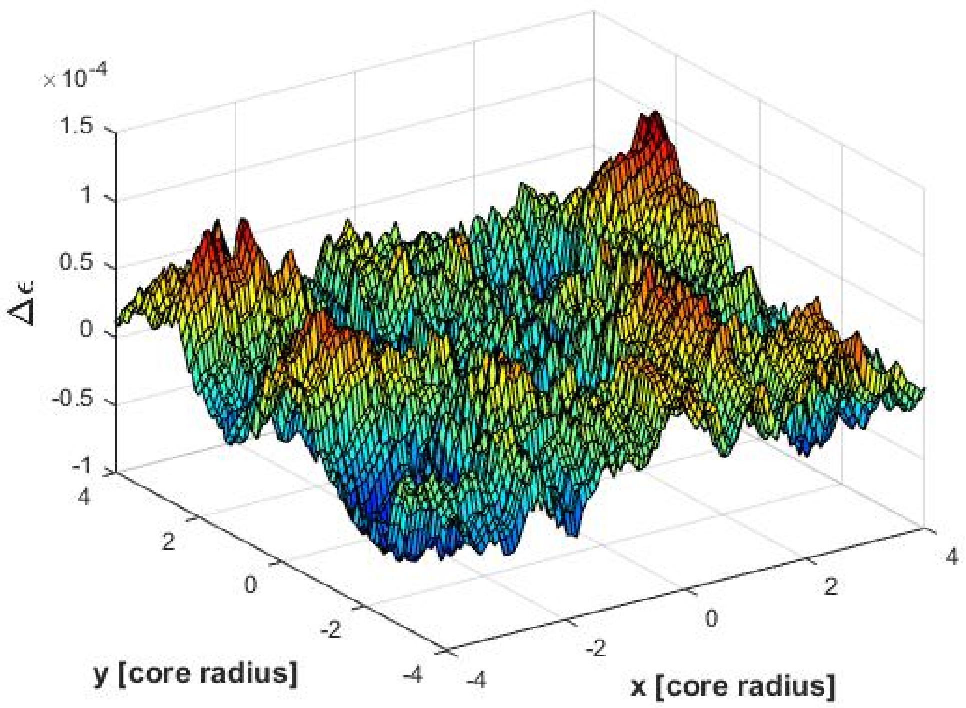


*Fig. 7.2:* An example of transverse fluctuations $\Delta\epsilon(x, y)$ in one section of the fiber. Fluctuations in two neighboring sections are assumed to be uncorrelated. The standard deviation of fluctuations is assumed to be $10^{-3}$ for the case shown here. Spatial frequencies higher than 1/2r have been filtered out, which leads to a reduction in the effective standard deviation.

practice, even orthogonally polarized modes with identical spatial distributions get strongly coupled after a certain distance because of birefringence fluctuations which lead to random polarization rotations. To take into account such random rotations, we employ the scheme shown in Fig. 7.1 and multiply the electric field of each mode by a random unitary matrix at the end of each section. In the matrix notation, this is equivalent to multiplying the transfer matrix by a block diagonal matrix $\mathbf{R}_k$, which is a N $\times$ N matrix comprising of $2 \times 2$ random unitary sub-matrices along the diagonal. The total transfer matrix of a fiber of length L=$Kl_d$ is thus given by

$$\mathbf{T} = \prod_{k=1}^{K} \mathbf{R}_k \exp\left[\imath(\delta\mathbf{B}_0 + \mathbf{Q}_k)z_f\right], \tag{7.15}$$

where $\mathbf{Q}_k$ is the coupling matrix of the $k$th section.

### 7.2.2 Numerically computing the transfer matrix

We now focus on numerically calculating the transfer matrix $\mathbf{T}$. Although the analysis is valid for HE fiber modes, we use here the basis of linearly polarized (LP) modes, employed commonly in literature on SDM [17]. The modal spatial distributions were calculated using a specific step-index few-mode fiber with core radius r=5.5 $\mu$m, V=3.8, and $\mathrm{n}_{\mathrm{clad}} = 1.444$ for cladding's refractive index. Such a fiber supports three spatial modes, denoted as

LP01, LP11a and LP11b, in the wavelength region near 1550 nm. For the remainder of this and the following chapter, all our numerical results have been computed using these fiber parameters.

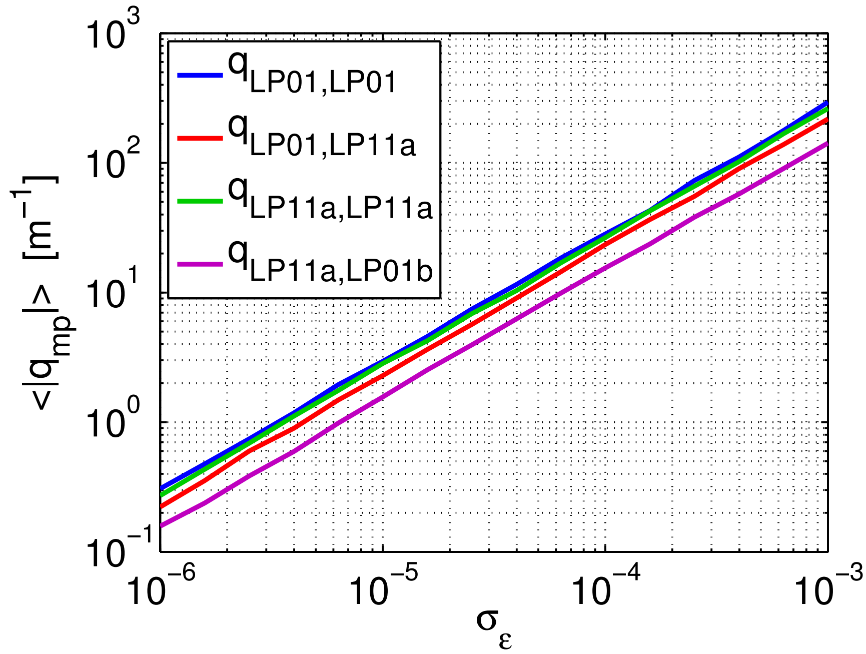


*Fig. 7.3:* Calculated average value of the magnitude of coupling coefficients as a function of the standard deviation of index fluctuations $\sigma_\epsilon$ between several pairs of modes. The index $\mathrm{LP}_{mn}$ in the subscript refers to any matrix element belonging to that spatial mode.

To generate the transfer matrix of this few-mode fiber, we begin by calculating the coupling matrix of the $k^{th}$ fiber section $\mathbf{Q}_k$. Equation (7.7) allows us to calculate its elements $q_{mp}$ between the modes $m$ and $p$ of the $k^{th}$ fiber section. The values of these matrix elements can be seen as random variations in the modal propagation constants caused by index fluctuations. Figure 7.3 shows the average value of several coupling coefficients as a function of the standard deviation of index fluctuations $\sigma_\epsilon$. We calculate the coupling matrices for each section $k$ and employ the scheme described by eq. (7.15) to generate the total transfer matrix $\mathbf{T}$.

The coupling between a pair of two modes labeled $m$ and $p$ is set by the off-diagonal element $t_{mp}$ of the transfer matrix $\mathbf{T}$, which depends not only on $q_{mp}$ but also on the difference, $\beta_{0m} - \beta_{0p}$, of the modal propagation constants. In order to see how the coupling varies with these two parameters, we consider a specific mode pair, one belonging to the LP01 mode and the other to the LP11a or LP11b modes (they are statistically equivalent). We then calculate the average value of the corresponding transfer-matrix element ($t_{\mathrm{LP01,LP11}}$) after 1 km of fiber (we choose $l_d = 50$ m for our simulations, which leads to $K = 20$). Figure 7.4 shows the average value of $t_{\mathrm{LP01,LP11}}$ as a function of the ratio $\kappa = \langle |q_{\mathrm{LP01,LP11}}|/|\Delta\beta_0|\rangle$, which can be interpreted as the normalized coupling strength. When this ratio is relatively small ($< 0.01$), the two modes are weakly coupled since $< 1\%$ of the power in one mode is transferred to the other mode. On the other hand, if this ratio is close to 1, the two modes are strongly coupled resulting in considerable flow of energy between the modes.

An important effect that we observed was that the saturation value of $1/\sqrt{2}$ in Fig. 7.4 is reached at smaller values of $\kappa$ if we choose a larger number of fiber sections $K$ (longer

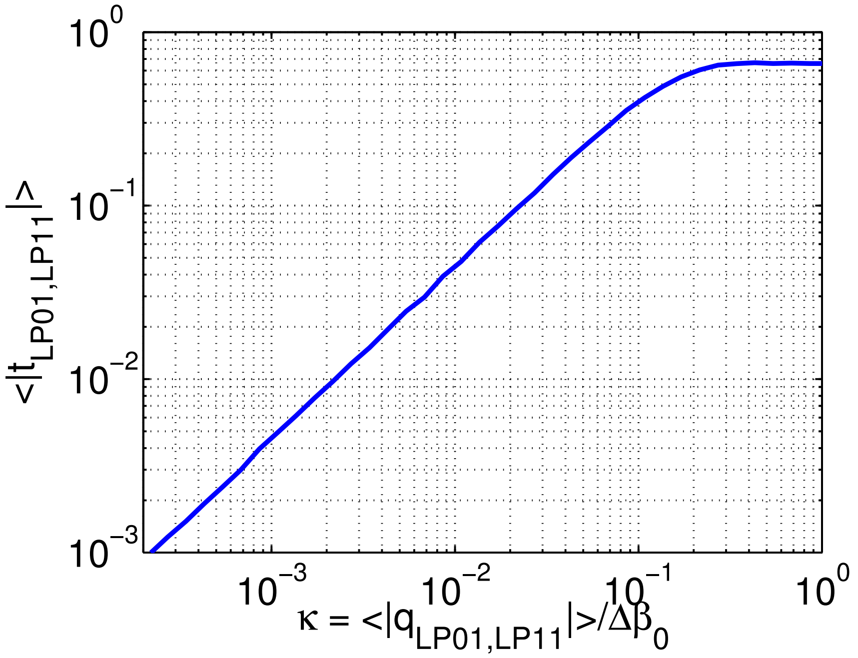


*Fig. 7.4:* Average magnitude of an off-diagonal element of the transfer matrix T, corresponding to coupling between the $LP_{01}$ and $LP_{11}$ modes, plotted as a function of the ratio of the normalized coupling strength $\kappa$ for a 1-km-long fiber.

fiber length $L$ or shorter fiber segment $l_d$). $l_d$ is the coupling length that we choose for the fiber (Appendix of Ref. [132]). Physically, this means that a shorter coupling length leads to stronger coupling between modes. The important point to note is that, for any two modes for which $\kappa$ is close to or exceeds 1, mode coupling is so strong that nearly half of the power in one mode can be transferred to the other mode even after a relatively short propagation distance of 1 km for a coupling length of a few tens of meters.

## 7.3 Averaged nonlinear propagation equations

We looked at how to compute the transfer matrix for a multimode fiber in the previous section. Eq. (7.12) is the stochastic equation that shows us how the elements of the transfer matrix, specifically their fourth-order moments, impact the nonlinear terms. To find the general multimode Manakov equations, we need to average this set of stochastic equations over several instantiations of the randomly varying refractive index ($\Delta\epsilon$).

It is important to note how the transformation from $\mathbf{A}$ to $\bar{\mathbf{A}}$ has affected the variable. $\mathbf{A}$ is a randomly varying (stochastic) quantity. But when we made the transformation $\mathbf{A} = \mathbf{T}\bar{\mathbf{A}}$, we explicitly included all the RLMC effects in $\mathbf{T}$. So $\bar{\mathbf{A}}$ is a deterministic quantity. With this in mind, we can proceed to average eq. (7.12).

We know that even in an ideal fiber, under the slowly-varying approximation (SVA), certain groups of modes can be assumed to be degenerate or nearly-degenerate. Since these modes have nearly identical propagation constants, there can be very strong linear and nonlinear coupling between these mode groups (ex: $LP_{11}$ mode group consisting of $LP_{11a}$ and $LP_{11b}$ modes). Let $S_m$ be the group of modes that couple strongly with the $m^{th}$ mode (with the convention $m \in S_m$) and let $n_m$ denote the number of modes in $S_m$.

Using these notations, we can write the average propagation equation for the $k^{th}$ mode in the following form

$$\frac{\partial \bar{A}_k}{\partial z} + (B'_{1k} - \frac{1}{v_{g1}})\frac{\partial \bar{A}_k}{\partial t} + \frac{\imath}{2}B'_{2k}\frac{\partial^2 \bar{A}_k}{\partial t^2} = \imath \sum_{l=1}^{\mathrm{N}} \sum_{m\in S_l} \sum_{n\in S_k} C_{klmn}|\bar{A}_l|^2 \bar{A}_k, \tag{7.16}$$

where $B'_{1k}$ and $B'_{2k}$ are the elements of diagonal matrices $\mathbf{B}'_1 = \langle \mathbf{T}^{\mathrm{H}}\mathbf{B}_1\mathbf{T}\rangle$ and $\mathbf{B}'_2 = \langle \mathbf{T}^{\mathrm{H}}\mathbf{B}_2\mathbf{T}\rangle$, and the nonlinear coefficients are given by

$$C_{klmn} = 2\gamma f_{mmnn} \frac{\langle |t_{ml}|^2 |t_{nk}|^2\rangle + \langle t_{ml}t_{nk}t^*_{mk}t^*_{nl}\rangle}{(1+d_{kl})(1+d_{mn})}. \tag{7.17}$$

As was discussed at the beginning of this chapter, RLMC in a multimode fiber can be categorized into different regimes. While we will qualitatively characterize each regime in the next chapter, we note here that equations (7.16) and (7.17) can be used to model the average behavior of an SDM system in any regime of RLMC. To the best of our knowledge, these are the most general averaged Manakov equations that have been derived for multimode fibers. At this point, we still have not discussed how to compute the averaged nonlinear coupling coefficients from eq. (7.17), which we will consider in detail in the next chapter.

## Conclusions

In this chapter, we have developed a formalism to derive multimode Manakov equations by averaging over several instantiations of linear coupling. The theory we present here can be applied to all regimes of RLMC, unlike the "strong" and "weak" coupling regimes that have been studied previously [30, 31, 33]. We introduced a transfer matrix that tracks the linear variations induced by random refractive index fluctuations and propagation constant difference between modes. We discussed in detail the physical and numerical considerations pertaining to computation of the transfer matrix. Finally, we presented the multimode Manakov equations applicable for all regimes of RLMC by averaging the coupled NLS equations. We found that the averaged nonlinear coefficients depend on the transfer matrix elements, specifically the fourth-order moments of the transfer matrix.

# Chapter 8

# Impact of linear coupling on nonlinear propagation

In chapter 7, we derived the multimode, Manakov, nonlinear propagation equation (7.16) averaged over fluctuations induced by random linear mode coupling (RLMC). The general Manakov equation was derived without imposing any constraints on the strength of RLMC. As we have discussed, this equation can be used to model the average nonlinear propagation behavior when RLMC is present.

However, these derived equations require the nonlinear coefficients $C_{klmn}$ as defined in eq. (7.17). These averaged nonlinear coupling coefficients depend on the fourth-order moments of the linear transfer matrix given in eq. (7.15). In this chapter, we discuss how to calculate these fourth-order matrix moments. Using the known results from theory of random matrices gives the exact analytical results for the coupling regimes where mode-groups are either strongly or weakly coupled. Most importantly, we qualitatively characterize RLMC in a multimode fiber and show the presence of an intermediate coupling regime (ICR), which exists at the transition of the two previously studied "strong" and "weak" coupling regimes. We also discuss full numerical simulations to understand the nonlinear penalties incurred by a lightwave system operating in the different coupling regimes.

In section 8.1, we focus on the fourth-order moments of the transfer matrix and see how to calculate them. We also look at some analytical results that help us in this analysis. In section 8.2, we discuss how to put the entire theory together to make it useful for modeling nonlinear propagation in multimode fibers. To verify our results, we derive averaged equations in the previously studied "strong" and "weak" coupling regimes and compare the results. In section 8.3, we perform a full numerical simulation of an SDM system and study how RLMC impacts the nonlinear penalties incurred by the system.

## 8.1 Fourth-order moments of transfer matrix

In the previous chapter, we discussed how to calculate the elements $t_{ij}$ of the transfer matrix $\mathbf{T}$. Equation (7.17) tells us that the coefficients of the averaged nonlinear term in the Manakov equation depends on the average values of the fourth-order moments of the transfer matrix $\mathbf{T}$. More specifically, we need the following four types of fourth-order moments:

$$m_{ij}^{(1)}(\mathbf{T}) = \langle |t_{ij}|^4 \rangle, \tag{8.1a}$$

$$m_{ikl}^{(2)}(\mathbf{T}) = \langle |t_{ik}|^2 |t_{il}|^2 \rangle \qquad (k \neq l), \tag{8.1b}$$

$$m_{ijkl}^{(3)}(\mathbf{T}) = \langle |t_{ik}|^2 |t_{jl}|^2 \rangle \qquad (i \neq j \text{ and } k \neq l), \tag{8.1c}$$

$$m^{(4)}_{ijkl}(\mathbf{T}) = \langle t_{ik}t_{jl}t^*_{il}t^*_{jk}\rangle \qquad (i \neq j \ \text{ and } \ k \neq l). \tag{8.1d}$$

Although the analysis that follows is general and valid for any SDM fiber, we will use a specific example fiber for the remainder of this chapter to show how to calculate these averaged nonlinear coefficients. This is the same fiber that was used to calculate the transfer matrix in the previous chapter. To recall, we consider a six-mode step-index fiber with a core diameter of 11 $\mu$m and $n_{\text{clad}}$ = 1.444 such that the normalized frequency V = 3.8 at the operating wavelength of $\lambda$ = 1.55 $\mu$m. Such a fiber supports M = 3 spatial modes (denoted by $\text{LP}_{01}$, $\text{LP}_{11a}$ and $\text{LP}_{11b}$ in the basis of linearly polarized LP modes), which, after including orthogonally polarized components of each mode, adds up to N = 6 modes.

For this example fiber, the transfer matrix $\mathbf{T}$ will be a 6×6 random matrix and we have previously seen how to calculate it. However, we know that $\text{LP}_{11a}$ and $\text{LP}_{11b}$ modes can be strongly coupled because of their degenerate nature. Additionally, the orthogonally polarized components of any spatial mode are also expected to be strongly coupled owing to birefringence fluctuations. It is thus useful to express the total transfer matrix $\mathbf{T}$ in the form

$$\mathbf{T} = \begin{bmatrix} \mathbf{T}_1 & \mathbf{T}_{12} \\ \mathbf{T}^{\text{H}}_{12} & \mathbf{T}_2 \end{bmatrix} \tag{8.2}$$

where $\mathbf{T}_1$ is a 2×2 matrix for the $\text{LP}_{01}$ mode group $g_1$, $\mathbf{T}_2$ is a 4×4 matrix for the $\text{LP}_{11}$ mode group $g_2$, and $\mathbf{T}_{12}$ is a 2×4 matrix representing coupling between these two mode groups. This coupling is induced by random index perturbations and its magnitude may vary considerably for different SDM fibers.

We calculate the average values for the individual blocks of $\mathbf{T}$ numerically. For this purpose, we recall that we had defined a dimensionless coupling parameter $\kappa$ in the previous chapter. Generalizing the definition of that parameter as

$$\kappa = \langle|q_{g1,g2}|\rangle/|\Delta\beta_{0,g1,g2}|, \tag{8.3}$$

where $\Delta\beta_{0,g1,g2}$ is the difference in propagation constants between mode groups $g1$ and $g2$ and $q_{g1,g2}$ governs the linear coupling between them. For the example fiber, $g1$ corresponds to the $\text{LP}_{01}$ group and $g2$ corresponds to the $\text{LP}_{11}$ group. Physically, $\kappa$ represents the normalized coupling strength between the two mode groups. As an example, we choose a fiber with $L$ = 1 km and $l_d$ = 50 m (the same parameters that were used to calculate $\mathbf{T}$ in the previous chapter) and numerically compute the values of the fourth-order moments as a function of this ratio $\kappa$. Figure 8.1 shows such a plot for $\mathbf{T}_1$. A striking feature in this figure is that all moments change rapidly in the range $0.01<\kappa<0.1$, but remain virtually constant outside this range.

Small and large values of $\kappa$ correspond to weak and strong coupling between mode-groups respectively. It turns out that is possible to predict the limiting values of $m^{(p)}$ analytically in these two regimes. For this purpose, we use the concept of a Haar matrix, which is a unitary random matrix whose elements are uniformly distributed over the entire range. If the coupling among mode groups is totally random in the sense that all unitary transformations are equally probable, then we expect the corresponding transfer matrix block to be a Haar matrix. Interestingly, the fourth-order moments of a Haar matrix depend only on the dimension $n$ of the matrix and are given by [133]:

$$\bar{m}^{(1)}(n) = \frac{2}{n(n+1)}, \qquad \bar{m}^{(3)}(n) = \frac{1}{(n-1)(n+1)}, \tag{8.4}$$

$$\bar{m}^{(2)}(n) = \frac{1}{n(n+1)}, \qquad \bar{m}^{(4)}(n) = \frac{-1}{(n-1)n(n+1)}, \tag{8.5}$$

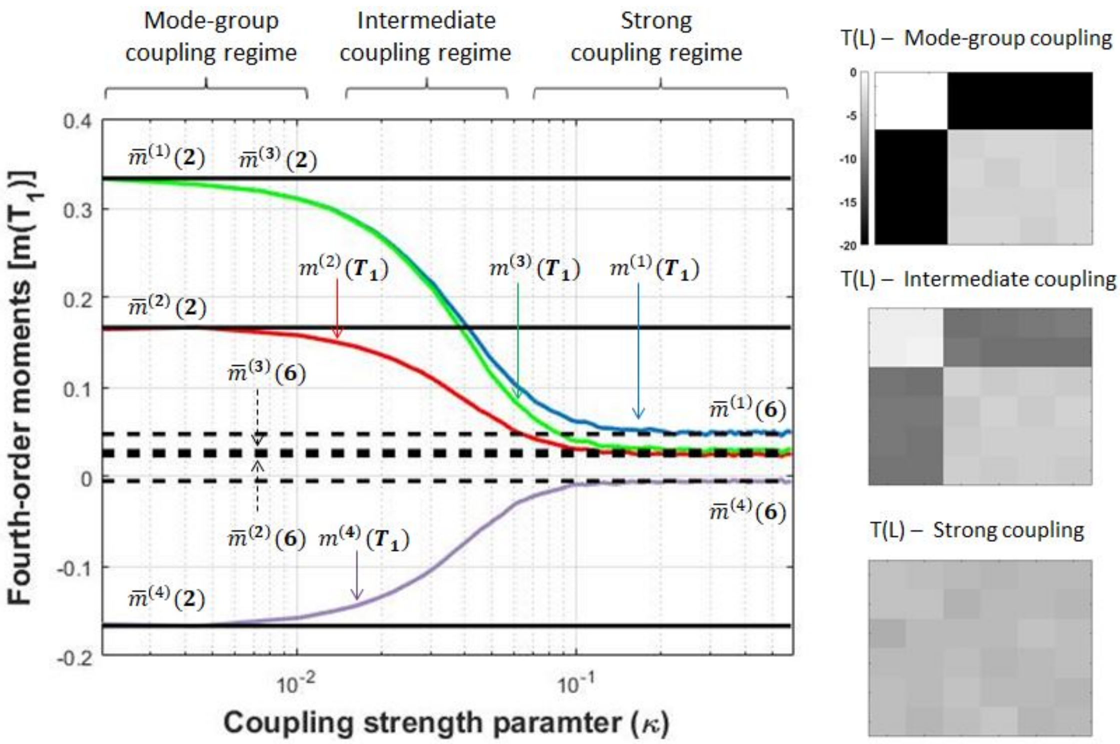


*Fig. 8.1:* Fourth-order moments of $\mathbf{T}_1$ in eq. (8.2) as a function of $\kappa$ when L = 1 km and $l_d$ = 50 m. Haar-limit predictions are shown by solid and dashed horizontal lines for $n$=2 and 6, respectively. Magnitude of numerically computed average transfer matrix elements in the three coupling regimes is shown on top using a gray-shaded logarithmic scale.

where a bar is used to indicate the Haar limit. These expressions agree with the numerical results in Fig. 8.1 in the two extreme limits of weak and strong intergroup coupling. In the case of weak coupling, $n = 2$ as $\mathbf{T}_1$ is an isolated 2×2 matrix. We call this the mode-group coupling regime (MGCR), since only the modes belonging to the same mode group are coupled with each other but inter-group coupling is negligible. This becomes more clear when we look at the numerically computed transfer matrix in the MGCR shown in Fig. 8.1, where the elements of the off-diagonal block matrix $\mathbf{T}_{12}$ have negligible values. In contrast, in the case of strong intergroup coupling, $n = 6$ since all modes are equally coupled. We call this the strong coupling regime (SCR). Again, the numerically computed transfer matrix in the SCR shows this to be true, as the values of all the elements of $\mathbf{T}$ are comparable. These analytical predictions are shown by the solid ($n = 2$) and dashed ($n = 6$) horizontal lines in Fig. 8.1. We can clearly see that the numerically computed values of the moments converge to the theoretically predicted values in the MGCR and SCR.

The transition region between these two extreme regimes, characterized by $0.01<\kappa<0.1$, is the intermediate coupling regime (ICR). The numerically computed transfer matrix in the ICR, shown in Fig. 8.1, clearly shows that the off-diagonal elements are no longer negligible and neither do they have values similar to the elements in the diagonal matrix blocks. This means that we cannot use the Haar matrix approach, since the elements are not uniformly distributed. This figure conclusively shows the presence of an intermediate coupling regime (ICR), for which no theory currently exists.

A similar analysis can be done for the 4×4 matrix block $\mathbf{T}_2$, which corresponds to the $LP_{11}$ mode group. The numerically computed fourth-order moments for $\mathbf{T}_2$ are shown in

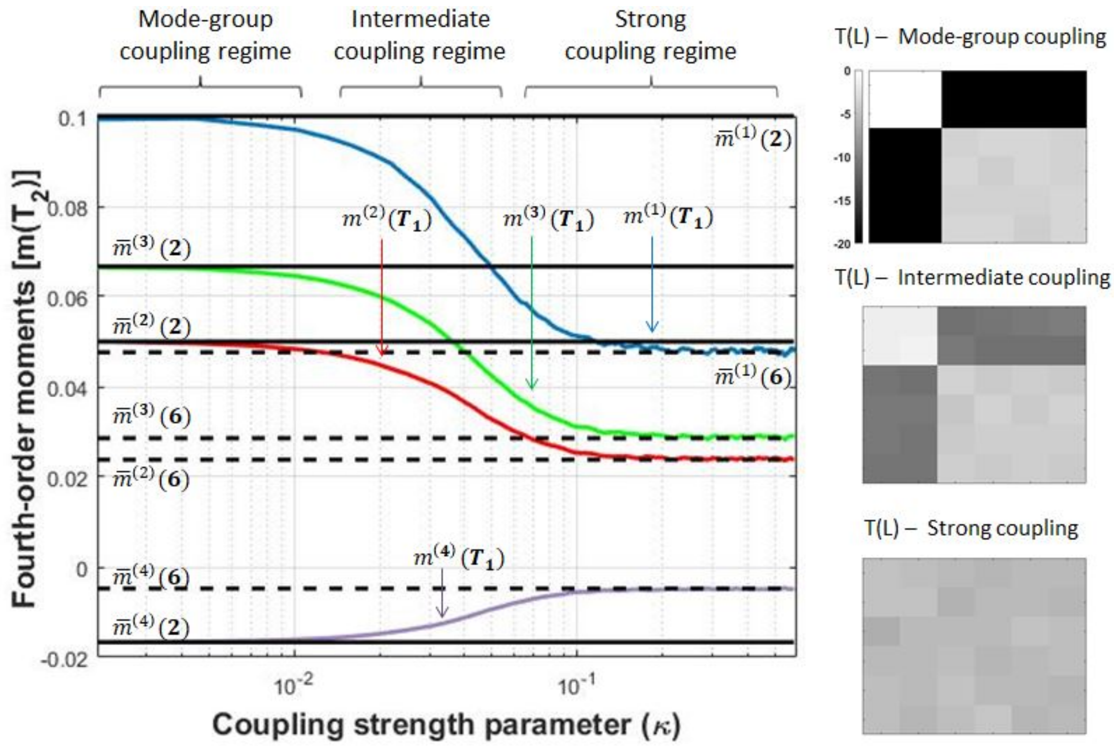


*Fig. 8.2:* Fourth-order moments of $\mathbf{T}_2$ in eq. (8.2) as a function of $\kappa$ for the same fiber parameters used to generate fig. 8.1. Haar-limit predictions are shown by solid and dashed horizontal lines for $n$=4 and 6, respectively. Magnitude of numerically computed average transfer matrix elements in the three coupling regimes is shown on top using a gray-shaded logarithmic scale.

Fig. 8.2. Here, we again show the analytically predicted values of these moments in the MGCR and SCR using $n = 4$ and $n = 6$ respectively in eqns. (8.4) and (8.5). Again, we notice the ICR in the region $0.01<\kappa<0.1$.

## 8.2 Averaged equations in different coupling regimes

Before we proceed to derive the Manakov equations in different coupling regimes, it is useful to discuss the averaged linear terms appearing in eq. (7.16). As was mentioned in chapter 7, $B^{'}_{1k}$ and $B^{'}_{2k}$ are the diagonal elements of averaged diagonal matrices $\mathbf{B}^{'}{}_1 = \langle \mathbf{T}^{\mathrm{H}}\mathbf{B}_1\mathbf{T}\rangle$ and $\mathbf{B}^{'}{}_2 = \langle \mathbf{T}^{\mathrm{H}}\mathbf{B}_2\mathbf{T}\rangle$. It is important to note that numerical verification shows that non-diagonal elements of $\mathbf{B}^{'}{}_1$ and $\mathbf{B}^{'}{}_2$ are negligible compared to the diagonal elements, no matter which coupling regime we are operating in. To understand what these diagonal elements would turn out to be, in different coupling regimes, and the associated physical impact, we will use our example fiber.

For the specific six-mode fiber that we have used as an example here, we split the diagonal matrix $\mathbf{B}_1$ in two mode groups and write it as

$$\mathbf{B}_1 = \begin{bmatrix} \mathbf{B}_1^{g1} & \mathbf{0} \\ \mathbf{0} & \mathbf{B}_1^{g2} \end{bmatrix}, \tag{8.6}$$

where $\mathbf{B}_1^{g1}$ is a 2×2 diagonal matrix, $\mathbf{B}_1^{g2}$ is a 4×4 diagonal matrix, and 0 is a null matrix. The elements of $\mathbf{B}^{'}_1 = \langle \mathbf{T}^{\mathrm{H}}\mathbf{B}_1\mathbf{T}\rangle$ can be calculated numerically by first calculating the transfer matrix $\mathbf{T}$ and averaging over a large ensemble. Moreover, we can calculate the averaged values analytically in the two limiting cases representing the MGCR and SCR.

In the MGCR limit, diagonal elements in each group become identical and take values $\mathrm{Tr}(\mathbf{B}_1^g)/\mathrm{Dim}(\mathbf{B}_1^g)$, where Tr and Dim represent the trace and dimension of each sub-matrix, respectively. Physically, this means that all the modes within a strongly coupled mode-group travel at the same speed on average. The same result applies in the SCR limit. However, the matrix $\mathbf{B}_1$ can no longer be divided into subgroups as all modes become strongly coupled. Thus, all diagonal elements of $\mathbf{B}_1^{'}$ become the same and take the value $\mathrm{Tr}(\mathbf{B}_1)/6$. Physically, when all modes are strongly coupled, they all end up traveling at the same group velocity on average. Both of these analytic predictions have been verified numerically. However, in the ICR, we do not have an analytical expression that can provide the values of these diagonal elements and they need to be computed numerically. The values of these diagonal elements only fluctuate between the maximum and the minimum diagonal values of the original matrix $\mathbf{B}_1$. The elements of $\mathbf{B}_2^{'} = \langle \mathbf{T}^{\mathrm{H}} \mathbf{B}_2 \mathbf{T} \rangle$ can be calculated in a similar manner.

Now that we have discussed the linear terms in the averaged Manakov equations, we move to the nonlinear coefficients. Once the values of averaged fourth-order moments (from section 8.1) are known, they can be used in the propagation eqs. (7.16) and (7.17) to model the average behavior of an SDM system in any regime of linear coupling. To validate further our general expression in eq. (7.17), we apply it to the two extreme coupling regimes that have been studied earlier (see Appendix B for detailed derivation).

In the MGCR, only some modes (with a larger value of $\kappa$) are strongly coupled. In this limit,

$$C_{klmn}(\mathrm{MGCR}) = \frac{2\gamma}{n_k} \frac{1}{n_l + d_{lk}} f_{mmnn}, \tag{8.7}$$

where, as before, $d_{mk}$ is 1 when $m$ and $k$ belong to a coupled mode-group but 0 otherwise. This is a general expression which allows for strong coupling between degenerate modes. In the SCR, all modes are assumed to be equally coupled, which means that $S_k$ and $S_m$ contain all $N$ modes ($n_k = n_m = N$). Under this condition, we get

$$C_{klmn}(\mathrm{SCR}) = \frac{2\gamma}{N(N+1)} f_{mmnn}. \tag{8.8}$$

Both of these cases have also been studied in the past [30, 31, 33], and our formulas agree with earlier results. Indeed, if we consider the case of a single-mode fiber that only supports two orthogonally polarized modes, we can substitute $N = 2$ in eq. (8.8) and the equation reduces to the well-known Manakov PMD equations [130]. It can be concluded from these results that, in general, the nonlinear terms are smaller when all modes of a multimode fiber are strongly coupled (because of the presence of the factor N(N + 1) in the denominator).

In the ICR, the nonlinear terms in eq. (7.17) depend on the coupling parameter $\kappa$. In this case, we saw that the transfer matrix does not reduce to a Haar matrix as its elements are not uniformly distributed. However, we can compute the nonlinear coefficients numerically and use them in eq. (7.16) to model the system performance. We have observed that the transition region of intermediate coupling seen in Figs. 8.1 and 8.2 becomes slightly narrower as the system length increases. Thus, our results allows us to predict where the transition to the ICR would occur for any SDM fiber.

Now that we have separately studied all aspects of this new theoretical model using an example six-mode fiber that has two separate mode-groups, we will briefly discuss how this theory can be used for any given multimode fiber. The averaging method discussed here can be applied to all SDM fibers with any number of spatial mode-groups. For fibers with more than two mode groups, each mode-group pair can have different strengths of RLMC (different $\kappa$). Recall here that $\kappa$ is defined with respect to a mode-group pair. Calculating the value of $\kappa$ for any mode-group pair can also give us the information about which coupling regime those two mode groups belong to. Indeed, all three coupling regimes can exist in a single fiber. One needs to calculate the nonlinear coefficients in eq. (7.17) separately for each mode-group pair and then use those coefficients in eq. (7.16) to model the average nonlinear transmission. In addition, if a mode-group pair lies in the SCR or MGCR, then we have also shown analytical solutions to eq. (7.17) which can be used for modeling.

## 8.3 Full numerical simulation of an SDM system

To show how useful the results shown in this chapter are for modeling realistic SDM systems and to verify their accuracy, we perform a full numerical simulation for a specific SDM system and predict the optical signal-to-noise ratio (OSNR) in different coupling regions. For this purpose, we focus again on the same few-mode fiber used in earlier sections supporting 3 distinct spatial modes, each with two orthogonal polarizations (N=6).

Using this six-mode fiber, we transmit six QPSK-format data streams, each at 28.5 Gbaud (bit rate 57 Gb/s). The 1000-km-long transmission line consists of 10 spans of 100-km fiber, each followed by a fiber amplifier that compensates for all span losses. No dispersion management is employed along the fiber link, but all linear impairments are assumed to be perfectly compensated at the digital receiver.

To calculate the actual bit-error rate (BER) numerically, $2^{20}$ symbols are transmitted through the fiber in the form of 256 identical copies of $2^{12}$ randomly selected symbols. The injected power per polarization and per mode is 3 dBm. We solve eq. (7.10) numerically using the split-step Fourier method with a step size $l_d = 100$ m. This value corresponds to a nonlinear phase shift of less than 0.05 rad per step. We assume that the fiber's refractive index varies randomly in the x–y plane, as indicated in eq. (7.2), and we pick a new set of random functions $\Delta\epsilon(x, y)$ at each step.

The propagation constants and spatial profiles of the three spatial modes supported by the example fiber were calculated numerically. The $LP_{11a}$ and $LP_{11b}$ modes are nearly degenerate and their propagation constants almost coincide. In contrast, the difference between the propagation constants of $LP_{01}$ and $LP_{11}$ modes is $\Delta\beta_0 = 1.4 \times 10^4$ m$^{-1}$, and the corresponding differential modal group delay $\Delta\beta_1 = 4.1$ ns/km. The $LP_{01}$ and $LP_{11}$ modes have dispersion parameters $[D = (-2\pi c/\lambda^2)\beta_2]$ of 23 and 18 ps/(km-nm) and their effective mode area ($A_{\text{eff}}$) are 78 and 81 $\mu$m$^2$, respectively. This fiber has a nonlinear parameter of $\gamma = 1.4$ W$^{-1}$/km and a loss coefficient of 0.2 dB/km.

Figure 8.3 shows the optical signal-to-noise ratio (OSNR) penalties (compared to the back-to-back performance) at a BER of $10^{-3}$ as a function of standard deviation $\sigma_\epsilon$ of index fluctuations. We stress that these penalties are solely due to nonlinear impairments as all linear degradations are perfectly compensated by the receiver. We have verified that in the absence of nonlinearity, no degradation is observed. By changing $\sigma_\epsilon$, we modify the strength of random linear mode coupling, and thus change the impact of nonlinearities on the system performance. The horizontal dashed lines are obtained by replacing $\mathcal{N}_k(z, t)$ in eq. (7.12) with its average value given in eq. (8.7) or eq. (8.8) in the two limiting cases.

Several points are noteworthy in Fig. 8.3. First, our full numerical simulations agree with the limiting value of 2.5-dB penalty obtained using the averaged nonlinear term when

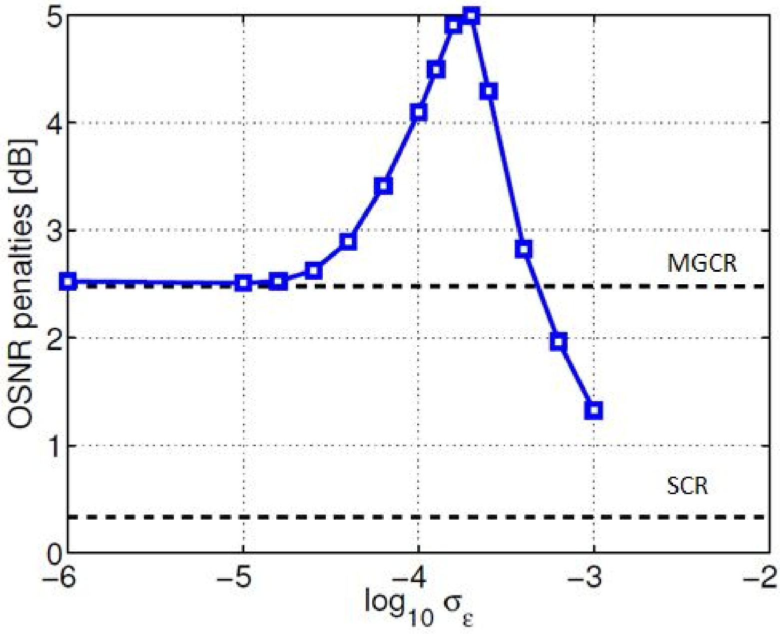


*Fig. 8.3:* OSNR penalties as a function of $\sigma_\epsilon$ when six SDM–PDM channels are transmitted over 1000 km at 28 Gbaud using the QPSK format for a six-mode fiber. Horizontal dashed lines show the penalties in the mode-group and strong coupling limits using the average values of the nonlinear terms.

index fluctuations are so small that one is operating in the MGCR. Second, we did not reach the SCR for our fiber for the largest value of $\sigma_\epsilon = 10^{-3}$ used in numerical simulations. We did not consider larger values because of a relatively small core-cladding difference ($< 0.01$) for our fiber. Although, we have verified that the SCR is reached in fibers designed with a smaller value of $\Delta\beta_0$ so that $\kappa$ is enhanced. The agreement of full numerical simulations in the two limiting cases, studied by using the averaged nonlinear terms, indicates that the averaging procedure discussed in earlier sections is accurate and can be used to reduce the computation time by a large factor.

The most important feature seen in Fig. 8.3 is the sharp peak occurring in the ICR. Our numerical simulations show that nonlinear penalties increase in the ICR and become as large as 5 dB for a specific value of $\sigma_\epsilon$. Clearly, the peak region should be avoided in real SDM systems by designing multimode fibers such that the system is operating either in the MGCR or SCR, but not in between the two limits. Moreover, it is preferable to operate in the SCR where the penalty is reduced to mere 0.3 dB. However, operation in this limit requires that the multimode fiber be designed such that the propagation constants for all modes are not too far apart from each other. This may be possible to realize in graded-index multimode fibers designed to support a large number of modes.

## Conclusions

In this chapter, we used the averaged equations derived in the previous chapter and discussed how to use them to model nonlinear propagation in a multimode fiber. This was done by using a six-mode fiber as an example. We calculated the fourth-order moments of the linear transfer matrix. The nonlinear coefficients of the averaged equations were found to depend on the averaged fourth-order moments. By looking at these moments as a function of a normalized coupling strength parameter, we could show three distinct coupling regimes. Using the concept of a Haar matrix, we were able to obtain analytical estimates in the two limiting mode-group coupling and strong coupling regimes, which agreed with the numerical results. Moreover, our results in these two extreme regimes are able to reproduce the equations derived previously [30, 31, 33]. Finally, we verified the validity of the averaging procedure through a full numerical simulation of an SDM transmission system. Our numerical results show that in the intermediate coupling regime, OSNR penalties are enhanced.

The method described here can be applied to all SDM fibers with any number of mode-groups. To the best of our knowledge, we have derived the most general averaged propagation equations that can help reduce computation time by a factor of 100 or more.

# Chapter 9

# Characterization of linear coupling in coupled-core fibers

In the previous two chapters, we developed a detailed theoretical model to study the impact of random linear coupling on nonlinear propagation. Linear coupling may occur due to a variety of reasons, including but not limited to density fluctuations, microbending, variations in shape and size of the core. This is an effect that is important to include for long-distance propagation applications, like space-division multiplexing (SDM) telecom systems.

SDM can be employed using either multimode fibers or multicore fibers [7]. In this chapter, we will discuss an experiment that was set up to characterize linear coupling in multicore fibers. Several theoretical frameworks have been proposed to model specific linear coupling impairments in both multimode and multicore fibers [134–139]. Our setup allows us to measure the Rayleigh backscattering amplitudes from each core simultaneously, which lets us characterize the cross-talk between the fibers non-destructively. The characterization is performed using an optical vector network analyzer. We try several different coupled-core pairs, each with a different strength of core-coupling.

In section 9.1, we go over the experimental setup and describe the special multicore fiber that was used for the experiment. This study is a work in progress, so in section 9.2, we look at the future work that is planned with regards to processing the data acquired using this setup and what we expect to understand from this experiment.

## 9.1 Experimental setup

This experiment was done at Nokia Bell Labs in Holmdel, NJ, USA. We used several proprietary coupled-core fibers with different core spacing. While pulses traveling in adjacent cores do not overlap spatially, there is some evanescent coupling of their spatial tails. So it is important to understand how core spacing affects linear coupling. The idea is to launch a swept laser beam into one core of the coupled-core pair and try to study how light gets coupled from one core to the other by measuring the back-scattered signal from each core individually.

A schematic of the experimental setup is shown in Fig. 9.1. The figure also shows the fiber that we use for this experiment. As we can see, it has six pairs of coupled-core fibers and one single-core fiber. Using 3 translational and 1 rotational degrees of freedom, we can choose to couple light into a specific core that belongs to a particular coupled-core pair. We launch a laser that sweeps over the C+L optical communication bands (1520 nm - 1630 nm), which is generated inside an optical vector network analyzer (OVNA). Optical

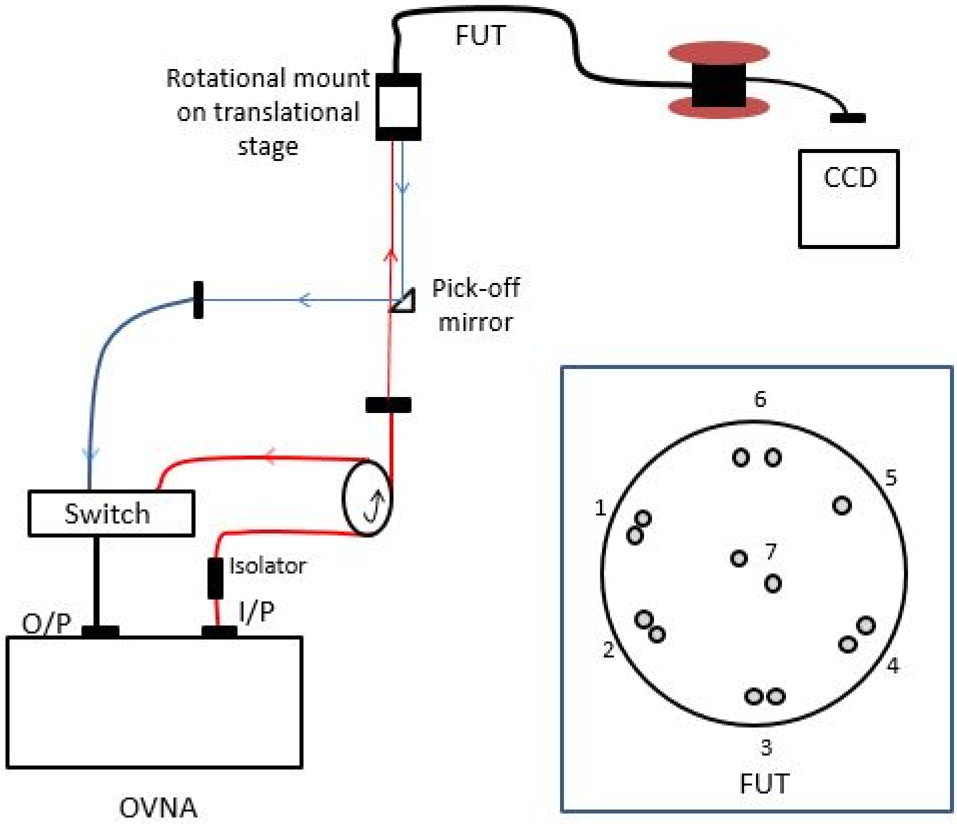


*Fig. 9.1:* Schematic of the experimental setup used to measure Rayleigh back-scattered data from coupled-core fibers. Red beam path indicates light going in to (or coming out of) the core into which a swept laser is launched and blue beam path corresponds to light coming out of the other core. OVNA = optical vector network analyzer, FUT = fiber under test, CCD = charge coupled device. A cross-section of the FUT is also shown in the bottom right corner.

vector network analysis is often used to characterize and study SDM fibers [140, 141]. A basic schematic for the OVNA that was used is shown in Fig. 9.2. This figure is taken from [142]. The OVNA comprises of the setup in Fig. 9.2 that lies outside the box with dashed boundary.

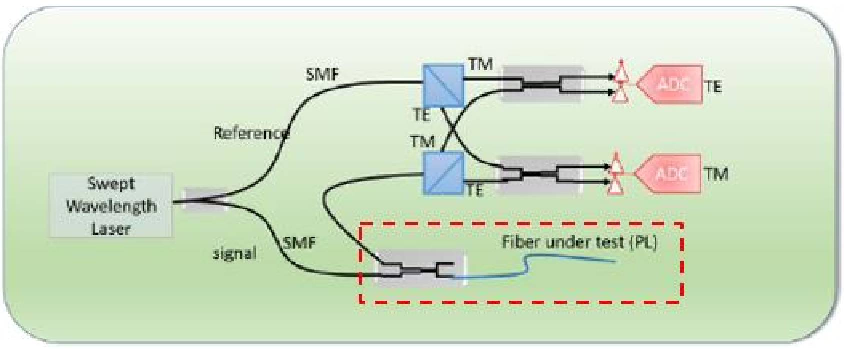


*Fig. 9.2:* Schematic of the optical vector network analyzer (from [142]). Polarization diversity receivers are used in this setup. The configuration outside dashed box is what is contained inside the box labeled "OVNA" in fig. 9.1.

Using the setup shown in Fig. 9.1, we launch the swept laser into a specific core and collect the back-scattered data coming from both the cores. We can control which core we are launching the swept laser into by looking at the output from the fiber using a charge-coupled device (CCD) camera. We can simultaneously detect the light being back-scattered from each core using the OVNA. Since we only launched light into one of the cores, the back-scattered light collected from the other core can be used to characterize how much energy is being transferred from one core to the other because of linear coupling. We use very low powers to safely ignore nonlinear effects.

The back-scattered signal is very weak and often difficult to observe because of the large reflection peaks that occur at fiber-air interfaces. For this reason, we angle-cleave the input end of the fiber under test and apply an index gel at the other end. This ensures that the reflected signals do not follow the path back to the OVNA. It is also essential to align the setup very precisely in order to obtain a signal-to-noise ratio (SNR) that leads to a discernible signal.

Finally, we repeated this experiment with another proprietary fiber that has a two-core, three-core and a six-core fiber within one cladding. Again, we launched light into one of the cores, but this time we only collected the back-scattered data from the same core.

## 9.2 Future work

The back-scattered data acquired using the OVNA for the experiments mentioned above is currently being analyzed. The plan is to understand the correlation between the signal from different cores, a process that has been performed for single-mode and polarization division multiplexing (PDM) fibers. However, instead of the autocorrelations performed for PDM fibers, we will look at cross-correlation between the two back-scattered signals. A theoretical model for Rayleigh scattering will also be used to understand what back-scattered signal we should expect.

The time delay of the back-scattered light corresponds to the distance propagated within the fiber. So this data can also tell us how the energy is distributed within the two cores after propagating a certain distance. This time to space mapping can help understand the characteristic coupling length for the different pairs of coupled-core fibers in a non-destructive manner. Since we expect linear coupling to be present in real fibers, we expect the energy to periodically move from one core to the other in the case of coupled-core fibers. The length of this period is expected to decrease with increasing strength of coupling, which depends on how closely spaced the cores are. Even for the three-core and six-core fibers, we expect linear coupling to be strong between nearest neighbors. Indeed, we observe that the back-scattered signal from one core oscillates periodically.

There can be two major reasons why we would observe any back-scattered signal from the neighboring (un-pumped) core. For completely random linear coupling, optical energy is expected to periodically move from one core to another. So we will see a back-scattering signal from the un-pumped core. This signal is proportional to the amplitude of light present in that particular core. Another, less likely possibility is that back-scattered light from one core gets coupled into the other core. A detailed understanding of Rayleigh scattering inside an optical fiber will help understand this behavior.

Unlike the completely random linear coupling that may occur because of density fluctuations or variations in shape and size of the core that are introduced during the fabrication process, there are certain perturbations that cause the optical energy to be distributed asymmetrically among the two cores. Examples of such perturbations are bending or twist in the fiber. We have taken measurements under several such situations that include: introducing macro and micro bends at random locations in the fiber, pinching the fiber, spooling the fiber around spools of different radii and laying out the fiber straight.

The data collected under all these different conditions will help characterize linear coupling between different cores of a multicore fiber and how it depends on specific perturbations. The combination of a swept laser and polarization diversity receivers also ensures that we will be able to observe whether linear coupling because of certain perturbations has any spectral or polarization preference. Similar data has been collected for the case of three-core and six-core fibers.

## Conclusion

We have described an experiment that was performed to characterize the extent of linear coupling between coupled-core fibers. We do this by launching a swept laser source in one core and looking at the Rayleigh back-scattered data from both cores simultaneously. The data is collected using an optical vector network analyzer (OVNA). This experiment is repeated for several different external perturbations and for six different core-separations. In addition, a three-core and six-core configuration were also studied. The data for these experiments is currently being analyzed and in the future, we plan to come up with a physical model to understand the linear coupling behavior that is experimentally demonstrated.

# Bibliography


[1] G. P. Agrawal, *Nonlinear Fiber Optics*. Academic, 2013.

[2] G. P. Agrawal, *Fiber-Optic Communication Systems*. Wiley, 2013.

[3] S. Berdague and P. Facq, "Mode-division multiplexing in optical fibers," *Appl. Opt.*, vol. 21, pp. 1950–1955, 1982.

[4] H. R. Stuart, "Dispersive multiplexing in multimode optical fiber," *Science*, vol. 289, pp. 281–283, 2000.

[5] S. Fan and J. Kahn, "Principal modes in multimode waveguides," *Opt. Lett.*, vol. 30, pp. 135–137, 2005.

[6] P. J. Winzer, "Optical networking beyond wdm," *IEEE Photon. J.*, vol. 4, pp. 647–651, 2012.

[7] D. J. Richardson, J. M. Fini, and L. E. Nelson, "Space-division multiplexing in optical fibers," *Nature Photonics*, vol. 7, pp. 354–362, 2013.

[8] R. N. Mahalati, R. Y. Gu, and J. M. Kahn, "Resolution limits for imaging through multi-mode fiber," *Opt. Express*, vol. 21, pp. 1656–1668, 2013.

[9] I. Papadopoulos, S. Farahi, C. Moser, and D. Psaltis, "High-resolution, lensless endoscope based on digital scanning through a multimode optical fiber," *Biomed. Opt. Express*, vol. 4, pp. 260–270, 2013.

[10] M. Ploschner, T. Tyc, and T. Cizmar, "Seeing through chaos in multi-mode fibers," *Nat. Photon.*, vol. 9, pp. 529–535, 2015.

[11] E. E. Morales-Delgado, D. Psaltis, and C. Moser, "Two-photon imaging through a multimode fiber," *Opt. Express*, vol. 23, pp. 32158–32170, 2015.

[12] E. Nazemosadat and A. Mafi, "Nonlinear switching in multicore versus multimode waveguide junctions for mode-locked laser applications," *Opt. Express*, vol. 21, pp. 30739–30745, 2013.

[13] L. G. Wright, D. N. CHristodoulides, and F. W. Wise, "Spatiotemporal mode-locking in multimode fiber lasers," *Science*, vol. 358, pp. 94–97, 2017.

[14] R.-J. Essiambre, G. Kramer, P. J. Winzer, G. J. Foschini, and B. Goebel, "Capacity limits of optical fiber networks," *J. Lightw. Technol.*, vol. 28, pp. 662–701, 2010.

[15] R. Ryf, S. Randel, A. H. Gnauck, C. Bolle, R. J. Essiambre, P. J. Winzer, D. W.Peckham, A. McCurdy, and R. Lingle, "Space-division multiplexing over 10 km of three-mode fiber using coherent 6x6 mimo processing," *Proc. Opt. Fiber Commun. Conf. Expo./Nat. Fiber Opt. Eng. Conf.*, pp. 1–3, 2011.

[16] E. Ip, N. Bai, Y. K. Huang, E. Mateo, F. Yaman, M. J. Li, S. Bickham, S. Ten, J. Linares, C. Montero, V. Moreno, X. Prieto, V. Tse, K. Chung, A. Lau, H. Y. Tam, C. Lu, Y. Luo, G. D. Peng, and G. Li, "88x3x112-gb/s wdm transmission over 50 km of three-mode fiber with inline few-mode fiber amplifier," *Proc. 37th Eur. Conf. Opt. Commun.*, pp. 1–3, 2011.

[17] R. Ryf, S. Randel, A. H. Gnauck, C. Bolle, A. Sierra, S. Mumtaz, M. Esmaeelpour, E. Burrows, R. Essiambre, P. Winzer, D. Peckham, A. McCurdy, and R. Lingle, "Mode-division multiplexing over 96 km of few-mode fiber using coherent 6×6 mimo processing," *J. Lightw. Technol.*, vol. 30, pp. 521–531, 2012.

[18] C. Koebele, M. Salsi, L. Milord, R. Ryf, C. Bolle, P. Sillard, S. Bigo, and G. Charlet, "40 km transmission of five mode division multiplexed data streams at 100 gb/s with low mimo-dsp complexity," *Proc. 37th Eur. Conf. Opt. Commun.*, pp. 1–3, 2011.

[19] E. Ding, S. Lefrancois, J. N. Kutz, and F. W. Wise, "Scaling fiber lasers to large mode-area: An investigation of passive mode-locking using multi-mode fiber," *J. Quantum Electron.*, vol. 47, pp. 597–606, 2011.

[20] A. Mafi, P. Hofmann, C. J. Salvin, and A. Schulzgen, "Low-loss coupling between two single-mode optical fibers with different mode-field diameters using a graded-index multimode optical fiber," *Opt. Lett.*, vol. 36, pp. 3596–3598, 2011.

[21] P. Hofmann, A. Mafi, C. J. Salvin, T. Tiess, N. Peyghambarian, and A. Schulzgen, "Detailed investigation of mode-field adapters utilizing multimode-interference in graded index fibers," *J. Lightw. Technol.*, vol. 30, pp. 2289–2298, 2012.

[22] F. Poletti and P. Horak, "Dynamics of femtosecond supercontinuum generation in multimode fibers," *Opt. Express*, vol. 17, pp. 6134–6147, 2009.

[23] A. Mafi, "Pulse propagation in a short nonlinear graded-index multimode optical fiber," *J. Lightw. Technol.*, vol. 30, pp. 2803–2811, 2012.

[24] R. H. Stolen, J. E. Bjorkholm, and A. Ashkin, "Phase-matched threewave mixing in silica fiber optical waveguides," *Appl. Phys. Lett.*, vol. 24, pp. 308–310, 1974.

[25] A. Hasegawa, "Self-confinement of multimode optical pulse in a glass fiber," *Opt. Lett.*, vol. 5, pp. 416–417, 1980.

[26] B. Crosignani and P. D. Porto, "Soliton propagation in multimode optical fibers," *Opt. Lett.*, vol. 6, pp. 329–330, 1981.

[27] C. Lin and M. A. Bosch, "Large-stokes-shift stimulated fourphoton mixing in optical fibers," *Appl. Phys. Lett.*, vol. 38, pp. 479–481, 1981.

[28] B. Crosignani, A. Cutolo, and P. D. Porto, "Coupled-mode theory of nonlinear propagation in multimode and single-mode fibers: envelope solitons and self-confinement," *J. Opt. Soc. Am. B*, vol. 72, pp. 1136–1141, 1982.

[29] F. Poletti and P. Horak, “Description of ultrashort pulse propagation in multimode optical fibers,” *J. Opt. Soc. Am. B*, vol. 25, pp. 1645–1654, 2008.

[30] A. Mecozzi, C. Antonelli, and M. Shtaif, “Nonlinear propagation in multi-mode fibers in the strong coupling regime,” *Opt. Express*, vol. 20, pp. 11673–11678, 2012.

[31] A. Mecozzi, C. Antonelli, and M. Shtaif, “Coupled manakov equations in multimode fibers with strongly coupled groups of modes,” *Opt. Express*, vol. 20, pp. 23436–23441, 2012.

[32] W. H. Renninger and F. W. Wise, “Optical solitons in graded-index multimode fibers,” *Nat. Commun.*, vol. 4, p. 1719, 2013.

[33] S. Mumtaz, R. J. Essiambre, and G. P. Agrawal, “Nonlinear propagation in multimode and multicore fibers: Generalization of the manakov equations,” *J. Lightw. Technol.*, vol. 31, pp. 398–406, 2013.

[34] H. Pourbeyram, G. P. Agrawal, and A. Mafi, “Stimulated raman scattering cascade spanning the wavelength range of 523 to 1750 nm using a graded-index multimode optical fiber,” *Appl. Phys. Lett.*, vol. 102, p. 201107, 2013.

[35] L. G. Wright, W. H. Renninger, D. N. Christodoulides, and F. W. Wise, “Spatiotemporal dynamics of multimode optical solitons,” *Opt. Express*, vol. 23, pp. 3492–3506, 2015.

[36] L. G. Wright, D. N. CHristodoulides, and F. W. Wise, “Controllable spatiotemporal nonlinear effects in multimode fibres,” *Nat. Photon.*, vol. 9, pp. 306–310, 2015.

[37] L. G. Wright, S. Wabnitz, D. N. Christodoulides, and F. W. Wise, “Ultrabroadband dispersive radiation by spatiotemporal oscillation of multimode waves,” *Phys. Rev. Lett.*, vol. 115, p. 223902, 2015.

[38] S. Buch and G. P. Agrawal, “Soliton stability and trappnig in multimode fibers,” *Opt. Lett.*, vol. 40, pp. 225–228, 2015.

[39] M. Guasoni, “Generalized modulational instability in multimode fibers: Wideband multimode parametric amplification,” *Phys. Rev. A*, vol. 92, p. 033849, 2015.

[40] S. Buch and G. P. Agrawal, “Intermodal soliton interaction in nearly degenerate modes of a multimode fiber,” *J. Opt. Soc. Am. B*, vol. 33, pp. 2217–2224, 2016.

[41] L. G. Wright, Z. Zhu, D. A. Nolan, M.-J. Li, D. N. Christodoulides, and F. W. Wise, “Self-organized instability in graded-index multimode fibre,” *Nat. Photon.*, vol. 10, pp. 771–776, 2016.

[42] K. Krupa, A. Tonello, A. Barthélémy, V. Couderc, B. M. Shalaby, A. Bendahmane, G. Millot, and S. Wabnitz, “Observation of geometric parametric instability induced by the periodic spatial self-imaging of multimode waves,” *Phys. Rev. Lett.*, vol. 116, p. 183901, 2016.

[43] Z. Liu, L. Wright, D. N. Christodoulides, and F. W. Wise, “Soliton propagation in multimode optical fibers,” *Opt. Lett.*, vol. 41, pp. 3675–3678, 2016.

[44] Z. Zhu, L. G. Wright, D. N. Christodoulides, and F. W. Wise, “Observation of multimode solitons in few-mode fibers,” *Opt. Lett.*, vol. 41, pp. 4819–4822, 2016.

[45] H. Pourbeyram and A. Mafi, “Photon pair generation in multimode optical fibers via intermodal phase matching,” *Phys. Rev. A*, vol. 94, p. 023815, 2016.

[46] K. Krupa, A. Tonelo, B. M. Shalaby, M. Fabert, A. Barthélémy, G. Millot, S. Wabnitz, and V. Couderc, “Spatial beam self-cleaning in multimode fibres,” *Nat. Photon.*, vol. 11, pp. 237–241, 2017.

[47] H. Pourbeyram and A. Mafi, “Photon pair generation with tailored frequency correlations in graded-index multimode fibers,” *Opt. Lett.*, vol. 43, pp. 2018–2021, 2018.

[48] H. Hasegawa and Y. Kodama, *Solitons in Optical Communications*. Oxford University Press, 1995.

[49] J. T. Taylor, P. L. Knight, and A. Miller, *Optical Solitons - Theory and Experiment*. Cambridge University Press, 2005.

[50] L. F. Mollenauer and J. P. Gordon, *Solitons in Optical Fibers: Fundamentals and Applications*. Academic, 2006.

[51] R. H. Stolen, “Modes in fiber optical waveguides with ring index profiles,” *Appl. Optics*, vol. 14, pp. 1533–1537, 1975.

[52] S. Trillo and S. Wabnitz, “Parametric and raman amplification in birefringent fibers,” *J. Opt. Soc. Am. B*, vol. 9, pp. 1061–1082, 1992.

[53] S. G. Murdoch, R. Leonhardt, and J. D. Harvey, “Polarization modulation instability in weakly birefringent fibers,” *Opt. Lett.*, vol. 20, pp. 866–868, 1995.

[54] M. Lehtonen, G. Genty, H. Ludvigsen, and M. Kaviola, “Supercontinuum generation in a highly birefringent microstructured fiber,” *Appl. Phys. Lett.*, vol. 82, pp. 2197–2199, 2003.

[55] S. Coen, A. H. L. Chau, R. Leonhardt, J. D. Harvey, J. C. Knight, W. J. Wadsworth, and P. S. J. Russell, “Supercontinuum generation by stimulated raman scattering and parametric four-wave mixing in photonic crystal fibers,” *J. Opt. Soc. Am. B*, vol. 19, pp. 753–764, 2002.

[56] E. R. Martins, D. H. Spadoti, M. A. Romero, and B.-H. V. Borgesl, “Theoretical analysis of supercontinuum generation in a highly birefringent d-spaced microstructured optical fiber,” *Opt. Express*, vol. 15, pp. 14335–14347, 2007.

[57] A. Tonello, S. Pitois, S. Wabnitz, G. Millot, T. Martynkien, W. Urbanczyk, J. Wojcik, A. Locatelli, M. Conforti, and C. D. Angelis, “Frequency tunable polarization and intermodal modulation instability in high birefringence holey fiber,” *Opt. Express*, vol. 14, pp. 397–404, 2005.

[58] J. M. Dudley, L. Provino, N. Grossard, H. Mailotte, R. S. Windeler, B. J. Eggleton, and S. Coen, “Supercontinuum generation in air-silica microstructured fibers with nanosecond and femtosecond pulse pumping,” *J. Opt. Soc. Am. B*, vol. 19, pp. 765–771, 2002.

[59] D. A. Akimov, E. E. Serebryannikov, A. M. Zheltikov, M. Schmitt, R. Maksimenka, W. Kiefer, K. V. Dukelskii, V. S. Shevandin, and Y. N. Kondratev, “Efficient anti-stokes generation through phase-matched four-wave mixing in higher-order modes of a microstructure fiber,” *Opt. Lett.*, vol. 28, pp. 1948–1950, 2003.

[60] P. V. Mamyshev and S. V. Chernikov, "Ultrashort-pulse propagation in optical fibers," *Opt. Lett.*, vol. 15, pp. 1076–1078, 1990.

[61] B. Kibler, J. M. Dudley, and S. Coen, "Supercontinuum generation and nonlinear pulse propagation in photonic crystal fiber: influence of the frequency-dependent effective mode area," *Appl. Phys. B*, vol. 81, pp. 337–342, 2005.

[62] Q. Lin and G. P. Agrawal, "Raman response function for silica fibers," *Opt. Lett.*, vol. 31, pp. 3086–3088, 2006.

[63] R. H. Hardin and F. D. Tappert, "Applications of the split-step fourier method to the numerical solution of nonlinear and variable coefficient wave equations," *SIAM Rev. Chronicle*, vol. 15, p. 423, 1973.

[64] R. A. Fisher and W. Bischel, "The role of linear dispersion in plane-wave self-phase modulation," *Appl. Phys. Lett.*, vol. 23, pp. 661–663, 1973.

[65] J. Hult, "A fourth-order rungrkutta in the interaction picture method for simulating supercontinuum generation in optical fibers," *J. Lightw. Technol.*, vol. 27, pp. 3358–3369, 2007.

[66] V. E. Zakharov and A. B. Shabat, "Exact theory of two-dimensional self-focusing and one-dimensional self-modulation of waves in nonlinear media," *Sov. Phys. JETP*, vol. 34, pp. 62–69, 1972.

[67] M. J. Ablowitz and P. A. Clarkson, *Solitons, Nonlinear Evolution Equations and Inverse Scattering*. Cambridge University Press, 1991.

[68] N. N. Akhmediev and A. A. Ankiewicz, *Dissipative Solitons*. Springer, 2005.

[69] C. R. Menyuk, "Stability of solitons in birefringent optical fibers. I. equal propagation amplitudes," *Opt. Lett.*, vol. 12, pp. 614–616, 1987.

[70] R.-J. Essiambre, M. A. Mestre, R. Ryf, A. H. Gnauck, R. W. Tkach, A. R. Charplyvy, Y. Sun, X. Jiang, and R. Lingle, "Experimental observation of inter-modal cross-phase modulation in few-mode fibers," *IEEE Photon. Technol. Lett.*, vol. 25, pp. 535–538, 1981.

[71] A. Picozzi, G. Millot, and S. Wabnitz, "Nonlinear optics: Nonlinear virtues of multimode fibre," *Nat. Photon.*, vol. 9, pp. 289–291, 2015.

[72] C. R. Menyuk, "Stability of solitons in birefringent optical fibers. ii. arbitrary amplitudes," *J. Opt. Soc. Am. B*, vol. 5, pp. 392–401, 1998.

[73] C. Xie, H. Karlsson, and P. A. Andrekson, "Soliton robustness to the polarization-mode dispersion in optical fibers," *IEEE Photon. Technol. Lett.*, vol. 12, pp. 801–803, 2000.

[74] S.-S. Yu, C.-H. Chien, Y. Lai, and J. Wang, "Spatio-temporal solitary pulses in graded-index materials with kerr nonlinearity," *Opt. Commun.*, vol. 119, pp. 167–170, 1995.

[75] S. Raghavan and G. P. Agrawal, "Spatiotemporal solitons in inhomogenous nonlinear media," *Opt. Commun.*, vol. 180, pp. 377–382, 2000.

[76] X.Liu, L. Qian, and F. W. Wise, “Generation of optical spatiotemporal solitons,” *Phys. Rev. Lett.*, vol. 82, pp. 4631–4634, 1999.

[77] T. Camron, C. Anastassiou, S. Lan, D. Kip, Z. H. Musslimani, M. Segev, and D. Christodoulides, “Observation of two-dimensional multimode solitons,” *Opt. Lett.*, vol. 25, pp. 1113–1115, 2000.

[78] J. P. Gordon, “Interaction forces among solitons in optical fibers,” *Opt. Lett.*, vol. 8, pp. 596–598, 1983.

[79] B. Hermansson and D. Yevick, “Numerical investigation of soliton interaction,” *Electron. Lett.*, vol. 19, pp. 570–571, 1983.

[80] K. J. Blow and N. J. Doran, “Bandwidth limits of nonlinear (soliton) optical communication systems,” *Electron. Lett.*, vol. 19, pp. 429–430, 1983.

[81] D. Anderson and M. Lisak, “Bandwidth limits due to incoherent soliton interaction in optical-fiber communication systems,” *Phys. Rev. A*, vol. 32, pp. 2270–2274, 1985.

[82] D. Anderson and M. Lisak, “Bandwidth limits due to mutual pulse interaction in optical soliton communication systems,” *Opt. Lett.*, vol. 11, pp. 174–176, 1986.

[83] Y. Kodama and K. Nozaki, “Soliton interaction in optical fibers,” *Opt. Lett.*, vol. 12, pp. 1038–1040, 1987.

[84] C. Desem and P. L. Chu, “Soliton propagation in the presence of source chirping and mutual interaction in single-mode optical fibres,” *Electron. Lett.*, vol. 23, pp. 260–262, 1987.

[85] C. Desem and P. L. Chu, “Soliton interaction in the presence of loss and periodic amplification in optical fibers,” *Opt. Lett.*, vol. 12, pp. 349–351, 1987.

[86] C. Desem and P. L. Chu, “Reducing soliton interaction in single-mode optical fibres,” *IEE Proc.*, vol. 134, pp. 145–151, 1987.

[87] F. M. Mitschke and L. F. Mollenauer, “Experimental observation of interaction forces between solitons in optical fibers,” *Opt. Lett.*, vol. 12, pp. 355–357, 1987.

[88] T. Georges and F. Favre, “Modulation, filtering, and initial phase control of interacting solitons,” *J. Opt. Soc. Am. B*, vol. 10, pp. 1880–1889, 1993.

[89] R.-J. Essiambre, B. Mikkelsen, and G. Raybon, “Intra-channel cross-phase modulation and four-wave mixing in high-speed TDM systems,” *Electron. Lett.*, vol. 35, pp. 1576–1578, 1999.

[90] P. V. Mamyshev and N. A. Mamysheva, “Pulse-overlapped dispersion-managed data transmission and intrachannel four-wave mixing,” *Opt. Lett.*, vol. 24, pp. 1454–1456, 1999.

[91] A. Antikainen, M. Erkintalo, J. M. Dudley, and G. Genty, “On the phase-dependent manifestation of optical rogue waves,” *Opt. Lett.*, vol. 24, pp. 1454–1456, 1999.

[92] K. Kurokawa, H. Kubota, and M. Nakazawa, “Soliton self-frequency shift accelerated by femtosecond soliton interaction,” *Electron. Lett.*, vol. 28, pp. 2052–2054, 1992.

[93] S. Kumar, A. Selvarajan, and G. V. Anand, “Influence of raman scattering on the cross phase modulation in optical fibers,” *Opt. Commun.*, vol. 102, pp. 329–335, 1993.

[94] S. Kumar, “Influence of raman effects in wavelength-division multiplexed soliton systems,” *Opt. Lett.*, vol. 23, pp. 1450–1452, 1998.

[95] W.-J. Liu, B. Tian, H.-Q. Zhang, L.-L. Li, and Y.-S. Xue, “Soliton interaction in the higher-order nonlinear schrödinger equation investigated with Hirota’s bilinear method,” *Phys. Rev. E*, vol. 77, p. 066605, 2008.

[96] A. Hause and F. Mitschke, “Reduced soliton interaction by raman self-frequency shift,” *Phys. Rev. A*, vol. 80, p. 063824, 2009.

[97] M. F. Saleh, A. Armaroli, A. Marini, and F. Biancalana, “Strong raman-induced noninstantaneous soliton interactions in gas-filled photonic crystal fibers,” *Opt. Lett.*, vol. 40, pp. 4058–4061, 2015.

[98] M. N. Islam, G. Sucha, I. Bar-Joseph, M. Wegener, J. P. Gordon, and D. S. Chemla, “Femtosecond distributed soliton spectrum in fibers,” *J. Opt. Soc. Am. B*, vol. 6, pp. 1149–1158, 1989.

[99] M. H. Frosz, O. Bang, and A. Bjarklev, “Soliton collision and raman gain regimes in continuous-wave pumped supercontinuum generation,” *Opt. Express*, vol. 14, pp. 9391–9407, 2006.

[100] M. Erkintalo, G. Genty, and J. M. Dudley, “On the statistical interpretation of optical rogue waves,” *Eur. Phys. J. Special Topics*, vol. 185, pp. 135–144, 2006.

[101] J. M. Dudley, F. Dias, M. Erkintalo, and G. Genty, “Instabilities, breathers and rogue waves in optics,” *Nat. Photonics*, vol. 8, pp. 755–764, 2014.

[102] B. J. Hong and C. C. Yang, “Interactions between femtosecond solitons in optical fibers,” *J. Opt. Soc. Am. B*, vol. 8, pp. 1114–1121, 2014.

[103] F. Luan, D. V. Skryabin, A. V. Yulin, , and J. C. Knight, “Energy exchange between colliding solitons in photonic crystal fibers,” *Opt. Express*, vol. 14, pp. 9844–9853, 2006.

[104] Q. M. Nguyen and A. Peleg, “Resolving the raman-induced cross frequency shift in fast optical soliton collisions,” *J. Opt. Soc. Am. B*, vol. 27, pp. 1985–1990, 2010.

[105] M. Erkintalo, G. Genty, and J. M. Dudley, “Experimental signatures of dispersive waves emitted during soliton collisions,” *Opt. Express*, vol. 18, pp. 13379–13384, 2010.

[106] J. M. Dudley and J. R. Taylor, *Supercontinuum Generation in Optical Fibers*. Cambridge University Press, 2010.

[107] S. Diddams, “The evolving optical frequency comb [invited],” *J. Opt. Soc. Am. B*, vol. 27, pp. B51–B62, 2010.

[108] Y. Takushima, F. Futami, and K. Kikuchi, “Generation of over 140-nm-wide supercontinuum from a normal dispersion fiber by using a mode-locked semiconductor laser source,” *IEEE Photon. Technol. Lett.*, vol. 10, pp. 1560–1562, 1998.

[109] A. M. Heidt, "Pulse preserving flat-top supercontinuum generation in all-normal dispersion photonic crystal fibers," *J. Opt. Soc. Am. B*, vol. 27, pp. 550–559, 2010.

[110] A. M. Heidt, A. Hartung, G. W. Bosman, P. Krok, E. G. Rohwer, H. Schwoerer, and H. Bartlet, "Coherent octave spanning near-infrared and visible supercontinuum generation in all-normal dispersion photonic crystal fibers," *Opt. Express*, vol. 19, pp. 3775–3787, 2011.

[111] L. E. Hooper, P. J. Mosley, A. C. Muir, W. J. Wadsworth, and J. C. Knight, "Coherent supercontinuum generation in photonic crystal fiber with all-normal group velocity dispersion," *Opt. Express*, vol. 19, pp. 4902–4907, 2011.

[112] M. Klimczak, B. Siwicki, P. Skibiński, D. Pysz, R. Stepień, A. Heidt, C. Radzewicz, and R. Buczyński, "Coherent supercontinuum generation up to 2.3 um in all-solid soft-glass photonic crystal fibers with flat all-normal dispersion," *Opt. Express*, vol. 22, pp. 18824–18832, 2014.

[113] G. Lopez-Galmiche, Z. S. Eznaveh, M. A. Eftekhar, J. A. Lopez, L. G. Wright, F. W. Wise, D. Christodoulides, and R. A. Correa, "Visible supercontinuum generation in a graded index multimode fiber pumped at 1064 nm," *Opt. Lett.*, vol. 41, pp. 2553–2556, 2016.

[114] M. A. Eftekhar, L. G. Wright, M. S. Mills, M. Kolesik, R. A. Correa, F. W. Wise, and D. N. Christodoulides, "Versatile supercontinuum generation in parabolic multimode optical fibers," *Opt. Express*, vol. 25, pp. 9078–9087, 2017.

[115] U. Tegin and B. Ortac, "Geometric parametric instability of femtosecond pulses in graded-index multimode fiber," *Frontiers in Optics*, p. JTu3A.72, 2017.

[116] B. R. Washburn, J. A. Buck, and S. E. Ralph, "Transform-limited spectral compression due to self-phase modulation in fibers," *Opt. Lett.*, vol. 25, pp. 445–447, 2000.

[117] E. R. Andersen, J. T. gersen, and S. R. Keiding, "Spectral compression of femtosecond pulses in photonic crystal fibers," *Opt. Lett.*, vol. 30, pp. 2025–2027, 2005.

[118] S. Turitsyn, A. E. Bednyakova, M. P. Fedoruk, S. B. Papernyi, and W. R. L. Clements, "Inverse four-wave mixing and self-parametric amplification in optical fibre," *Nat. Photon.*, vol. 9, pp. 608–614, 2015.

[119] S. Mumtaz, R. J. Essiambre, and G. P. Agrawal, "Reduction of nonlinear penalties due to linear coupling in multicore optical fibers," *IEEE Photon. Technol. Lett.*, vol. 24, pp. 1574–1576, 2012.

[120] K. Ho and J. Kahn, "Delay-spread distribution for multimode fiber with strong mode coupling," *IEEE Photon. Technol. Lett.*, vol. 24, pp. 1574–1576, 2012.

[121] L. Yu and B. S. Rawat, "Mode-coupling analysis of depolarization effects in a multimode optical fiber," *J. Lightw. Technol.*, vol. 10, pp. 556–562, 1992.

[122] M. B. Shemirani, W. Mao, R. Panicker, and J. Kahn, "Principal modes in graded-index multimode fiber in presence of spatial- and polarization-mode coupling," *J. Lightw. Technol.*, vol. 27, pp. 1248–1261, 2009.

[123] F. Yaman, E. Mateo, and T. Wang, "Impact of modal crosstalk and multi-path interference on few-mode fiber transmission," *Proc. Opt. Fiber Commun. Conf.*, vol. paper OTu1D.2, 2012.

[124] H. Bulow, H. Al-Hashimi, B. T. Abebe, and B. Schmauss, "Capacity and outage of multimode fiber with statistical bends," *Proc. Opt. Fiber Commun. Conf.*, vol. paper OW3D.2, 2012.

[125] A. A. Juarez, E. Krune, S. Warm, C. A. Bunge, and K. Peterman, "Modeling of mode coupling in multimode fibers with respect to bandwidth and loss," *J. Lightw. Technol.*, vol. 32, pp. 1549–1558, 2014.

[126] C. Antonelli, M. Shtaif, and A. Mecozzi, "Modeling of nonlinear propagation in space-division multiplexed fiber-optic transmission," *J. Lightw. Technol.*, vol. 34, pp. 36–54, 2016.

[127] C. Antonelli, A. Mecozzi, and M. Shtaif, "Scaling of inter-channel nonlinear interference noise and capacity with the number of strongly coupled modes in sdm systems," *Proc. Opt. Fiber Comm. Conf.*, vol. W4I.2, 2016.

[128] F. M. Ferreira, C. S. Costa, S. Sygletos, and A. D. Ellis, "Semi-analytical modelling of linear mode coupling in few-mode fibers," *J. Lightw. Technol.*, vol. 35, pp. 4011–4022, 2017.

[129] S. V. Manakov, "On the theory of two-dimensional stationary self-focusing of electromagnetic waves," *Zh. Eksp. Teor. Fiz.*, vol. 65, pp. 505–516, 1973.

[130] D. Marcuse, C. R. Menyuk, and P. K. A. Wai, "Application of the manakov-PMD equation to studies of signal propagation in optical fibers with randomly varying birefringence," *J. Lightw. Technol.*, vol. 15, pp. 1735–1746, 1997.

[131] D. Marcuse, *Light Transmission Optics.* Van Nostrand Reinhold, 1982.

[132] Y. Xiao, R. J. Essiambre, M. Desgroseilliers, A. M. Tulino, R. Ryf, S. Mumtaz, and G. P. Agrawal, "Theory of intermodal four-wave mixing with random linear mode coupling in few-mode fibers," *Opt. Express*, vol. 22, pp. 32039–32059, 2014.

[133] A. M. Tulino and S. Verdú, "Random matrix theory and wireless communications," *Communications and Information Theory*, vol. 1, pp. 1–182, 2004.

[134] D. Marcuse, "Fluctuations of the power of coupled modes," *Bell Sys. Tech. J.*, vol. 51, pp. 1793–1800, 1972.

[135] D. Gloge, "Optical power flow in multimode fibers," *Bell Sys. Tech. J.*, vol. 51, pp. 1767–1783, 1972.

[136] R. Olshanky, "Mode coupling effects in graded-index optical fibers," *Appl. Optics*, vol. 14, pp. 935–945, 1975.

[137] S. C. Rashleigh, "Origins and control of polarization effects in single-mode fibers," *J. Lightw. Technol.*, vol. LT-1, pp. 312–331, 1983.

[138] J. M. Fini, B. Zhu, T. F. Taunay, and M. F. Yan, "Statistics of crosstalk in bent multicore fibers," *Opt. Express*, vol. 18, pp. 15122–15129, 2010.

[139] G. Rademacher, R. S. Luis, B. J. Puttnam, Y. Awaji, and N. Wada, "Crosstalk dynamics in multi-core fibers," *Opt. Express*, vol. 25, pp. 12020–12028, 2017.

[140] S. Rommel, J. M. D. Mendinueta, W. Klaus, J. Sakaguchi, J. J. V. Olmos, Y. Awaji, I. T. Monroy, and N. Wada, "Few-mode fiber, splice and SDM component characterization by spatially-diverse optical vector network analysis," *Opt. Express*, vol. 25, pp. 22347–22361, 2017.

[141] S. Ohno, K. Toge, D. Iida, and T. Manabe, "Distributed spatial mode dispersion measurement along strongly coupled multicore fibers based on correlation analysis of rayleigh backscattering amplitudes," *Opt. Express*, vol. 25, pp. 29650–29658, 2017.

[142] J. C. Alvarado-Zacarias, B. Huang, Z. S. Eznaveh, N. K. Fontaine, H. Chen, R. Ryf, J. E. Antonio-Lopez, and R. A. Correa, "Experimental analysis of the modal evolution in photonic lanterns," *Frontiers in Optics*, vol. Tu2J.7, 2017.

# APPENDIX

# Appendix A

# Deriving k$^{\mathrm{th}}$ component of nonlinear term with random coupling included

In this appendix, we present the mathematical steps and explain the approximations that were used in deriving Eq. (7.12) using Eq. (7.11).

We start with the following equation for the nonlinear term in the matrix form [see Eq. (7.11)]:

$$\boldsymbol{\mathcal{N}} = \frac{\imath\gamma}{3}\iint \left[2(\bar{\mathbf{A}}^{\mathrm{H}}\mathbf{T}^{\mathrm{H}}\mathbf{G}^{(1)}\mathbf{T}\bar{\mathbf{A}})\mathbf{T}^{\mathrm{H}}\mathbf{G}^{(1)}\mathbf{T}\bar{\mathbf{A}} + (\bar{\mathbf{A}}^{\mathrm{T}}\mathbf{T}^{\mathrm{T}}\mathbf{G}^{(2)}\mathbf{T}\bar{\mathbf{A}})\mathbf{T}^{\mathrm{H}}\mathbf{G}^{(2)*}\mathbf{T}^{*}\bar{\mathbf{A}}^{*}\right] dx\, dy. \tag{A.1}$$

We treat the two terms separately.

(i) $\quad$ *First term* : $\boldsymbol{\mathcal{N}}^{(\mathbf{1})} = \frac{\imath\gamma}{3}\iint \left[2(\bar{\mathbf{A}}^{\mathrm{H}}\mathbf{T}^{\mathrm{H}}\mathbf{G}^{(1)}\mathbf{T}\bar{\mathbf{A}})\mathbf{T}^{\mathrm{H}}\mathbf{G}^{(1)}\mathbf{T}\bar{\mathbf{A}}\right] dx\, dy$

Writing the $k^{th}$ element of the matrix product in $\mathcal{N}^{(\mathbf{1})}$ as a summation in the most general form, where all index values go from 0 to N, we get the following equation,

$$\hat{\mathcal{N}}_k^{(1)} = \frac{\imath\gamma}{3}\sum_{i,j,l,m,n,o,p}\iint \left[2\bar{A}_l^{*}t_{ml}^{*}g_{mj}^{(1)}t_{ji}\bar{A}_i t_{nk}^{*}g_{no}^{(1)}t_{op}\bar{A}_p\right] dxdy \tag{A.2}$$

***First reduction***: Phase-matching $\implies$ only terms of the form $|\bar{A}_l|^2\bar{A}_k$ make non-negligible contributions. This follows from the fact that the $\bar{A}$ has $e^{\imath\delta\beta_0}z$ term in its definition, where $\delta\beta_0$ is the propagation constant of the mode relative to the reference mode. So, the condition for phase-matching becomes

$$\delta\beta_0^k \approx -\delta\beta_0^l + \delta\beta_0^i + \delta\beta_0^p \tag{A.3}$$

We make the choice of $p = l$ and $i = k$ to satisfy this phase-matching condition. It is important to note that:

- The intermodal four-wave mixing (IM-FWM) terms, which are not phase-matched at the same frequency can, in theory, be perfectly phase-matched at different distinct frequencies in different modes. But we have numerically verified that, on average, the contribution of the IM-FWM-like terms is negligible when linear coupling is included.
- Since the alternate choice of $i = l$ and $p = k$ would yield the same result, we multiply by a factor of $2/(1 + d_{kl})$ to account for that degeneracy built into our

choice. To recall, $d_{kl}$ is 1 when $k$ and $l$ belong to the same degenerate mode group but 0 otherwise.

The resulting equation becomes:

$$\hat{\mathcal{N}}_k^{(1)} = \frac{\imath\gamma}{3} \sum_{j,l,m,n,o} \frac{2}{(1+d_{kl})} \iint \left[2|\bar{A}_l|^2 \bar{A}_k \left(g_{mj}^{(1)} g_{no}^{(1)}\right) \left(t_{ml}^* t_{jk} t_{nk}^* t_{nl}\right)\right] dxdy \tag{A.4}$$

***Second reduction***: Orthogonality relation of spatial profile $F_m \implies \iint g_{mj}^{(1)} g_{no}^{(1)} dxdy = \iint F_m^* F_j F_n^* F_o dxdy \neq 0$ only if $j = m, o = n$, or $j = n, o = m$. These conditions can be expressed as

$$f_{plmn}^{(1)} = \iint F_p^* F_l F_m^* F_n dxdy = \frac{(\delta_{pl}\delta_{mn} + \delta_{pn}\delta_{lm})}{(1+d_{pm})} I_{plmn}^{(1)} \tag{A.5}$$

where $I_{plmn}^{(1)}$ corresponds to the magnitude of the integral. So, we set 1) $j = m$ and $o = n$ and 2) $j = n$ and $o = m$ to get the two terms which have non-zero contributions. This leads to the following equation:

$$\hat{\mathcal{N}}_k^{(1)} = \frac{\imath\gamma}{3} \sum_{l,m,n} \frac{2}{(1+d_{kl})} \frac{1}{(1+d_{mn})} \left[2|\bar{A}_l|^2 \bar{A}_k f_{mmnn}^{(1)} \left(t_{ml}^* t_{mk} t_{nk}^* t_{nl}\right) + 2|\bar{A}_l|^2 \bar{A}_i f_{mnnm}^{(1)} \left(|t_{ml}|^2 |t_{nk}|\right)\right] \tag{A.6}$$

By definition [Eq. (A.5)], $f_{mmnn}^{(1)} = f_{mnnm}^{(1)}$, so the two terms can be combined and written as:

$$\hat{\mathcal{N}}_k^{(1)} = \frac{\imath\gamma}{3} \sum_{l,m,n} \frac{2}{(1+d_{kl})} \frac{1}{(1+d_{mn})} \left[2 f_{mmnn}^{(1)} \left(t_{ml}^* t_{mk} t_{nk}^* t_{nl} + |t_{ml}|^2 |t_{nk}|^2\right) |\bar{A}_l|^2 \bar{A}_k\right] \tag{A.7}$$

(ii) *Second term* : $\boldsymbol{\mathcal{N}}^{(2)} = \frac{\imath\gamma}{3} \iint \left[(\bar{\mathbf{A}}^{\mathrm{T}} \mathbf{T}^{\mathrm{T}} \mathbf{G}^{(2)} \mathbf{T} \bar{\mathbf{A}}) \mathbf{T}^{\mathrm{H}} \mathbf{G}^{(2)*} \mathbf{T}^* \bar{\mathbf{A}}^*\right] dx\, dy$

We follow the same steps as shown here for the first term, but the orthogonality argument in this case becomes $\iint g_{mj}^{(2)} g_{no}^{(2)*} dxdy = \iint F_m F_j F_n^* F_o^* dxdy \neq 0$ only if $n = m, o = j$ OR $n = j, o = m$ , which can be written as:

$$f_{plmn}^{(2)} = \iint F_p F_l F_m^* F_n^* dxdy = \frac{(\delta_{pm}\delta_{ln} + \delta_{pn}\delta_{lm})}{(1+d_{pm})} I_{plmn}^{(2)} \tag{A.8}$$

where $I_{plmn}^{(2)}$ corresponds to the magnitude of the integral. Using this and the phase-matching argument similar to Eq. (A.3), we eventually get:

$$\hat{\mathcal{N}}_k^{(2)} = \frac{\imath\gamma}{3} \sum_{j,l,m} \frac{2}{(1+d_{kl})} \frac{1}{(1+d_{mj})} \left[|\bar{A}_l|^2 \bar{A}_k f_{mjmj}^{(2)} \left(t_{ml} t_{jk} t_{mk}^* t_{jl}^*\right) + |\bar{A}_l|^2 \bar{A}_k f_{mjjm}^{(2)} \left(|t_{ml}|^2 |t_{jk}|^2\right)\right] \tag{A.9}$$

We do the following index variable change: $j \to m$ and $m \to n$ for the first term and $j \to n$ for the second term in Eq. (A.9). This is not inconsistent, since only the dummy indices are being changed. The purpose for doing this is to make the product of $t_{ij}$ terms to be similar to Eq. (A.7). The equation then becomes,

$$\hat{\mathcal{N}}_k^{(2)} = \frac{\imath\gamma}{3} \sum_{l,m,n} \frac{2}{(1+d_{kl})} \frac{1}{(1+d_{mn})} \left[ |\bar{A}_l|^2 \bar{A}_k f^{(2)}_{nmnm} \left(t_{nl} t_{mk} t^*_{nk} t^*_{ml}\right) + |\bar{A}_l|^2 \bar{A}_k f^{(2)}_{mnnm} \left(|t_{ml}|^2 |t_{nk}|^2\right) \right] \tag{A.10}$$

By definition [Eq. (A.8)], $f^{(2)}_{nmnm} = f^{(2)}_{mnnm}$, so the two terms can be combined and written as:

$$\hat{\mathcal{N}}_k^{(2)} = \frac{\imath\gamma}{3} \sum_{l,m,n} \frac{2}{(1+d_{kl})} \frac{1}{(1+d_{mn})} \left[ f^{(2)}_{nmnm} \left(t_{ml} t_{nk} t^*_{mk} t^*_{nl} + |t_{ml}|^2 |t_{nk}|^2\right) |\bar{A}_l|^2 \bar{A}_k \right] \tag{A.11}$$

(iii) *Final expression*

Now, we combine both the terms from Eq. (A.7) and Eq. (A.11) to get the final equation for the $k^{th}$ component of the non-linear term

$$\hat{\mathcal{N}}_k = \hat{\mathcal{N}}_k^{(1)} + \hat{\mathcal{N}}_k^{(2)} = \imath\gamma \sum_{l,m,n} \frac{2\left(t_{ml} t_{nk} t^*_{mk} t^*_{nl} + |t_{ml}|^2 |t_{nk}|^2\right)}{3(1+d_{kl})(1+d_{mn})} (2 f^{(1)}_{mmnn} + f^{(2)}_{nmnm}) |\bar{A}_l|^2 \bar{A}_k \tag{A.12}$$

We can further reduce this equation by using the equality $f^{(1)}_{mmnn} = f^{(2)}_{nmnm}$, which follows from the definition of both these terms, and define them as $f_{mmnn}$. This leads to the more compact equation:

$$\hat{\mathcal{N}}_k = \imath\gamma \sum_{l,m,n} \frac{2\left(t_{ml} t_{nk} t^*_{mk} t^*_{nl} + |t_{ml}|^2 |t_{nk}|^2\right)}{(1+d_{kl})(1+d_{mn})} f_{mmnn} |\bar{A}_l|^2 \bar{A}_k \tag{A.13}$$

# Appendix B

# Deriving nonlinear coefficients for the averaged Manakov equation

In this appendix, we derive the averaged coefficients of the nonlinear terms in the Manakov equations for the general case when modes belonging to the same mode group in a fiber are coupled but there is no coupling between different mode groups. We start with Eq. (7.12) from chapter 7. To find the averaged equations, we need to find the average of the transfer matrix moments:

$$< \hat{\mathcal{N}}_k >= \imath\gamma \sum_{l=1}^{\mathrm{N}} \sum_{m=1}^{\mathrm{N}} \sum_{n=1}^{\mathrm{N}} \frac{2 < (|t_{ml}|^2 |t_{nk}|^2 + t_{ml} t_{nk} t^*_{mk} t^*_{nl}) >}{(1+d_{kl})(1+d_{mn})} f_{mmnn} |\bar{A}_l|^2 \bar{A}_k. \tag{B.1}$$

To recall, we denote by $S_l$ the modes that belong to the mode-group $l$ and by $n_l$ the number of modes present in the mode-group $l$. We evaluate separately for 2 situations:

**$l$ and $k$ belong to different mode groups** (B.2)

In this case,

$$< t_{ml} t_{nk} t^*_{mk} t^*_{nl} >= 0, \quad < |t_{ml}|^2 |t_{nk}|^2 >\neq 0 \text{ if } m \in S_l \text{ and } n \in S_k. \tag{B.3}$$

This means that $d_{kl}, d_{mn} \to 0$. As we have shown that the averaged transfer matrix is a Haar matrix, we can use the following property of unitary matrices

$$< |t_{ml}|^2 |t_{nk}|^2| >= \frac{1}{n_l n_k}. \tag{B.4}$$

Substituting this in Eq. (B.1), we end up with

$$< \hat{\mathcal{N}}_k^{(1)} >= \frac{2\imath\gamma}{n_k} \sum_{l=1}^{\mathrm{N}} \frac{1}{n_l} \sum_{m\in S_l} \sum_{n \in S_k} 2 f_{mmnn} |\bar{A}_l|^2 \bar{A}_k. \tag{B.5}$$

**$l$ and $k$ belong to the same mode group** (B.6)

In this case, all four possible fourth-order moments survive. Since $k$ and $l$ are coupled, $S_k = S_l$. We get non-zero contributions only when $m, n \in S_k = S_l$. Thus, $d_{mn}, d_{kl} \to 1$.

Using the formula for the moments of a Haar matrix, we get:

$$
\begin{aligned}
<|t_{ij}|^4> &= \frac{2}{n_k(n_k+1)} && \text{(B.7)}\\
<|t_{ik}|^2|t_{il}|^2> &= \frac{1}{n_k(n_k+1)} \qquad (k \neq l), && \text{(B.8)}\\
<|t_{ik}|^2|t_{jl}|^2> &= \frac{1}{(n_k-1)(n_k+1)} \qquad (i \neq j \quad \text{and} \quad k \neq l), && \text{(B.9)}\\
<t_{ik}t_{jl}t^*_{il}t^*_{jk}> &= \frac{-1}{(n_k-1)n_k(n_k+1)} \qquad (i \neq j \quad \text{and} \quad k \neq l). && \text{(B.10)}
\end{aligned}
$$

Adding the contributions from all these terms and dividing by 4 to account for the $(1 + d_{kl})(1 + d_{mn})$ term, we end up with $1/[n_k(n_k + 1)]$. Using the fact that $n_l = n_k$, we get the following expression

$$
<\hat{\mathcal{N}}_k^{(2)}>= \frac{2\imath\gamma}{n_k}\sum_{l=1}^{\mathrm{N}} \frac{1}{(n_l+1)} \sum_{m\in S_l}\sum_{n\in S_k} f_{mmnn}|\bar{A}_l|^2\bar{A}_k. \tag{B.11}
$$

Both these equations can be combined and written in the final form:

$$
<\hat{\mathcal{N}}_k>=<\hat{\mathcal{N}}_k^{(1)}>+<\hat{\mathcal{N}}_k^{(2)}>= \frac{2\imath\gamma}{n_k}\sum_{l=1}^{\mathrm{N}} \frac{1}{(n_l+d_{lk})} \sum_{m\in S_l}\sum_{n\in S_k} f_{mmnn}|\bar{A}_l|^2\bar{A}_k, \tag{B.12}
$$

where, as defined for Eq. (7.12), $d_{lk}$ is 1 when $l$ and $k$ belong to coupled mode groups and 0 otherwise. Hence, the nonlinear coefficients in Eq. (7.16) can be written as

$$
C_{klmn} = \frac{2\gamma}{n_k}\frac{1}{n_l+d_{lk}} f_{mmnn}. \tag{B.13}
$$